UNIVERSITY OF CALIFORNIA SAN DIEGO

Seismic Response to Ocean Waves: Microseisms and Plate Waves

A dissertation submitted in partial satisfaction of the
requirements for the degree
Doctor of Philosophy

in

Earth Sciences

by

Zhao Chen

Committee in charge:

Peter Gerstoft, Chair
Peter D. Bromirski
William A. Coles
William S. Hodgkiss
John A. Orcutt
Peter M. Shearer

2019

The dissertation of Zhao Chen is approved, and it is acceptable in quality and form for publication on microfilm and electronically:

_____

_____

_____

_____

_____

_____

Chair

University of California San Diego

2019

DEDICATION

To my co-advisors Peter Gerstoft and Peter Bromirski for their guidance on both my research and life.

To my parents Lingbin Chen and Fengxia Qu for their ever love and support.

To my girlfriend Zhuqing Yuan for being the sunshine of my life.

EPIGRAPH

Look deep into nature, and then you will understand everything better.

—Albert Einstein

TABLE OF CONTENTS

LIST OF FIGURES

LIST OF TABLES

ACKNOWLEDGEMENTS

I would first like to thank my advisor, Peter Gerstoft, and my co-advisor, Peter Bromirski, for their support and guidance on my research. They are always reachable for discussion and are fast with feedback. I would like to thank my committee members for providing helpful suggestions in my research and presentations from different perspectives. I would like to thank my team members in Antarctica, with whom I had a wonderful field trip and recovered the fruitful dataset. I would like to thank my colleagues, who make up our happy and positive NoiseLab. I would like to thank my family and friends, who always love and support me. Without these great people in my life, I will never achieve this point.

Chapter 2, in full, is a reprint of the material as it appears in Geophysical Journal International: Chen, Z., Gerstoft, P., Bromirski, P.D., 2016, "Microseism source direction from noise cross-correlation", *Geophysical Journal International*, 205(2), pp.810-818. The dissertation author is the primary investigator and author of this paper.

Chapter 3, in full, is a reprint of the material as it appears in Journal of Glaciology: Chen, Z., Bromirski, P.D., Gerstoft, P., Stephen, R.A., Wiens, D.A., Aster, R.C., Nyblade, A.A., 2018, "Ocean-excited plate waves in the Ross and Pine Island Glacier ice shelves", *Journal of Glaciology*, 64(247), pp.730-744. The dissertation author is the primary investigator and author of this paper.

Chapter 4, in full, has been submitted for publication as Chen, Z., Bromirski, P.D., Gerstoft, P., Stephen, R.A., Lee, W.S., Yun, S., Olinger, S.D., Aster, R.C., Wiens, D.A., and Nyblade, A.A., 2019, "Ross Ice Shelf Icequakes Associated with Ocean Gravity Wave Activity", *Geophysical Research Letters.* The dissertation author was the primary investigator and author of the paper.

VITA

Sep 14, 1991	Born, Huaibei, Anhui, China
2008-2012	Bachelor of Science in Geophysics, Peking University, Beijing, China
2012-2018	Graduate Student Researcher, Scripps Institution of Oceanography, University of California San Diego, La Jolla, CA, United States
2019	Doctor of Philosophy in Earth Sciences, Scripps Institution of Oceanography, University of California San Diego, La Jolla, CA, United States

PUBLICATIONS

Chen, Z., Bromirski, P.D., Gerstoft, P., Stephen, R.A., Lee, W.S., Yun, S., Olinger, S.D., Aster, R.C., Wiens, D.A., and Nyblade, A.A., "Ross Ice Shelf Icequakes Associated with Ocean Gravity Wave Activity", *Geophysical Research Letters*, 2019 (submitted).

Chen, Z., Bromirski, P.D., Gerstoft, P., Stephen, R.A., Wiens, D.A., Aster, R.C., Nyblade, A.A., "Ocean-excited plate waves in the Ross and Pine Island Glacier ice shelves", *Journal of Glaciology*, 64(247), pp.730-744, 2018.

Bromirski, P.D., **Chen, Z.**, Stephen, R.A., Gerstoft P., Arcas, D., Diez, A., Aster, R.C., Wiens, D.A., Nyblade, A.A., "Tsunami and infragravity waves impacting Antarctic ice shelves", *Journal of Geophysical Research: Oceans*, 122, pp.5786-5801, 2017.

Chen, Z., Gerstoft, P., Bromirski, P.D., "Microseism source direction from noise cross-correlation", *Geophysical Journal International*, 205(2), 2016.

ABSTRACT OF THE DISSERTATION

Seismic Response to Ocean Waves: Microseisms and Plate Waves

by

Zhao Chen

Doctor of Philosophy in Earth Sciences

University of California San Diego, 2019

Peter Gerstoft, Chair

Microseisms and plate waves are two types of seismic waves that are generated by the interaction between the ocean surface gravity waves and the solid Earth, providing the primary seismic noise source on the Earth.

The source distribution of microseisms is important to study their generation mechanisms and in imaging Earth structures. Comparisons between different preprocessing methods to identify microseism source areas were made using Cascadia Initiative ocean bottom seismometer array data, where it was found that the total energy arriving from pelagic and coastal areas is similar. Moreover, pelagic-generated signals tend to be weaker but have a longer duration, in contrast to coastal-generated signals that tend to be stronger but have a shorter duration.

Ocean surface gravity waves interacting with Antarctic ice shelves affect their integrity and likely play a role in their evolution, critical for assessing long-term changes that will affect the rate of sea level rise. Long-period gravity-wave impacts excite plate waves in the ice shelves, which can expand pre-existing fractures and trigger iceberg calving. Flexural-gravity waves ($<$20 mHz) and extensional Lamb waves (20–100 mHz) were identified on both the Ross Ice Shelf and the Pine Island Glacier ice shelf. Considering the ubiquitous presence of storm activity in the Southern Ocean and the similar observations at both the Ross Ice Shelf and the Pine Island Glacier ice shelves, it is likely that most, if not all, West Antarctic ice shelves are subjected to similar gravity-wave excitation. The transfer of ocean wave energy to ice shelves was determined from the comparison of gravity wave forcing of the Ross Ice Shelf measured by an ocean bottom hydrophone near the ice shelf front with nearby broadband on-ice seismic observations. The relative impact of gravity wave forcing on the Ross Ice Shelf integrity is inferred from comparison of the Ross Ice Shelf response amplitudes in 0.001–0.04 Hz band and from the association of icequake activity with very-long-period (0.001–0.003 Hz) and swell (0.03–0.1 Hz) band responses.

Chapter 1

Introduction

Ocean surface gravity waves interact with the solid Earth and excite multiple types of seismic waves with different mechanisms, which provide the primary seismic noise source recorded by both land and ocean bottom stations. These ocean-excited seismic waves can be used in Earth structure imaging, and can also help understand the dynamics of the Antarctic ocean/ice-shelf system. The two major wave types, microseisms, generated in coastal and pelagic region, and plate waves, generated on ice shelves, are studied in depth in this dissertation.

1.1 Ocean surface gravity waves

Ocean surface gravity waves are water waves propagating at the ocean surface with gravity as their restoring force. Depending on the generation mechanisms, they can be classified into multiple types, including wind waves, swells, infragravity waves, and tsunamis. High-frequency ($>$80 mHz) surface gravity waves are generated by local winds, called wind waves. After strong storms with long duration and fetch, the higher-frequency waves attenuate, with lower-frequency swells (30–100 mHz) propagating over long distances [Munk et al. 1963]. Infragravity waves (3–20 mHz) are generated by nonlinear wave interactions along coastlines [Herbers, Elgar, and

Guza 1995; Bromirski, Sergienko, and MacAyeal 2010] and under mid-ocean storms [Uchiyama and McWilliams 2008]. Tsunamis (1–3 mHz) are forced by submarine seismic shift (with vertical component), landslides, meteorite impacts or volcanic eruptions.

In this dissertation, we will focus on the surface gravity waves, which explain most of our seismic observations of microseisms and plate waves. Internal waves (periods from $\sim$10 min to $\sim$1 day [Müller et al. 2015]) and tides (periods of 0.5 day or 1 day) are in a lower frequency band than microseisms (0.05–0.35 Hz) and the observed plate waves (0.001–0.1 Hz) and are not considered in this study.

1.2 Microseisms

Microseisms are generated by interactions between ocean wave energy and the seafloor in two frequency bands with different generation mechanisms. Single-frequency microseisms (0.05–0.1 Hz) are observed in the swell frequency band, while double-frequency microseisms (0.1–0.35 Hz) are observed at about twice the swell frequency band. Recorded everywhere on Earth [Webb 1998], microseisms can be used to image the Earth as a supplement to earthquakes, because earthquakes are highly heterogeneously distributed and limit the resolution in regions with less seismic ray paths [Shapiro and Campillo 2004]. With decades of recordings, microseisms can also be used to reconstruct the historical wave climate, which can avoid biases due to changing instruments and technologies in wave height observations (e.g. visual assessment from ships versus buoy measurements) [Grevemeyer, Herber, and Essen 2000]. Together with ocean bottom pressure measurements, microseisms have also been used to extract directional spectrum information of the ocean surface waves [Farrell and Munk 2010].

Microseisms have been studied since the nineteenth century [Bertelli 1874]. The mechanisms have been developed and improved since mid-twentieth century [e.g. Longuet-Higgins 1950; Hasselmann 1963; Traer and Gerstoft 2014; Ardhuin, Gualtieri, and Stutzmann 2015]. It is

generally accepted that single-frequency microseisms are generated by the interaction between the ocean waves and the seafloor near coasts [Hasselmann 1963], while double-frequency microseisms are generated by counter-propagating, or more generally, obliquely interacting surface waves [Longuet-Higgins 1950; Traer and Gerstoft 2014] that can occur in any open water setting. For the single-frequency band, all studies indicate shallow water generation [Cessaro 1994; Bromirski and Duennebier 2002], consistent with the theoretical work by [Hasselmann 1963]. For the double-frequency band, however, both pelagic generation [Bromirski, Duennebier, and Stephen 2005; Kedar et al. 2008; Ardhuin et al. 2011] and near-coastal generation [Bromirski, Flick, and Graham 1999; Bromirski, Duennebier, and Stephen 2005; Gerstoft and Tanimoto 2007; Yang and Ritzwoller 2008; Ardhuin et al. 2011] have been identified. Some studies support one dominant source area, while others conclude both source areas are important, rendering this topic still under debate. In Chapter 2, the microseism source direction is analyzed with the data from the Cascadia Initiative ocean bottom seismometer array. The Cascadia Initiative is a 4-year (summer 2011 to summer 2015) onshore/offshore seismic and geodetic experiment focusing on the megathrust earthquakes, volcanism, and geology of the Juan De Fuca and Gorda plates, with 64, 70, 70, and 93 ocean bottom seismometers deployed each year respectively. With both shallow-water and deep-water stations off the US west coast, this array facilitates the comparison between the coastal and pelagic microseismic source characteristics.

1.3 Antarctic ocean/ice-shelf system

Of all the glaciological components comprising the Antarctic Ice Sheet, Ice shelves are the most vulnerable to climate change. This is because ice shelves are in contact with the most dynamic, changeable parts of the ocean and atmosphere, and because they are the parts of the glaciological system that respond most quickly to changes in mass, energy, and stress balances. At the same time, ice shelves play an important role in inhibiting sea level rise as they

buttress glaciers on land and restrain ice discharge to the circum-Antarctica seas that merge with the Southern Ocean [MacAyeal 1987; Rignot et al. 2004; Scambos et al. 2004]. Volume loss of Antarctic ice shelves [Paolo, Fricker, and Padman 2015] reduces buttressing, which raises concerns of consequent acceleration of glacier discharge, raising sea level. Ice shelf volume loss results from ice shelf thinning due to enhanced ocean-driven melting and iceberg calving [Pritchard et al. 2012; Paolo, Fricker, and Padman 2015]. Therefore, it is critical to understand the dynamics and monitor the evolution of Antarctic ice shelves.

1.3.1 Thermodynamic system

A primary thermodynamic control on ice-shelf thickness and integrity is surface melting [Scambos et al. 2000; Scambos et al. 2009]. The other main thermodynamic control, basal melting [Pritchard et al. 2012; Hellmer et al. 2012], is also a possible precursor to ice-shelf disintegration. Basal melting depends on circulation into the cavity below the Ross Ice Shelf [Smethie and Jacobs 2005; Shepherd et al. 2003; Holland et al. 2008], which depends on regional ocean circulation patterns [Orsi and Wiederwohl 2009; Thoma et al. 2008] and ocean temperature [Gille 2008].

In the Antarctic circulation system (Figure 1.1), near-freezing High-Salinity Shelf Water (HSSW) forms as a byproduct of sea ice production in the continental shelf region. To the north, HSSW mixes with the warmer Circumpolar Deep Water (CDW) and sinks along the continental slope, feeding the Antarctic Bottom Water (AABW), the coldest and densest water mass on Earth [De Santis et al. 2018]. To the south, HSSW descends beneath the ice shelf towards the ice shelf base. The freezing point drops down as the pressure increases, therefore the warmer HSSW partially melt the ice near the base [Smethie and Jacobs 2005]. The resulting Ice Shelf Water (ISW) flows upward along the ice shelf base with partial refreezing due to the restored freezing point, forming modified Ice Shelf Water (mISW) that feeds the sea ice production.

Changes in ocean circulation can affect basal layer characteristics [Pritchard et al. 2012;

Hellmer et al. 2012]. While the Ross Ice Shelf is considered stable, a redirection of coastal or regional currents [Hellmer et al. 2012; Jacobs et al. 2011] could enhance basal melting already identified near the RIS front [Horgan et al. 2011; Pritchard et al. 2012] and cause them to be more vulnerable to destabilization from gravity wave impacts. The thermodynamic interactions described above, when appreciable, will affect wave-induced ice-shelf mechanical response characteristics, connecting ice-shelf mechanical sensitivity to the atmospheric and oceanic environments.

1.3.2 Mechanical system

Ice shelves are also subject to mechanical interactions with the ocean environment, particularly within the spatiotemporal spectrum of gravity wave fluctuations, spanning local wind seas (>100 mHz), sea swell (30–100 mHz), and IG-wave periods (3–20 mHz) to tidal periods. Simplified as a plate model, seismic waves on an ice shelf can be analyzed with plate wave theory.

The simplest plate waves are Lamb waves, which propagate on a plate in a vacuum. There are two classes of Lamb waves, symmetric modes and antisymmetric modes. The symmetric modes produce extensional motions, thus also called extensional Lamb waves. The antisymmetric modes produce flexural motions, thus also called flexural Lamb Waves.

However, an ice shelf is a floating plate instead of one in vacuum, which requires plate wave theory to be adjusted [Press and Ewing 1951; Fox and Squire 1991]. The extensional motions of the ice shelf are not affected by the water below because water does not transfer shear stress. Therefore extensional Lamb waves are confined to the ice shelf. In contrast, the flexural motions of the ice shelf are significantly modified by the ocean/ice-shelf coupling, yielding flexural-gravity waves. At higher frequencies (>0.02 Hz for the Ross Ice Shelf), where the gravity restoring force does not affect the wave propagation significantly, the flexural-gravity waves are also called flexural waves.

Iceberg calving contributes about half of the mass loss in Antarctica (1321±144 gigatonnes per year) [Depoorter et al. 2013], which are preceded by rift formation and propagation. While the internal glaciological stress due to gravitational spreading of the ice may be the dominant driving force of the rift propagation and reduction in ice shelf integrity [Bassis et al. 2008], stress induced by ocean gravity wave impacts may also have a contribution [Sergienko 2010; Lipovsky 2018].

The link between ice shelf fractures and ocean gravity wave forcing was indirectly raised by the observation that sea swell incident on grounded giant iceberg B15A potentially had a role in the iceberg's catastrophic fragmentation [MacAyeal et al. 2006]. Seasonal loss of sea ice leaves the outer ice shelf margin directly impacted by swells, which may have contributed to the collapse of the Wilkins ice shelf [Massom et al. 2018]. Considering the persistent strong Southern Ocean storm activity and the associated intense ocean wave climate that continuously impacts ice shelves [Trenberth 1991; Tolman 2009; Chapman et al. 2015], ocean wave impacts likely play a role in ice shelf evolution. In addition to swell, longer-period gravity waves, e.g. infragravity waves and tsunamis, may also contribute to iceberg calving. For example, the tsunami generated by the March 11, 2011 Honshu earthquake may have triggered a 125-km^2 iceberg calved from the Sulzberger Ice Shelf [Brunt, Okal, and MacAyeal 2011]. Persistent infragravity waves and sporadic tsunamis are not damped by sea ice, as is swells, providing forcing to impact and weaken the ice shelves throughout the year.

1.3.3 Experiment on the Ross Ice Shelf

Both thermodynamic changes and mechanical changes relevant to ice shelf integrity affect ocean-excited seismic wave propagation across ice shelves. Monitoring and interpreting the resonance response characteristics and propagation characteristics of seismic waves through the ice-shelf/sub-shelf-water-cavity/basement system can be used to monitor changes in ice

shelf properties [Bromirski and Stephen 2012; MacAyeal et al. 2006]. Understanding ocean/ice-shelf interactions will improve modeling of ice-shelf/ice-sheet response to climate change, and consequently reduce the uncertainty in ice-sheet mass loss projections over the coming decades. Thus, it is important to quantify the spatial and temporal response of ice shelves to ocean gravity waves with in-situ measurements.

This motivated the multi-disciplinary, multi-investigator project to use proven seismological techniques to quantitatively examine ice shelf elastic properties by measuring the response of the Ross Ice Shelf to the ocean's mechanical impacts from the spectrum of ocean gravity waves. A broadband seismic array was deployed on the Ross Ice Shelf between October 2014 and November 2016 (Figure 1.2), with 3 near the shelf edge, 6 north-south orthogonal to the shelf front, 13 east-west parallel to the shelf front, and 10 clustered in a high-density array (aperture diameter = 40 km) at the intersection of the north-south and the east-west arrays (Figure 1.3). Each seismic station consisted of a self-leveling three-component Nanometrics T120 PHQ seismometers and Quanterra Q330 digitizers, buried in the ice at depth of $\sim$1.5 m (Figure 1.2). In addition, a three-component Nanometrics Trillium Compact broadband ocean bottom seismometer (OBS) system, which included a HighTech HTI-04-PCA/ULF pressure sensor, was deployed $\sim$6 km north of the ice front and 8 km north of DR01 between Jan 17 and Dec 11, 2015 (station KPDR in Figure 1.3a). The concurrent deployment of a near-front ocean bottom hydrophone to measure gravity wave forcing and near-front on-ice broadband seismic stations to measure the RIS response allows determination of an empirical frequency-dependent ocean-to-ice-shelf amplitude transfer function for the first time.

In Chapter 3, with the array on the Ross Ice Shelf and another broadband seismic array on the Pine Island Glacier ice shelf, plate waves are identified and compared, improving our knowledge on the ice shelf dynamics.

In Chapter 4, we present a comparison of gravity wave forcing of the Ross Ice Shelf measured by the ocean bottom hydrophone with the nearby broadband on-ice seismic observations.

The relative impact of gravity wave forcing on the Ross Ice Shelf integrity is inferred from the association of the icequake activity and the Ross Ice Shelf response amplitudes in very-long-period and swell bands.

Figures

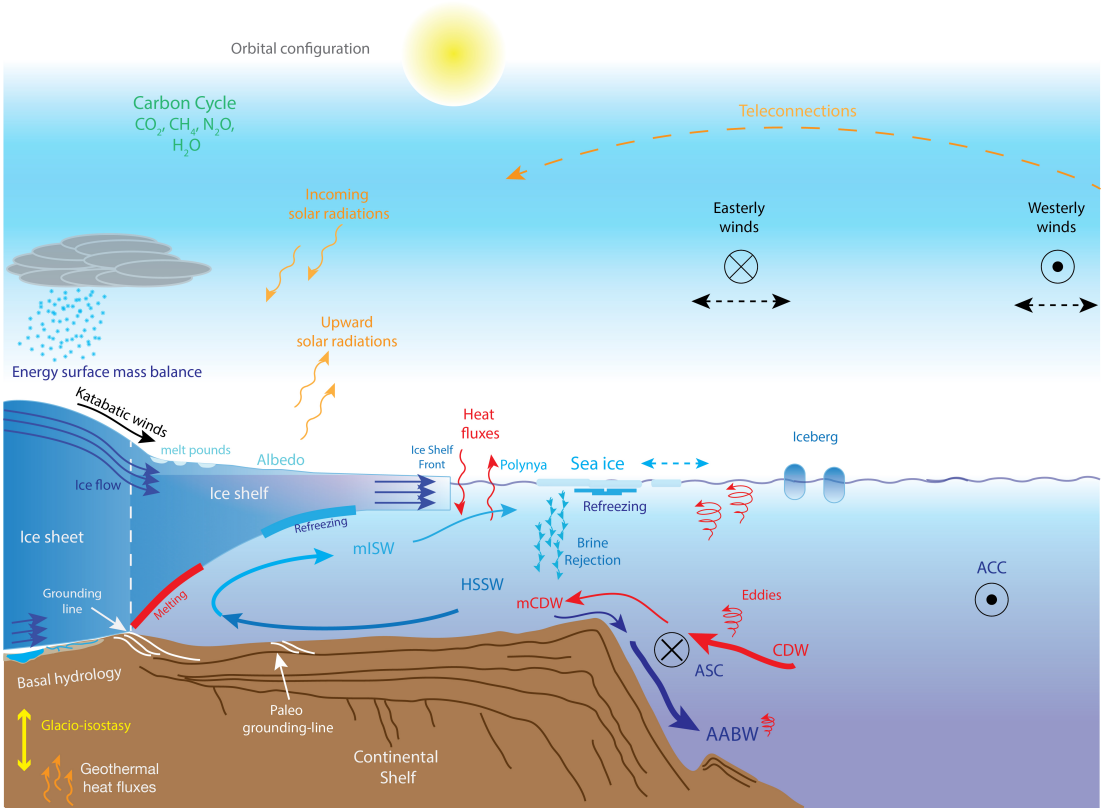

Figure 1.1: Schematic diagram of the Antarctic polar system, with the directions of the Antarctic Bottom Water (AABW), Antarctic Circumpolar Current (ACC), Antarctic Slope Current (ASC), Circumpolar Deep Water (CDW), and High-Salinity Shelf Water (HSSW), modified CDW (mCDW) and modified Ice Shelf Water (mISW) marked. Inward and outward flow directions are indicated by a circled X and a circled dot, respectively. Credit: Modified from [Colleoni et al. 2018]

.

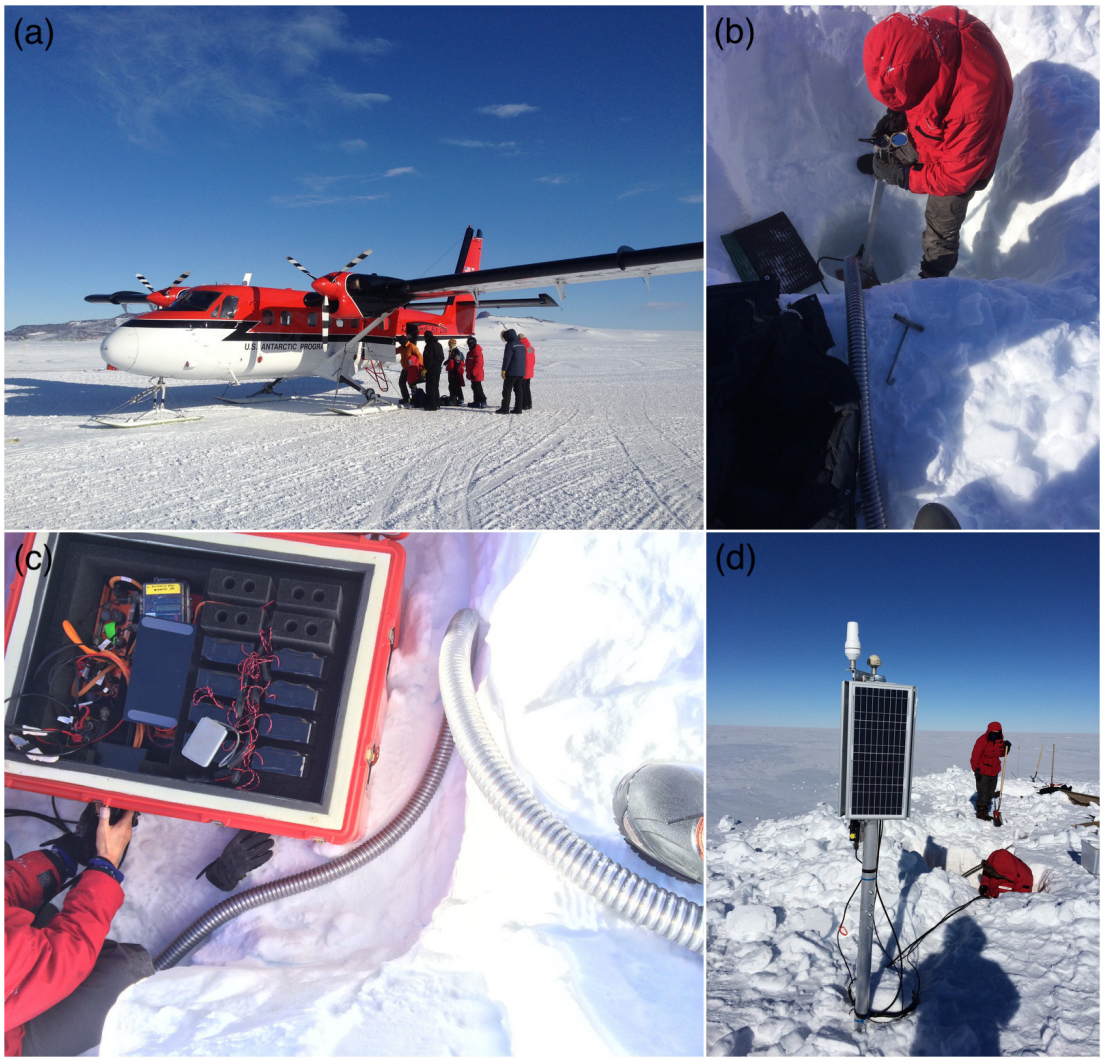

Figure 1.2: Photos of the field work in Antarctica. (a) A Twin Otter plane that carries the crews and equipments to the field. (b) Deployment of a seismic sensor. (c) Deployment of an equipment box with a Q330 digitizer, a B14 baler, and other supporting equipments. (d) A solar panel that provided power to the equipments in summer.

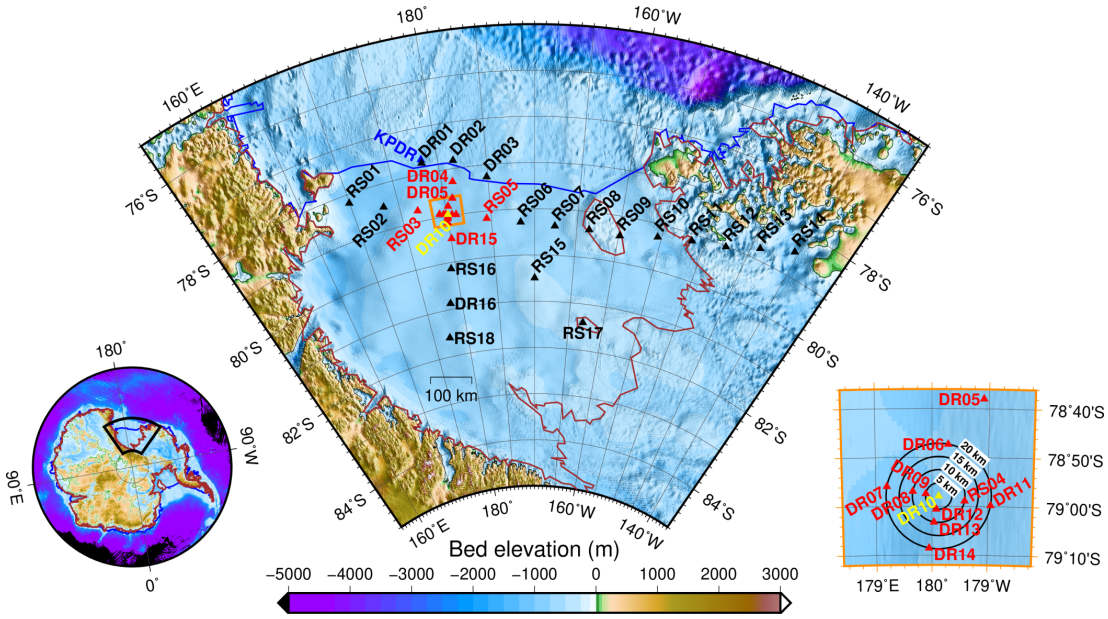

Figure 1.3: The Ross Ice Shelf seismic stations (triangles) superimposed on the bed elevation map [Fretwell et al. 2013], with the ocean bottom station KPDR (blue), the center station DR10 (yellow), extended center subarray (red) and other stations (black) indicated. The Ross Ice Shelf is bounded by the grounding line (brown line) and the ice front (blue line). Expanded view of the dense center subarray (orange box) is shown in the right inset, where the contours of distance to DR10 are shown (black circles). DR01, DR02, and DR03 are off the ice front because the ice front has moved northward, but the edge geometry data has not been updated.

References

Ardhuin, F., Gualtieri, L., and Stutzmann, E. (2015). "How ocean waves rock the Earth: Two mechanisms explain microseisms with periods 3 to 300 s". In: *Geophysical Research Letters* 42.3, pp. 765–772. DOI: 10.1002/2014GL062782.

Ardhuin, F., Stutzmann, E., Schimmel, M., and Mangeney, A. (2011). "Ocean wave sources of seismic noise". In: *Journal of Geophysical Research: Oceans* 116.C9. DOI: 10.1029/2011JC006952.

Bassis, J. N., Fricker, H. A., Coleman, R., and Minster, J.-B. (2008). "An investigation into the forces that drive ice-shelf rift propagation on the Amery Ice Shelf, East Antarctica". In: *Journal of Glaciology* 54.184, pp. 17–27. DOI: 10.3189/002214308784409116.

Bertelli, T. (1874). "Observacioni microsismiche". In: *Atti dell'Accademia Pontificia de'Nuovi Lincei* 27, pp. 429–464.

Bromirski, P. D. and Duennebier, F. K. (2002). "The near-coastal microseism spectrum: Spatial and temporal wave climate relationships". In: *Journal of Geophysical Research: Solid Earth* 107.B8, ESE 5-1–ESE 5-20. DOI: 10.1029/2001JB000265.

Bromirski, P. D., Duennebier, F. K., and Stephen, R. A. (2005). "Mid-ocean microseisms". In: *Geochemistry, Geophysics, Geosystems* 6.4. DOI: 10.1029/2004GC000768.

Bromirski, P. D., Flick, R. E., and Graham, N. (1999). "Ocean wave height determined from inland seismometer data: Implications for investigating wave climate changes in the NE Pacific". In: *Journal of Geophysical Research: Oceans* 104.C9, pp. 20753–20766. DOI: 10.1029/1999JC900156.

Bromirski, P. D., Sergienko, O. V., and MacAyeal, D. R. (2010). "Transoceanic infragravity waves impacting Antarctic ice shelves". In: *Geophysical Research Letters* 37.2. DOI: 10.1029/2009GL041488.

Bromirski, P. D. and Stephen, R. A. (2012). "Response of the Ross Ice Shelf, Antarctica, to ocean gravity-wave forcing". In: *Annals of Glaciology* 53.60, pp. 163–172. DOI: 10.3189/2012AoG60A058.

Brunt, K. M., Okal, E. A., and MacAyeal, D. R. (2011). "Antarctic ice-shelf calving triggered by the Honshu (Japan) earthquake and tsunami, March 2011". In: *Journal of Glaciology* 57.205, pp. 785–788. DOI: 10.3189/002214311798043681.

Cessaro, R. K. (1994). "Sources of primary and secondary microseisms". In: *Bulletin of the Seismological Society of America* 84.1, pp. 142–148.

Chapman, C. C., Hogg, A. M., Kiss, A. E., and Rintoul, S. R. (2015). "The dynamics of Southern Ocean storm tracks". In: *Journal of Physical Oceanography* 45.3, pp. 884–903. DOI: 10.1175/JPO-D-14-0075.1.

Colleoni, F., De Santis, L., Siddoway, C. S., Bergamasco, A., Golledge, N. R., Lohmann, G., Passchier, S., and Siegert, M. J. (2018). "Spatio-temporal variability of processes across Antarctic ice-bed-ocean interfaces". In: *Nature Communications* 9.1, p. 2289. DOI: 10.1038/s41467-018-04583-0.

De Santis, L., Colleoni, F., Bergamasco, A., Rebesco, M., Accettella, D., Kovacevic, V., Gales, J., Sookwan, K., and Olivo, E. (2018). "Exploring the unknown of the Ross Sea in sea ice-free conditions". In: *EOS* 99. DOI: 10.1029/2018EO106159.

Depoorter, M. A., Bamber, J. L., Griggs, J. A., Lenaerts, J. T. M., Ligtenberg, S. R. M., Broeke, M. R. van den, and Moholdt, G. (2013). "Calving fluxes and basal melt rates of Antarctic ice shelves". In: *Nature* 502, p. 89.

Farrell, W. E. and Munk, W. H. (2010). "Booms and Busts in the Deep". In: *Journal of Physical Oceanography* 40.9, pp. 2159–2169. DOI: 10.1175/2010JPO4440.1.

Fox, C. and Squire, V. A. (1991). "Coupling between the ocean and an ice shelf". In: *Annals of Glaciology* 15, pp. 101–108. DOI: 10.3189/1991AoG15-1-101-108.

Fretwell, P., Pritchard, H. D., Vaughan, D. G., Bamber, J. L., Barrand, N. E., Bell, R., Bianchi, C., Bingham, R. G., Blankenship, D. D., Casassa, G., Catania, G., Callens, D., Conway, H., Cook, A. J., Corr, H. F. J., Damaske, D., Damm, V., Ferraccioli, F., Forsberg, R., Fujita, S., Gim, Y., Gogineni, P., Griggs, J. A., Hindmarsh, R. C. A., Holmlund, P., Holt, J. W., Jacobel, R. W., Jenkins, A., Jokat, W., Jordan, T., King, E. C., Kohler, J., Krabill, W., Riger-Kusk, M., Langley, K. A., Leitchenkov, G., Leuschen, C., Luyendyk, B. P., Matsuoka, K., Mouginot, J., Nitsche, F. O., Nogi, Y., Nost, O. A., Popov, S. V., Rignot, E., Rippin, D. M., Rivera, A., Roberts, J., Ross, N., Siegert, M. J., Smith, A. M., Steinhage, D., Studinger, M., Sun, B., Tinto, B. K., Welch, B. C., Wilson, D., Young, D. A., Xiangbin, C., and Zirizzotti, A. (2013). "Bedmap2: improved ice bed, surface and thickness datasets for Antarctica". In: *Cryosphere* 7.1, pp. 375–393. DOI: 10.5194/tc-7-375-2013.

Gerstoft, P. and Tanimoto, T. (2007). "A year of microseisms in southern California". In: *Geophysical Research Letters* 34.20. DOI: 10.1029/2007GL031091.

Gille, S. T. (2008). "Decadal-Scale Temperature Trends in the Southern Hemisphere Ocean". In: *Journal of Climate* 21.18, pp. 4749–4765. DOI: 10.1175/2008JCLI2131.1.

Grevemeyer, I., Herber, R., and Essen, H.-H. (2000). "Microseismological evidence for a changing wave climate in the northeast Atlantic Ocean". In: *Nature* 408, pp. 349–352. DOI: 10.1038/35042558.

Hasselmann, K. (1963). “A statistical analysis of the generation of microseisms”. In: *Reviews of Geophysics* 1.2, pp. 177–210. DOI: 10.1029/RG001i002p00177.

Hellmer, H. H., Kauker, F., Timmermann, R., Determann, J., and Rae, J. (2012). “Twenty-first-century warming of a large Antarctic ice-shelf cavity by a redirected coastal current”. In: *Nature* 485, pp. 225–228. DOI: 10.1038/nature11064.

Herbers, T. H. C., Elgar, S., and Guza, R. T. (1995). “Generation and propagation of infragravity waves”. In: *Journal of Geophysical Research: Oceans* 100.C12, pp. 24863–24872. DOI: 10.1029/95JC02680.

Holland, D. M., Thomas, R. H., Young, B. de, Ribergaard, M. H., and Lyberth, B. (2008). “Acceleration of Jakobshavn Isbræ triggered by warm subsurface ocean waters”. In: *Nature Geoscience* 1, pp. 659–664. DOI: 10.1038/ngeo316.

Horgan, H. J., Walker, R. T., Anandakrishnan, S., and Alley, R. B. (2011). “Surface elevation changes at the front of the Ross Ice Shelf: Implications for basal melting”. In: *Journal of Geophysical Research: Oceans* 116.C2. DOI: 10.1029/2010JC006192.

Jacobs, S. S., Jenkins, A., Giulivi, C. F., and Dutrieux, P. (2011). “Stronger ocean circulation and increased melting under Pine Island Glacier ice shelf”. In: *Nature Geoscience* 4, pp. 519–523. DOI: 10.1038/ngeo1188.

Kedar, S., Longuet-Higgins, M., Webb, F., Graham, N., Clayton, R., and Jones, C. (2008). “The origin of deep ocean microseisms in the North Atlantic Ocean”. In: *Proceedings of the Royal Society A: Mathematical, Physical and Engineering Science* 464.2091, pp. 777–793. DOI: 10.1098/rspa.2007.0277.

Lipovsky, B. P. (2018). “Ice Shelf Rift Propagation and the Mechanics of Wave-Induced Fracture”. In: *Journal of Geophysical Research: Oceans* 123. DOI: 10.1029/2017JC013664.

Longuet-Higgins, M. S. (1950). “A theory of the origin of microseisms”. In: *Philosophical Transactions of the Royal Society of London. Series A, Mathematical and Physical Sciences* 243.857, pp. 1–35. DOI: 10.1098/rsta.1950.0012.

MacAyeal, D. R. (1987). “Ice-Shelf Backpressure: Form Drag Versus Dynamic Drag”. In: *Dynamics of the West Antarctic Ice Sheet*. Ed. by C. J. Van der Veen and J. Oerlemans. Dordrecht: Springer Netherlands, pp. 141–160. ISBN: 9789400937451.

MacAyeal, D. R., Okal, E. A., Aster, R. C., Bassis, J. N., Brunt, K. M., Cathles, L. M., Drucker, R., Fricker, H. A., Kim, Y.-J., Martin, S., Okal, M. H., Sergienko, O. V., Sponsler, M. P., and Thom, J. E. (2006). “Transoceanic wave propagation links iceberg calving margins of Antarctica with storms in tropics and Northern Hemisphere”. In: *Geophysical Research Letters* 33.17. DOI: 10.1029/2006GL027235.

Massom, R. A., Scambos, T. A., Bennetts, L. G., Reid, P., Squire, V. A., and Stammerjohn, S. E. (2018). "Antarctic ice shelf disintegration triggered by sea ice loss and ocean swell". In: *Nature* 558.7710, pp. 383–389. DOI: 10.1038/s41586-018-0212-1.

Müller, M., Arbic, B. K., Richman, J. G., Shriver, J. F., Kunze, E. L., Scott, R. B., Wallcraft, A. J., and Zamudio, L. (2015). "Toward an internal gravity wave spectrum in global ocean models". In: *Geophysical Research Letters* 42.9, pp. 3474–3481. DOI: 10.1002/2015GL063365.

Munk, W. H., Miller, G. R., Snodgrass, F. E., and Barber, N. F. (1963). "Directional Recording of Swell from Distant Storms". In: *Philosophical Transactions of the Royal Society of London A: Mathematical, Physical and Engineering Sciences* 255.1062, pp. 505–584. DOI: 10.1098/rsta.1963.0011.

Orsi, A. H. and Wiederwohl, C. L. (2009). "A recount of Ross Sea waters". In: *Deep Sea Research Part II: Topical Studies in Oceanography* 56.13. Southern Ocean Shelf Slope Exchange, pp. 778–795. DOI: 10.1016/j.dsr2.2008.10.033.

Paolo, F. S., Fricker, H. A., and Padman, L. (2015). "Volume loss from Antarctic ice shelves is accelerating". In: *Science* 348.6232, pp. 327–331. DOI: 10.1126/science.aaa0940.

Press, F. and Ewing, M. (1951). "Propagation of elastic waves in a floating ice sheet". In: *Eos, Transactions American Geophysical Union* 32.5, pp. 673–678. DOI: 10.1029/TR032i005p00673.

Pritchard, H. D., Ligtenberg, S. R. M., Fricker, H. A., Vaughan, D. G., Broeke, M. R. van den, and Padman, L. (2012). "Antarctic ice-sheet loss driven by basal melting of ice shelves". In: *Nature* 484, pp. 502–505. DOI: 10.1038/nature10968.

Rignot, E., Casassa, G., Gogineni, P., Krabill, W., Rivera, A., and Thomas, R. (2004). "Accelerated ice discharge from the Antarctic Peninsula following the collapse of Larsen B ice shelf". In: *Geophysical Research Letters* 31.18. DOI: 10.1029/2004GL020697.

Scambos, T. A., Bohlander, J. A., Shuman, C. A., and Skvarca, P. (2004). "Glacier acceleration and thinning after ice shelf collapse in the Larsen B embayment, Antarctica". In: *Geophysical Research Letters* 31.18. DOI: 10.1029/2004GL020670.

Scambos, T. A., Fricker, H. A., Liu, C.-C., Bohlander, J., Fastook, J., Sargent, A., Massom, R., and Wu, A.-M. (2009). "Ice shelf disintegration by plate bending and hydro-fracture: Satellite observations and model results of the 2008 Wilkins ice shelf break-ups". In: *Earth and Planetary Science Letters* 280.1, pp. 51–60. DOI: 10.1016/j.epsl.2008.12.027.

Scambos, T. A., Hulbe, C., Fahnestock, M., and Bohlander, J. (2000). "The link between climate warming and break-up of ice shelves in the Antarctic Peninsula". In: *Journal of Glaciology* 46.154, pp. 516–530. DOI: 10.3189/172756500781833043.

Sergienko, O. V. (2010). "Elastic response of floating glacier ice to impact of long-period ocean waves". In: *Journal of Geophysical Research: Earth Surface* 115.F4. DOI: 10.1029/2010JF001721.

Shapiro, N. M. and Campillo, M. (2004). "Emergence of broadband Rayleigh waves from correlations of the ambient seismic noise". In: *Geophysical Research Letters* 31.7. DOI: 10.1029/2004GL019491.

Shepherd, A., Wingham, D., Payne, T., and Skvarca, P. (2003). "Larsen Ice Shelf Has Progressively Thinned". In: *Science* 302.5646, pp. 856–859. DOI: 10.1126/science.1089768.

Smethie, W. M. and Jacobs, S. S. (2005). "Circulation and melting under the Ross Ice Shelf: estimates from evolving CFC, salinity and temperature fields in the Ross Sea". In: *Deep Sea Research Part I: Oceanographic Research Papers* 52.6, pp. 959–978. DOI: 10.1016/j.dsr.2004.11.016.

Thoma, M., Jenkins, A., Holland, D., and Jacobs, S. S. (2008). "Modelling Circumpolar Deep Water intrusions on the Amundsen Sea continental shelf, Antarctica". In: *Geophysical Research Letters* 35.18. DOI: 10.1029/2008GL034939.

Tolman, H. L. (2009). "User manual and system documentation of WAVEWATCH III TM version 3.14". In: *Technical Note, MMAB Contribution* 276.

Traer, J. and Gerstoft, P. (2014). "A unified theory of microseisms and hum". In: *Journal of Geophysical Research: Solid Earth* 119.4, pp. 3317–3339. DOI: 10.1002/2013JB010504.

Trenberth, K. E. (1991). "Storm tracks in the Southern Hemisphere". In: *Journal of the Atmospheric Sciences* 48.19, pp. 2159–2178. DOI: 10.1175/1520-0469(1991)048<2159:STITSH>2.0.CO;2.

Uchiyama, Y. and McWilliams, J. C. (2008). "Infragravity waves in the deep ocean: Generation, propagation, and seismic hum excitation". In: *Journal of Geophysical Research: Oceans* 113.C7. DOI: 10.1029/2007JC004562.

Webb, S. C. (1998). "Broadband seismology and noise under the ocean". In: *Reviews of Geophysics* 36.1, pp. 105–142. DOI: 10.1029/97RG02287.

Yang, Y. and Ritzwoller, M. H. (2008). "Characteristics of ambient seismic noise as a source for surface wave tomography". In: *Geochemistry, Geophysics, Geosystems* 9.2. DOI: 10.1029/2007GC001814.

Chapter 2

Microseism Source Direction Identification

Inhomogeneous noise sources surrounding stations produce asymmetric amplitudes in cross-correlation functions that yield preferential source directions. Here we show that preprocessing biases the dominant source direction estimate towards the source producing long-duration signals by down-weighting high-amplitude signals. Tests with both synthetic data and observations show that conventional preprocessing, where only earthquakes and local transients (e.g. trawling, fish impacts) are removed, is more sensitive to coherent energy, while one-bit preprocessing and running-absolute-mean (RAM) preprocessing are more influenced by signal duration. Comparisons between different preprocessing methods are made on data from the Cascadia Initiative (CI) ocean bottom seismometer (OBS) array, where we find that the total energy arriving from pelagic and coastal areas is similar. Moreover, pelagic-generated signals tend to be weaker but have longer duration, in contrast to coastal-generated signals that tend to be stronger but have shorter duration.

2.1 Introduction

Conventional seismic tomography has been extensively used to study the Earth's structure, see reviews by [Romanowicz 1991; Romanowicz 2003]. However, as earthquake sources are spatially restricted, the more widely distributed ambient noise sources provide another important resource to study Earth structure. It has been demonstrated that Green's functions can be extracted from the ambient noise cross-correlation functions [Snieder 2004; Sato and Fehler 2009], which became the foundation of ambient noise tomography. However, the reliability of the extracted Green's functions depends on the validity of the assumption that the noise sources are homogeneously distributed. Although seismic data preprocessing, especially one-bit and RAM, serves to better spatially homogenize the noise field that allows unbiased estimates of travel times [Shapiro et al. 2005; Harmon, Rychert, and Gerstoft 2010] and usually increases SNR for surface waves, absolute amplitude information is lost. Besides, ambient noise has also been used for crustal attenuation estimation [e.g. Prieto, Lawrence, and Beroza 2009; Lin, Tsai, and Ritzwoller 2012]. However, noise source distribution has an effect on the coherency amplitude decay rate with station separation, which is important for attenuation coefficient estimation [Tsai 2011]. Therefore, it is important to study the distribution of noise sources to investigate whether a homogeneous source distribution assumption is valid, and to determine the impact on cross-correlation functions if it is not [Yao and Van Der Hilst 2009; Cupillard and Capdeville 2010; Harmon, Rychert, and Gerstoft 2010].

Microseisms (0.05–0.35 Hz) have been studied for several decades, with the dominant source area of double-frequency (DF) microseisms (0.1–0.35 Hz) an important but unresolved issue [Bromirski, Stephen, and Gerstoft 2013]. It is generally accepted that single-frequency (SF) microseisms (0.05–0.1 Hz) are generated by the interaction between the ocean waves and the seafloor near coasts [Hasselmann 1963], while DF microseisms are generated by counter-propagating, or more generally, obliquely interacting surface waves [Longuet-Higgins 1950;

Traer and Gerstoft 2014]. For the SF band, all studies support shallow water generation [Cessaro 1994; Bromirski and Duennebier 2002], consistent with the theoretical work by [Hasselmann 1963]. For the DF band, however, both pelagic generation [Bromirski, Duennebier, and Stephen 2005; Kedar et al. 2008; Ardhuin et al. 2011] and near-coastal generation [Bromirski, Flick, and Graham 1999; Bromirski, Duennebier, and Stephen 2005; Gerstoft and Tanimoto 2007; Yang and Ritzwoller 2008; Ardhuin et al. 2011] have been identified. Some studies support one dominant source area, while others conclude both source areas are important, rendering this topic still under debate. Sensor location, on land or on the deep seafloor, is an important consideration. Most previous studies on this topic relied on land data alone, which limits its ability to distinct pelagic and coastal generated signals. Spanning both continental shelf and pelagic regions, the Cascadia Initiative (CI) ocean bottom seismometer (OBS) array (Figure 2.1) may help to resolve DF source location issues.

Noise cross-correlation has been widely used for estimating source directions. Additionally, preprocessing has also been implemented in most, if not all, previous microseism source direction studies using noise cross-correlation [e.g. Yang and Ritzwoller 2008; Tian and Ritzwoller 2015]. Among various preprocessing methods, one-bit normalization [Campillo and Paul 2003] is one of the most popular approaches since it's straightforward and produces cross-correlation functions with high signal-to-noise-ratio (SNR). However, its weakness is that it normalizes amplitudes and thus distorts the coherent energy information between stations. A detailed demonstration will be given in Section 2.3. Similarly, another popular preprocessing method, RAM [Bensen et al. 2007], also discards amplitude information. Amplitude information loss can affect cross-correlation functions, and thus biasing dominant source direction estimation towards the source producing long-duration signals regardless of the signal amplitude. (To be clear, we define the dominant source to be the source of the strongest signal arriving at the station pair, even though the source itself could be weaker than other sources.) We will show that SNR of the cross-correlation function, generally the criterion for determining dominant source direction, is

unreliable with RAM preprocessing. In this paper, we will compare cross-correlation functions from different preprocessing methods, and show the weakness of some preprocessing methods for estimating dominant source direction. Then we apply these methods to dominant source direction estimation for the Cascadia region.

2.2 Background

To investigate the effects of data preprocessing on microseism source direction estimates using noise cross-correlation, the following preprocessing methods are compared: (1) Conventional preprocessing: only remove earthquakes and other transients (e.g. trawling, fish impacts). (2) One-bit: only the sign of the records are kept for cross-correlation [Campillo and Paul 2003]. (3) Clipping: truncating signals above a given threshold after conventional preprocessing. Higher clipping thresholds preserve more of the original data. A low threshold (more severe clipping) gives results similar to the one-bit method. (4) Running absolute mean (RAM): normalize the waveform by the running average of the absolute value of waveform in a RAM window centered at the normalization point [Bensen et al. 2007]. The RAM method is given by

$$\tilde{d}_n = \frac{d_n}{w_n} \tag{2.1}$$

where d_n is the raw or filtered seismogram, $\tilde{d}_n$ is the normalized data. w_n is the normalization factor determined from

$$w_n = \frac{1}{2N+1} \sum_{j=n-N}^{n+N} |d_j| \tag{2.2}$$

where the RAM window length is $(2N+1)$ samples. Similar to the clipping method, RAM is also an intermediate method between keeping the raw data and one-bit preprocessing. This is controlled by the RAM window length [Bensen et al. 2007].

If $N = 0$, then

$$w_n = \frac{1}{2\times 0+1}\sum_{j=n-0}^{n+0}|d_j| = |d_n| \tag{2.3}$$

$$\tilde{d_n} = \frac{d_n}{w_n} = \frac{d_n}{|d_n|} = \mathrm{sgn}(d_n) \tag{2.4}$$

Therefore, RAM with $N = 0$, i.e. the RAM window length is one sample, is equivalent to one-bit.

As $N \to \infty$, then

$$\lim_{N\to\infty} w_n = \lim_{N\to\infty}\frac{1}{2N+1}\sum_{j=n-N}^{n+N}|d_j| = \overline{|d_j|} \tag{2.5}$$

where $\overline{|d_j|}$ is the mean of the absolute value of the entire data d_j. Therefore, $\lim_{N\to\infty} w_n$ is a constant series. Thus $\tilde{d_n}$ approaches a re-scaled d_n with a very long window. Thus for large N, RAM and conventional preprocessing (with earthquakes and other transients retained) are similar.

Here, the RAM window length is set to half the maximum period of the bandpass filter as suggested by [Bensen et al. 2007], and as applied in most studies using the RAM method. For the DF frequency band 0.115–0.145 Hz, the RAM window length is $\frac{1}{2}\times\frac{1}{0.115\,\mathrm{Hz}} \approx 4.3\,\mathrm{s}$. As the sampling rate is 1 Hz, we select $N = 2$, giving $2N+1 = 5$ samples for the RAM window. For such a short window, RAM is expected to give similar results as one-bit.

The cross-correlation, $C_{12}(\tau)$ of preprocessed records $r_1(t)$ and $r_2(t)$ is obtained from

$$C_{12}(\tau) = \frac{1}{T}\int_0^T r_1(t+\tau)r_2(t)\mathrm{d}t \tag{2.6}$$

where τ is the lag, and T is the length of the chosen data segment.

Sources on opposite sides of the station-pair, $C_{12}(\tau)$ produce peaks at both positive and negative lags. Based on stationary phase approximation, the contribution of the sources near the station axis dominates the cross-correlation function [Snieder 2004]. Therefore, the two peaks

correspond to two opposite source directions near the station axis, respectively. The relative amplitudes of the peaks are used as an indicator of the energy propagating in the corresponding directions. This is obvious for non-dispersive case as $C_{12}(\tau)$ reaches its peak and equals the product of the signal energy and a geometric spreading factor when τ is equal to the travel time,as demonstrated in section 2.3. We assume this relation approximately holds for dispersive cases. Then the higher peak corresponds to the dominant direction from which energy is propagating. Note that any normalization of the records r_1 and r_2 will lose amplitude information and make it difficult to obtain the signal energy ratio from cross-correlation. Thus this dominant source direction estimation method is more compatible with conventional preprocessing than the other three preprocessing methods.

Dominant source direction analysis for an array is more complex than for a single station-pair because of different site effects and different station separations. SNR is used to reduce the influence of site effects by normalizing the signal power by the site-dependent background noise level. Here, SNR is defined by the ratio between the peak of $C_{12}(\tau)$ and the root-mean-square (RMS) of $C_{12}(\tau)$'s tail. The tail is defined as $|\tau|$ between 1500 s and 2000 s, with the maximum lag in cross-correlation set to 2000 s. For a maximum station-pair separation of 601.5 km as in Section 2.6, this background noise estimation methodology should work if the average group velocity is larger than 601.5 km/1500 s = 0.40 km/s. This holds true for most of the station pairs except for some station pairs within the thick sediment region. However, these station pairs are uncommon and oriented mostly north-south. Thus, these station pairs won't influence the investigation of whether shallow water (east) or deep water (west) is the dominant source direction.

Because of the relationship between cross-correlation functions and Green's functions, the RMS of cross-correlation function tails is related to scattered energy [Stehly et al. 2008], and can be anisotropic because of inhomogeneous source and scatterer distributions. Consequently, the background noise level is estimated by the RMS of the tails of cross-correlation functions on

both sides. In addition, SNR depends on station separation because each station could be regarded as a virtual source and Rayleigh wave amplitudes decay as $1/\sqrt{d}$ due to geometric spreading, where d is the propagation distance, while background noise is independent of d. To account for the effect of spreading losses, we define range-scaled SNR (RSNR) to be

$$\text{RSNR} = \text{SNR} \times \sqrt{d/d_0} \tag{2.7}$$

where d_0 is set to 70 km, approximately equal to the neighboring station separation.

We will show the advantage of RSNR in Section 2.6. The dominant source direction will be determined based on RSNR except for single station-pair cases, for which peak height comparison is sufficient.

2.3 Synthetic test

The impact of preprocessing on direction estimates was investigated for counter-propagating synthetic signals with different power and duration. The effects of different preprocessing methodologies were determined by comparing cross-correlation functions (determined with Equation 2.6).

The model geometry is shown in Figure 2.2(a), where S_m ($m = 1,2$) represents source i, and R_n ($n = 1,2$) receiver j. The corresponding lower-case letters, i.e. s_m and r_n, represent the source time function and the receiver record, respectively. Only vertical component responses are examined. The source time functions are formed from a 1 sample/s Gaussian time series with a 50% Tukey window and a 0.05–0.35 Hz (microseism frequency band) Butterworth passband filter applied (Figures 2.2(c) and (d)). s_1 has a smaller amplitude (RMS = 0.62) and longer duration (4096 s), while s_2 has higher amplitude (RMS = 6.17) but shorter duration (256 s). The source spectrum is calculated by Welch's method [Welch 1967] with 64-s segments (50% overlap)

(Figure 2.2(b)). s_2 has higher spectral levels than s_1 over the entire frequency band. The onset time of s_1 and s_2 are 100 s and 2000 s respectively.

The vertical component of s_m propagated to R_n, denoted by r_{mn}, is obtained by the product of the source function in frequency domain $s_m(\omega)$ and the vertical-vertical component of the Rayleigh wave Green's function [Aki and Richards 2002].

$$r_{mn}(\omega) = s_m(\omega)\frac{\exp\left[-i(kd_{mn} - \frac{\pi}{4})\right]}{\sqrt{\frac{\pi}{2}kd_{mn}}} \tag{2.8}$$

where i is the imaginary unit. d_{mn} represents the distance between source S_m and receiver R_n. k is the wavenumber calculated by assuming a constant phase velocity, $c = 2.5$ km/s.
RMS of the propagated signals (averaged over the signal duration) is obtained as

$$\mathrm{RMS}(r_{11}) \approx 0.046, \mathrm{RMS}(r_{12}) \approx 0.022$$

$$\mathrm{RMS}(r_{21}) \approx 0.221, \mathrm{RMS}(r_{22}) \approx 0.461$$

The distance of the receiver from respective sources determines which signal dominates. When s_2 signal arrives at the receiver, it dominates over the signal from s_1. Otherwise the s_1 signal dominates (Figures 2.2(e) and (f)). Thus, because s_1 is 15 times longer than s_2, s_1 dominates more of the time. The summation of r_{1m} and r_{2m} constitutes the coherent signal at receiver R_m. To include the influence of incoherent background noise, low amplitude incoherent Gaussian noise (RMS $= 0.01$) was added to the coherent signal to constitute a more realistic receiver record r_m.

Cross-correlation functions between r_1 and r_2 are shown in Figures 2.2(g) and (h). The peak at negative lag (peak 1) corresponds to the signal from S_1, while the peak at positive lag (peak 2) corresponds to the signal from S_2. Note that both methods give accurate travel times ($d_{12}/c = 1000\mathrm{km}/2.5\mathrm{km\,s^{-1}} = 400$ s). However, conventional cross-correlation indicates a dominant signal from S_2, while one-bit cross-correlation indicates a dominant signal from S_1.

Specifically, the ratio between peak 2 and peak 1 is 5.8 in conventional cross-correlation function, which is close to the ratio between the arrival energy from the two sources $\sum r_{22}^2 / \sum r_{11}^2 = 6.4$. In contrast, this ratio is much less than 1 in one-bit cross-correlation function as peak 2 is almost invisible. This is because conventional preprocessing conserves amplitude information and gives the correct dominant source direction, while one-bit preprocessing normalizes the received signal per time unit, thus over-emphasizing the long-duration weak signals from S_1. Therefore, conventional preprocessing is a better choice for dominant source direction estimation.

2.4 Method comparisons for a selected station-pair

Different preprocessing methods on CI OBS observations affect DF microseism noise cross-correlation source direction estimation. The 2012 CI OBS array covers the Juan de Fuca Plate with inter-station separation of $\sim$ 70 km, see Figure 2.1). Available stations in March 2012 include 13 shallow-water (depth $<$ 200 m) stations, 9 intermediate-depth (200 m $<$ depth $<$ 2000 m) stations, and 31 deep-water (depth $>$ 2000 m) stations. Twenty of the 53 available OBSs were designed to record along the continental shelf and slope of the Cascadia margin at less than 1000-m depth [Toomey et al. 2014]. However, we choose deep-water station-pair J31A and J30A because deep-water stations have higher SNR in cross-correlation functions because they do not include overhead ocean wave direct-pressure signals that decay exponentially with depth (described as hydrodynamic filtering), which could reduce SNR.

Observations at J31A (depth: 2657 m) and J30A (depth: 2824 m) during March 2012 were bandpass filtered from 0.115–0.145 Hz after correcting for the instrument response to displacement. This frequency band belongs to ocean-swell-generated longer-period double-frequency band in [Bromirski, Duennebier, and Stephen 2005], with further justification for choosing this band provided in Section 2.6. For clipping preprocessing, the records were divided into 31 single-day segments. The median of the 10 smallest RMS of these segments represents

the noise level, denoted by RMS_{noise}. The clipping thresholds are obtained by multiplying RMS_{noise} by different factors (0.5, 5, 10, 20, higher thresholds give less clipping). Clipping with a sufficiently low threshold is used to minimize the effect of earthquake signals and other short-duration high-amplitude transients.

Although various preprocessing methods produce cross-correlation functions with peaks at similar lags (i.e. similar travel times), the ratios between the amplitudes of the two peaks at the positive and negative lag sides are significantly different, demonstrated in Figure 2.3. Note that the negative lag peak corresponds to signals coming from west, with positive lag from the east. The ratio of the two peaks allows comparison of counter-propagating signals for one station-pair because the same background noise level and station separation would be used to calculate RSNR of both sides of the cross-correlation function. The conventional cross-correlation function has similar peak amplitudes on both sides, indicating no dominant source direction. Lowering clipping thresholds (increasing the amount of clipping) increases the ratio between the left and right peaks. One-bit and RAM preprocessing give similar cross-correlation functions as the strong factor of 0.5 clipping preprocessing, indicating a prominent dominant signal from west.

Since preprocessing methods have such a significant influence on dominant source direction estimation, it is important to investigate changes in direction estimates over time for a particular event. We compare conventional preprocessing and one-bit preprocessing, which represents no-clipping (but earthquakes have been removed) and extreme clipping (RAM preprocessing with 5-point window length gives cross-correlation function peak levels similar to one-bit preprocessing). This shows differences between the cases at both ends of the clipping spectrum (Figure 2.3). Amplitude and spectral characteristics are examined for the same station-pair (J30A and J31A) and frequency band (0.115–0.145 Hz) during March 4–7 observations. There was a small local earthquake on Mar. 6, which was removed in conventional preprocessing (Figure 2.4(b) and (d)). It is almost invisible in 0.115–0.145 Hz. Similar results were obtained without removing this earthquake. Note that the first two days have higher power in the 0.115–0.145 Hz

band, but have lower power in the 0.2–0.3 Hz band (Figure 2.4(a) and (c)), suggesting different source characteristics for the 0.115–0.145 Hz and 0.2–0.3 Hz microseism components. Consistent with the observations, wave model hindcast significant-wave-height H_s (WAVEWATCH-III^{TM} [Tolman 2009]) indicate ocean wave arrivals from strong distant storm in the first two days, followed by weak local storm events, and then quiet wave activity during the last two days. Cross-correlation functions are given for the first two days (Figure 2.5(a) and (b)), last two days (Figure 2.5(c) and (d)), all four days (Figure 2.5(e) and (f)), and also whole March (Figure 2.5(g) and (h)).

Both preprocessing methods indicate a dominant signal from east during Mar. 4–5 and a dominant signal from west during Mar. 6–7. These results are consistent with coastal generation dominating when strong swell is present in shallow near-coastal water, with pelagic generation dominating otherwise.

The two methods indicate different dominant source directions for the combined time period, i.e. March 4–7. Conventional cross-correlation indicates a dominant signal from east while one-bit cross-correlation indicates a dominant signal from the west. Additionally, the two methods also give different results for the whole month. Conventional cross-correlation indicates similar-strength signals from two directions while one-bit cross-correlation consistently indicates a dominant signal from the west.

Recall the synthetic test (Figure 2.2), the difference between the source amplitude and duration characteristics could contribute to this distinction. Hindcast H_s spanning March 2012 show episodic distant storm waves and strong regionally-generated storm waves reaching the coastal region, likely producing relatively short-duration but high amplitude signals there. However, as these strong coastal-generated signals have short duration, persistent pelagic-generated signals could dominate most of the time, thus producing the differences between the two cross-correlation functions. One-bit normalization accentuates the pelagic-generated long-duration and but relatively weak signals, thus biasing the dominant source direction estimation. In order to

examine the validity of this conjecture, we need to examine the source characteristics in coastal and pelagic areas.

2.5 Source characteristics analysis

The microseism power is assumed to be closely associated with ocean wave power (OWP) variability at deep-water and shallow-water stations. J31A (depth: 2657 m) and J25A (depth: 142.8 m) were chosen as representative deep-water and shallow-water stations, respectively. The power evolution over Mar. 2012 is characterized by the hourly mean of the squared 0.115–0.145-Hz filtered seismogram, see Figure 2.6(a). Spikes appearing in both curves indicate large earthquakes, while spikes occurring only at shallow water J25A may result from small local earthquakes or local transients cased by, e.g., trawling or fish impacts. OWP is estimated from

$$P \approx \frac{1}{2} Ec = \frac{\rho g^2}{32\pi} H_s^2 T_p \tag{2.9}$$

where E is the wave energy, c is the wave phase speed, T_p is the peak wave period [Kinsman 1965]. Modeled H_s and T_p are available from WAVEWATCH III model. OWP at the two stations are obtained by spatial linear interpolation of the OWP at the nearest grid points, see Figure 2.6(b). The spatial grid interval is 0.5°. The shallow-water seismic spectrogram has a larger dynamic range due to the exceptionally high peaks. Most of the episodic broad seismic power peaks are coincident with shallow-water OWP peaks (e.g. Mar. 5, 10, 12, 21). Shallow-water OWP peaks generally follow deep-water OWP peaks because swell comes from deep water, although local storms intensifying nearer the coast can produce the opposite relationship (e.g. Mar. 27). The coincidence between seismic power peaks and shallow water OWP peaks indicates that shallow water is the dominant source area of 0.115–0.145-Hz microseisms when strong swell is present. The seismic power peaks are occasionally not coincident with the OWP peaks. Seismic peaks

with no corresponding OWP peaks could indicate a pelagic storm from which the swell did not arrive at the array and/or microseisms generated at remote coastal locations. OWP peaks with no corresponding seismic peaks may result from a lack of counter-propagating or obliquely interacting waves.

As shown previously (Figure 2.2), conventional cross-correlation is more sensitive to signal power while one-bit and RAM cross-correlation are more sensitive to signal duration. To investigate the power and duration characteristics of the sources, we calculate the ratio of the the 5% strongest segments' power to the total power in 0.115–0.145 Hz band. Specifically, the record is 0.115–0.145-Hz bandpass filtered and then divided into consecutive 1-hour segments. Segments with earthquakes, missing data, or local transients (e.g. trawling, fish impacts) are removed. When a time segment is removed in one station record, the corresponding time segment is removed for all stations. The energy of each segment is represented by the mean of the squared record. The total energy of the 5% strongest segments are calculated and divided by the total energy of all segments. This ratio reflects the percentage the strongest 5% segments possess of the total energy. Thus, a larger ratio indicates more energy concentrated in the 5% most energetic time. This ratio is significantly larger in coastal areas (especially in the northeast near Vancouver Island) than in pelagic areas, see Figure 2.7(a), suggesting that shallow water could be the primary source area of short-duration high-amplitude signals. If this is the case, a lower west-to-east peak ratio in conventional cross-correlation functions than in one-bit cross-correlation functions is expected, since the eastern-generated short-duration strong signals would be underestimated by one-bit preprocessing. This is validated by Figure 2.5(g) and (h). The comparison on the entire array will be given in the next section.

2.6 Comparison on the entire array

To show the advantage of using RSNR, we calculated both SNR and RSNR of the cross-correlation functions from conventional, one-bit and RAM preprocessing for the entire CI OBS array record, see Figure 2.8. Station J06A, G30A, and G03A are excluded for they are far from the main part of the array. SNR decreases with station-separation roughly as $1/\sqrt{d}$, while RSNR is less related to station separation, suggesting that geometric spreading effect is minimized in RSNR. Thus, the dominant source direction will be better determined using RSNR.

The two SNRs (one for each side, or equivalently, source direction), as well as the two RSNRs, of each cross-correlation function are much closer to each other with conventional preprocessing than with one-bit and RAM preprocessing, as shown in Figure 2.8. This reflects the bias effect of one-bit and RAM preprocessing as demonstrated in section 2.5.

To investigate the effect of preprocessing on identifying source direction, we first calculate RSNR for each station-pair in CI OBS array with conventional, one-bit and RAM preprocessing methods in 0.115–0.145 Hz band (first column in Figure 2.9). The directions with highest RSNR values should be the dominant directions. Averages of RSNR values for 10° azimuth slices are presented for clarity. Only the outgoing wave (propagating to the other station) RSNRs are plotted, similar to [Tian and Ritzwoller 2015]. Note that here the arrows point to the source, while pointing away from the source in [Tian and Ritzwoller 2015]. Shallow-water station records have a higher background noise level than deep-water stations. Thus, on average, RSNR at shallow-water stations are lower than that at deep-water stations. Therefore, it's more reasonable to compare RSNR in different directions at one station than to compare RSNR between stations, especially between deep-water and shallow-water stations. Stations with RSNR values showing both pelagic and coastal directions (mostly inside the red frame in Figure 2.9) are more informative. Conventional cross-correlation shows no notably dominant source direction while one-bit and RAM cross-correlations show a significantly dominant signal from the west,

especially from the southwest. This is consistent with the source characteristic analysis that short-duration strong signals are mainly coastal-generated (sensitive to conventional preprocessing) while pelagic-generated signals are mostly weak but with long duration (sensitive to one-bit and RAM preprocessing) in the 0.115–0.145 Hz band. Thus the one-bit and RAM preprocessing artificially increase SNR only for long-duration relatively low-amplitude signals. This gives an erroneous source direction distribution.

For comparison, we also calculated the energy ratio of the strongest 5% segments in the 0.2–0.3 Hz band, associated with the deep-water microseism peak [Bromirski, Stephen, and Gerstoft 2013] (see second column in Figure 2.7). The energy ratio is significantly smaller than that in the 0.115–0.145-Hz band, and has less variability with location. But the energy ratio is generally larger in pelagic areas (especially the southwest), which is opposite to the 0.115–0.145 Hz band (compare Figure 2.7(a) and (b)). The RSNR map for 0.2–0.3 Hz indicates a dominant signal from west for all preprocessing methods (second column in Figure 2.9), suggesting pelagic-generated signals are both longer and stronger (in total energy sense) than coastal-generated signals in the 0.2–0.3 Hz band.

We chose the 0.115–0.145-Hz frequency band for several reasons: (1) The spectrum of J30A and J31A show that March 4–5 DF signal is stronger than March 6–7 DF signal only in this frequency band (Figure 2.4), suggesting different source characteristics between 0.115–0.145-Hz microseism and higher-frequency (e.g. 0.2–0.3 Hz) DF microseism levels. (2) As was shown in this section, the conventional cross-correlation function is most different from both one-bit and RAM cross-correlation functions in this frequency band, i.e. the source amplitude and duration effect is strongest in this frequency band. (3) Earthquake signals are easy to detect and remove in the DF band. Comparatively, there is more earthquake surface wave energy in the SF band. The SF band can also be contaminated by currents.

The 0.115–0.145-Hz DF band has some association with SF microseism band variability, with both dominated by excitation near the coast during a strong swell event. However, the

possibility of SF band signals significantly affecting spectral levels in the DF band is minimal since the double-frequency criterion makes for good separation between SF and DF signals. Multiple sources with differing spectral characteristics at different locations could in some cases obscure source directions, but in general the DF signal levels are much stronger than primary microseism levels and so will dominate. Because bottom interaction decreases with increasing frequency (shorter wavelength), ocean waves at over 0.1 Hz produce progressively less SF energy in the DF band.

2.7 Conclusion

Preprocessing has a significant influence on the amplitudes of cross-correlation function peaks. One-bit and RAM preprocessing methods introduce a bias in dominant source direction estimation associated with signal duration. Because they do not conserve amplitude information, signals with long duration dominate the cross-correlation functions, even if their total energy is lower than strong signals with short duration from the opposite direction. Comparatively, because conventional preprocessing retains amplitude information, this method is more influenced by energy and less by duration, which makes it a better choice for dominant source direction determination.

The temporal variation of spectral characteristics across the deep-water CI array stations indicates that there are always DF microseisms in the deep ocean. In contrast, strong DF microseisms are generated near-shore when waves from a storm reach the shore, which occur intermittently on synoptic time scales. Therefore, ubiquitous pelagic-generated signals have a much longer duration time than relatively short-duration coastal-generated signals even though their total energy is similar. Cross-correlation functions from one-bit and RAM preprocessing show a significantly dominant pelagic source direction, while those from conventional preprocessing show no significantly dominant source direction. This is consistent with the source location

characteristics.

Remark

Chapter 2, in full, is a reprint of the material as it appears in Geophysical Journal International: Chen, Z., Gerstoft, P., Bromirski, P.D., 2016, “Microseism source direction from noise cross-correlation”, *Geophysical Journal International*, 205(2), pp.810-818. The dissertation author is the primary investigator and author of this paper.

Figures

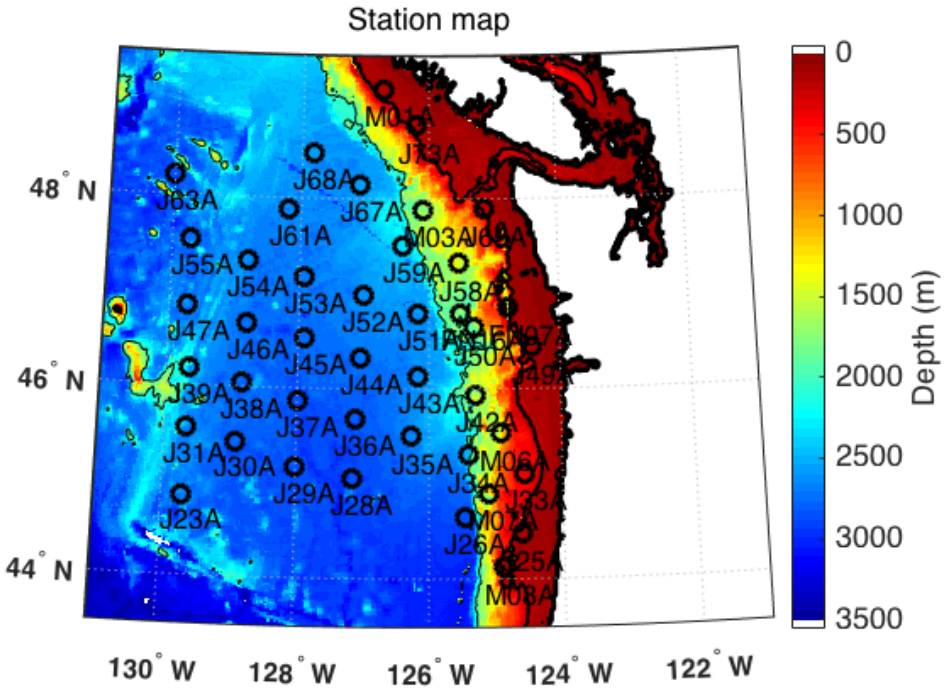

Figure 2.1: CI OBS stations map (March 2012). Color represents seafloor depth. The three black contours are the coastline, the 200-m depth contour, and the 2000-m depth contour, from the thickest to the thinnest lines, respectively. Station J06A, G30A, and G03A are out of the plot region and are not shown in the map.

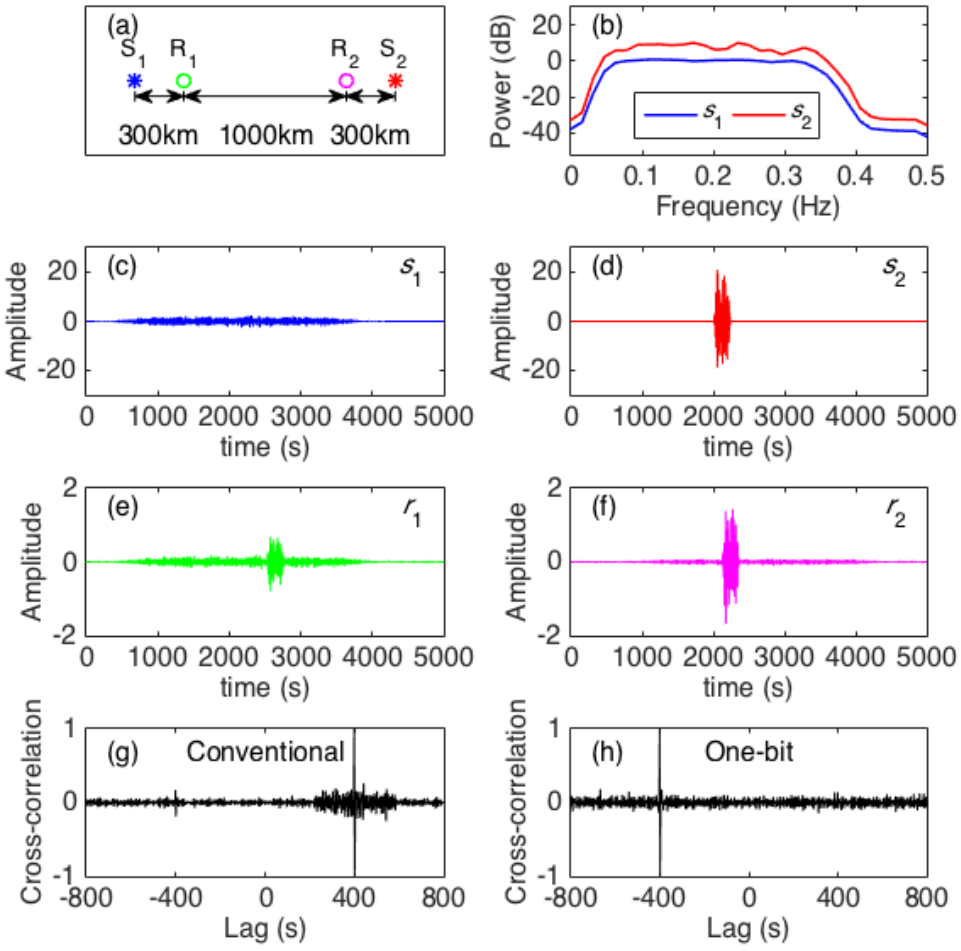

Figure 2.2: Synthetic tests of noise cross-correlation functions: (a) geometry, (b) source spectra, (c) source S_1 time function, (d) source S_2 time function, (e) receiver R_1 record, (f) receiver R_2 record, (g) normalized conventional cross-correlation function, and (h) normalized one-bit cross-correlation function. The records (e and f) were calculated using the Green's function given in Eq. 2.8.

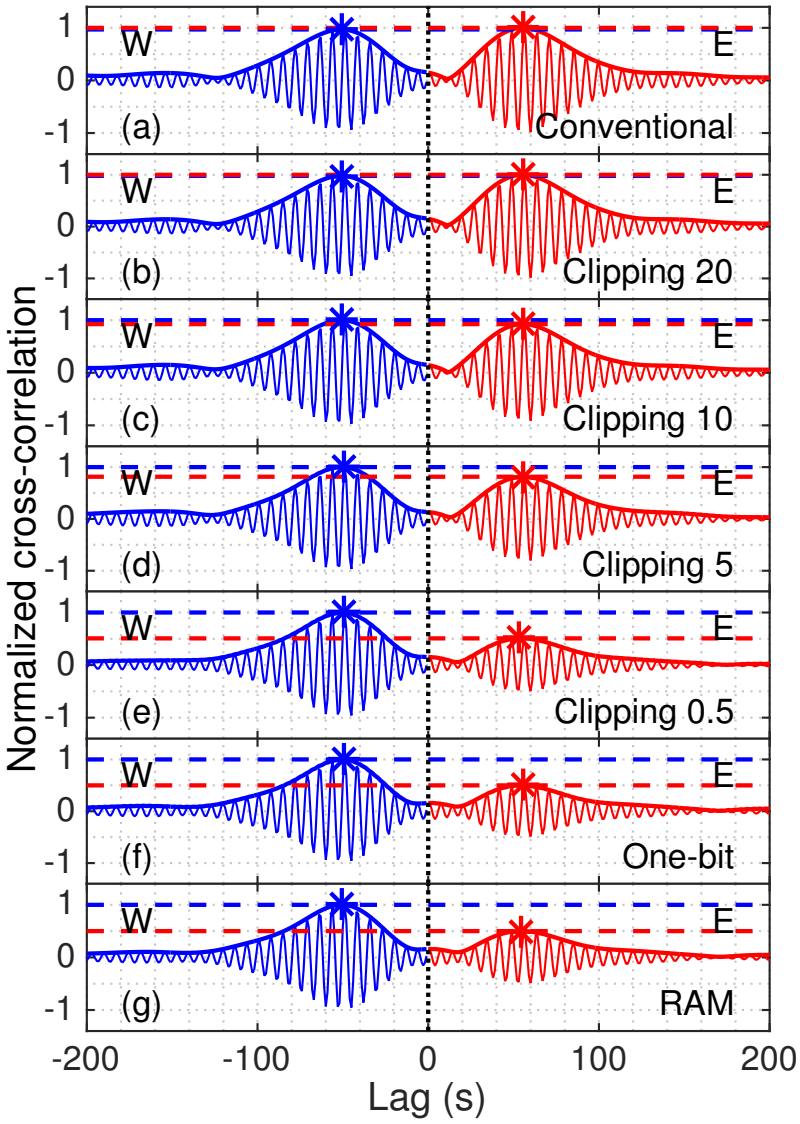

Figure 2.3: Comparison of cross-correlation functions (thin lines) and their envelopes (thick lines) between station-pair J30A and J31A for March 2012 in 0.115–0.145 Hz frequency band. Results are shown for preprocessing methods (a) conventional, (b) clipping (threshold: $20 \times \mathrm{RMS}_{\mathrm{noise}}$), (c) clipping (threshold: $10 \times \mathrm{RMS}_{\mathrm{noise}}$), (d) clipping (threshold: $5 \times \mathrm{RMS}_{\mathrm{noise}}$), (e) clipping (threshold: $0.5 \times \mathrm{RMS}_{\mathrm{noise}}$), (f) one-bit, (g) running-absolute-mean (RAM). Signals coming from west (W, blue) and east(E, red) are indicated. Respective peaks and peak levels are represented by correspondingly colored asterisks and colored dashed lines.

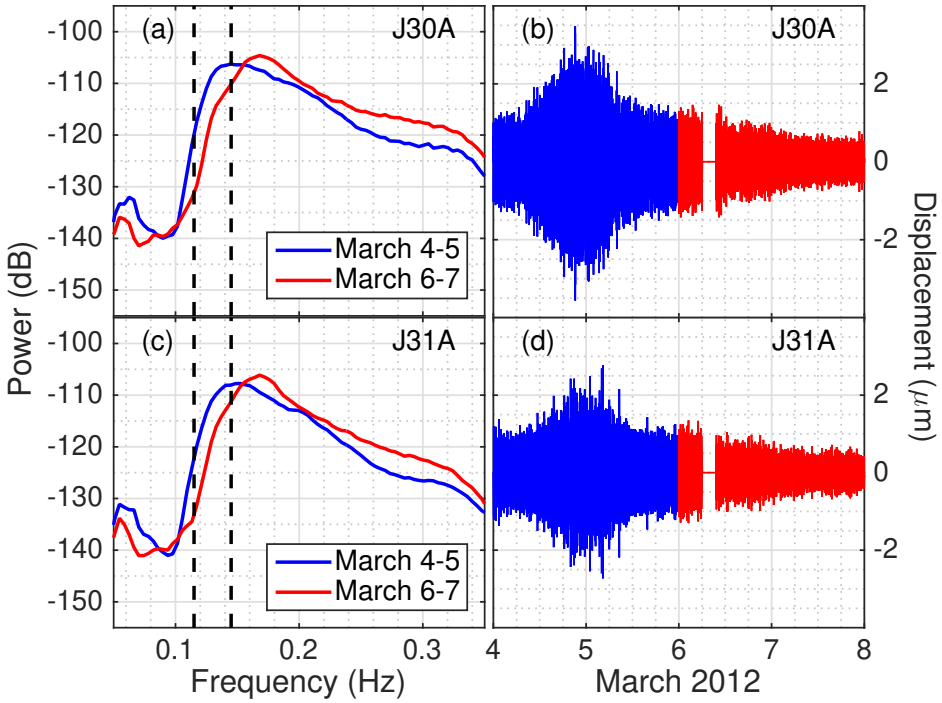

Figure 2.4: Spectra (left column) and 0.115-0.145-Hz-Butterworth-filtered waveforms (right column) of station J30A (top row) and J31A (bottom row) records in March 4–5 (blue) and March 6–7 (red). Spectra were calculated using Welch's method with 50% overlapping 256-s data segments. The corner frequencies of the filter are indicated by the dashed lines. The small local earthquake on March 6 was removed, indicated by the gap.

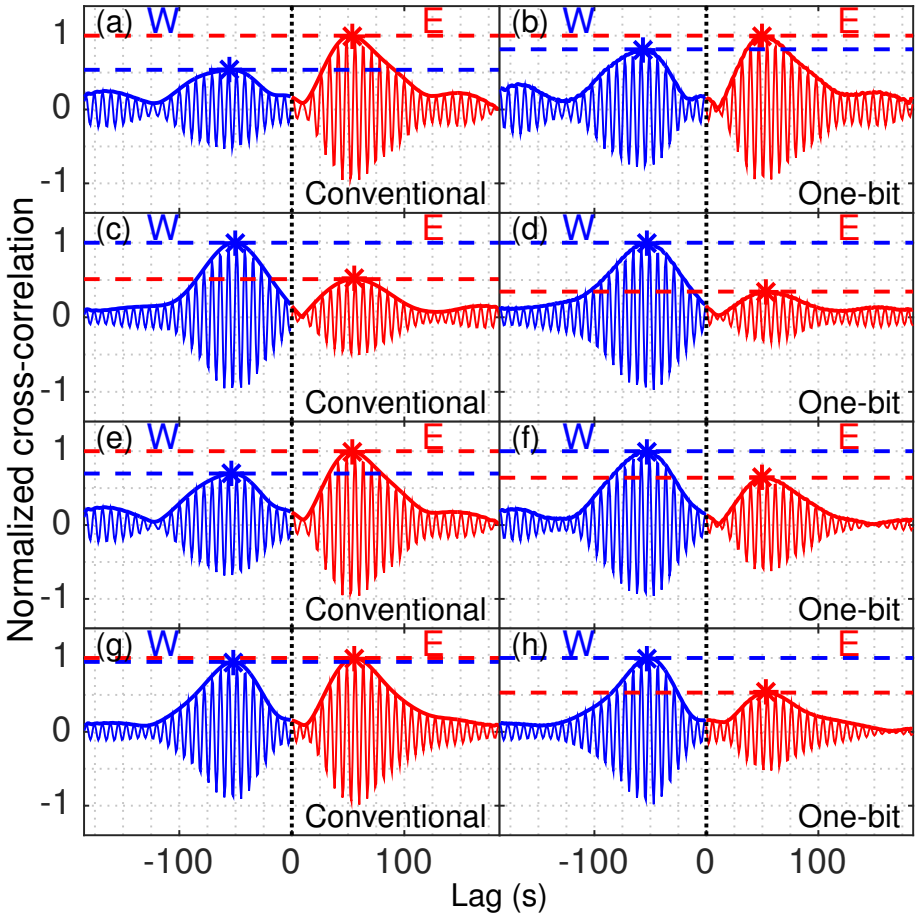

Figure 2.5: Conventional (left column) and one-bit (right column) cross-correlation functions (thin solid lines) and their envelopes (thick solid lines) for station J30A and J31A with each row from top to bottom representing an observation time: (a, b) 4–5 March, (c, d) 6–7 March, (e, f) 4–7 March, and (g, h) 1–31 March. Signals coming from west (W, blue) and east (E, red), as well as the peaks (asterisks) and peak levels (dashed) are indicated.

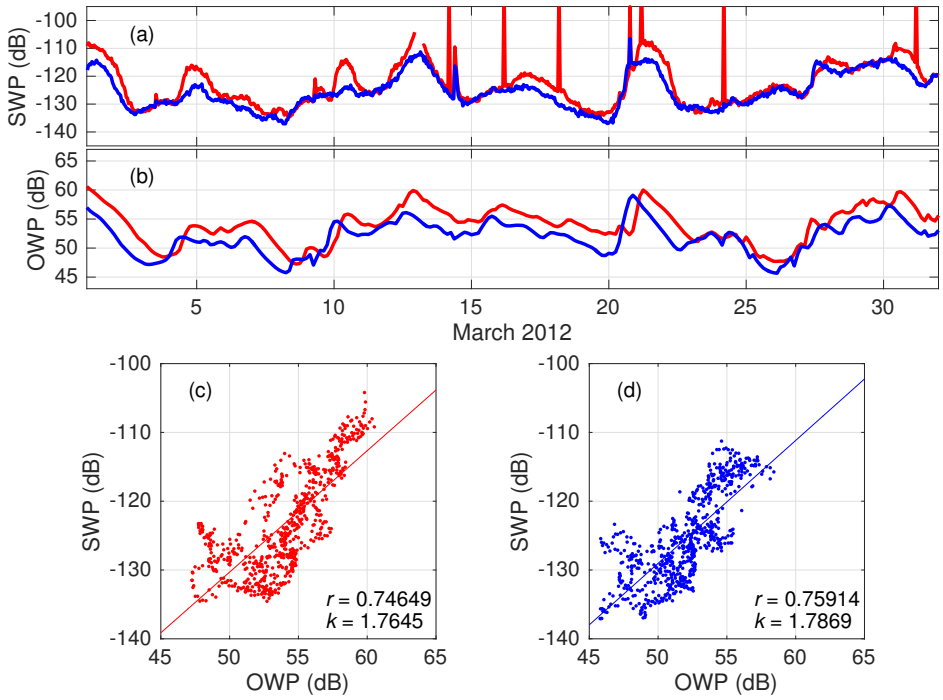

Figure 2.6: (a) Seismic wave power (SWP) of deep-water J31A (blue) and shallow-water J25A (red) records in 0.115–0.145 Hz frequency band and (b) Spatial-linear-interpolated Ocean wave power (OWP) at J31A (blue) and J25A (red) in March 2012. SWP is characterized by hourly mean square of 0.115–0.145-Hz filtered seismogram, while OWP is calculated from equation 2.9. Linear regressions of corresponding SWP and OWP (both in dB) for station (c) J25A and (d) J31A are shown. SWP segments with earthquakes or other local transients are removed. OWP is temporal-interpolated to correspond to SWP segments.

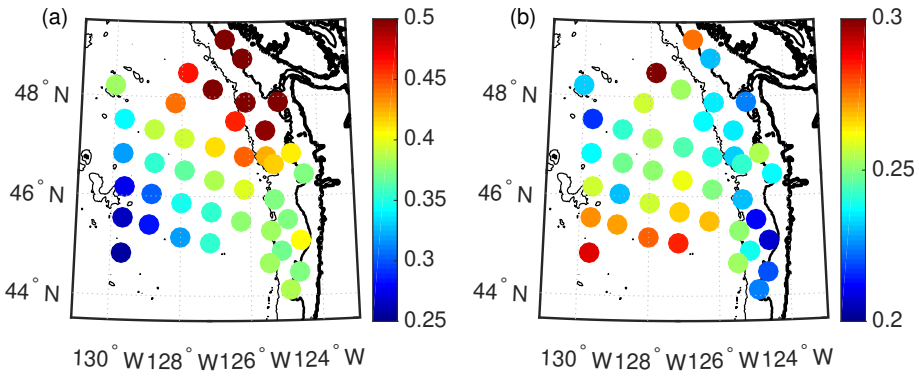

Figure 2.7: The energy ratio of the 5% strongest spectral estimates to the total energy of March 2012. Frequency bands: (a) 0.115–0.145 Hz, (b) 0.2–0.3 Hz. The energy of each segment is represented by the mean of the squared record. The three black contours are coastlines, and the 200-m and 2000-m depth contours, thickest to the thinnest, respectively.

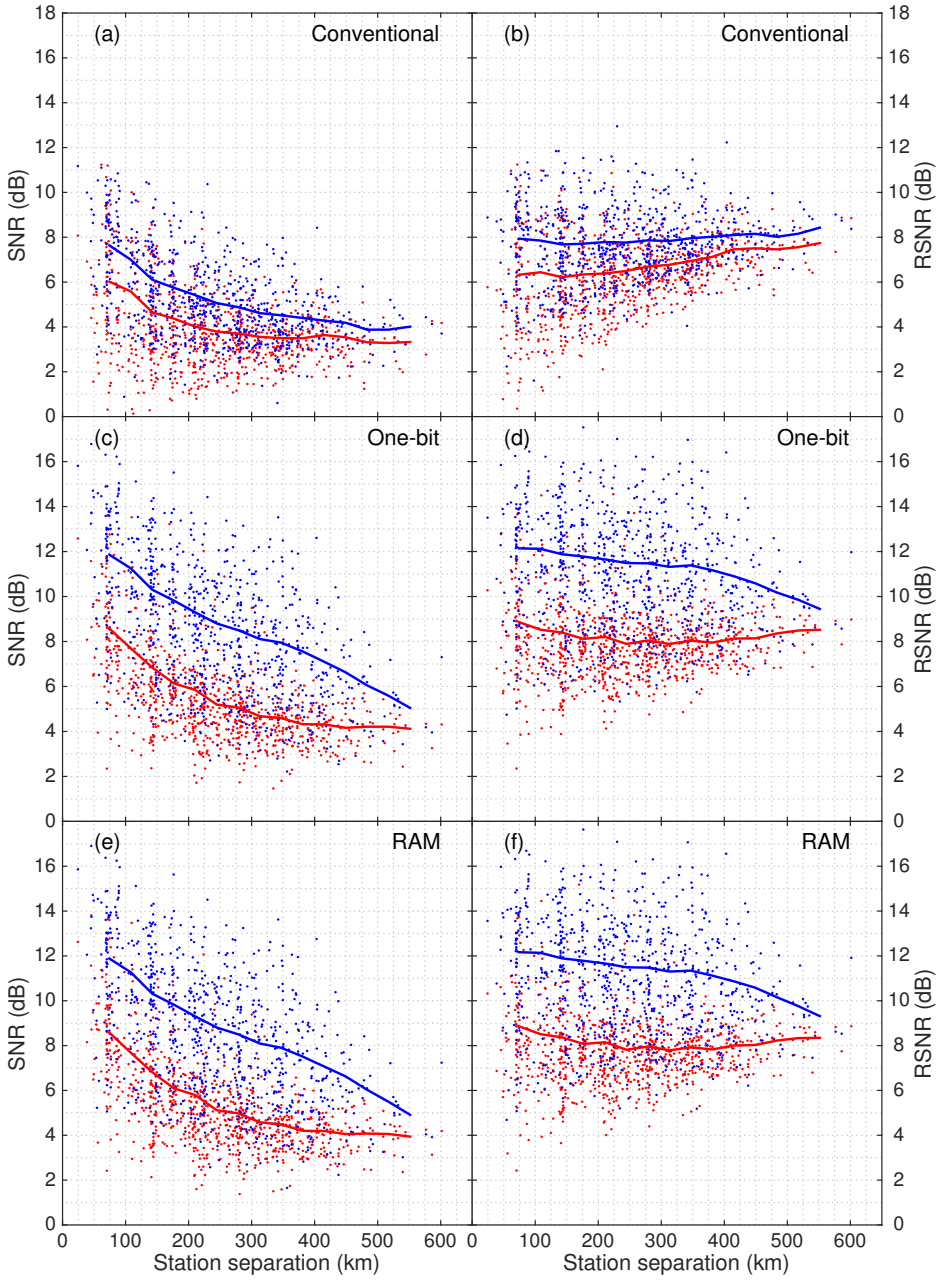

Figure 2.8: Station separation versus SNR (first column) or RSNR (second column) of the cross-correlation functions from conventional (first row), one-bit (second row), and RAM (third row) preprocessing of the CI OBS array records. SNR/RSNR for positive (signals from east, red dots) and negative (signals from west, blue dots) lags are indicated. Colored solid lines are 100-km-window running average of the SNR/RSNR on the corresponding lag side. Frequency band: 0.115–0.145 Hz.

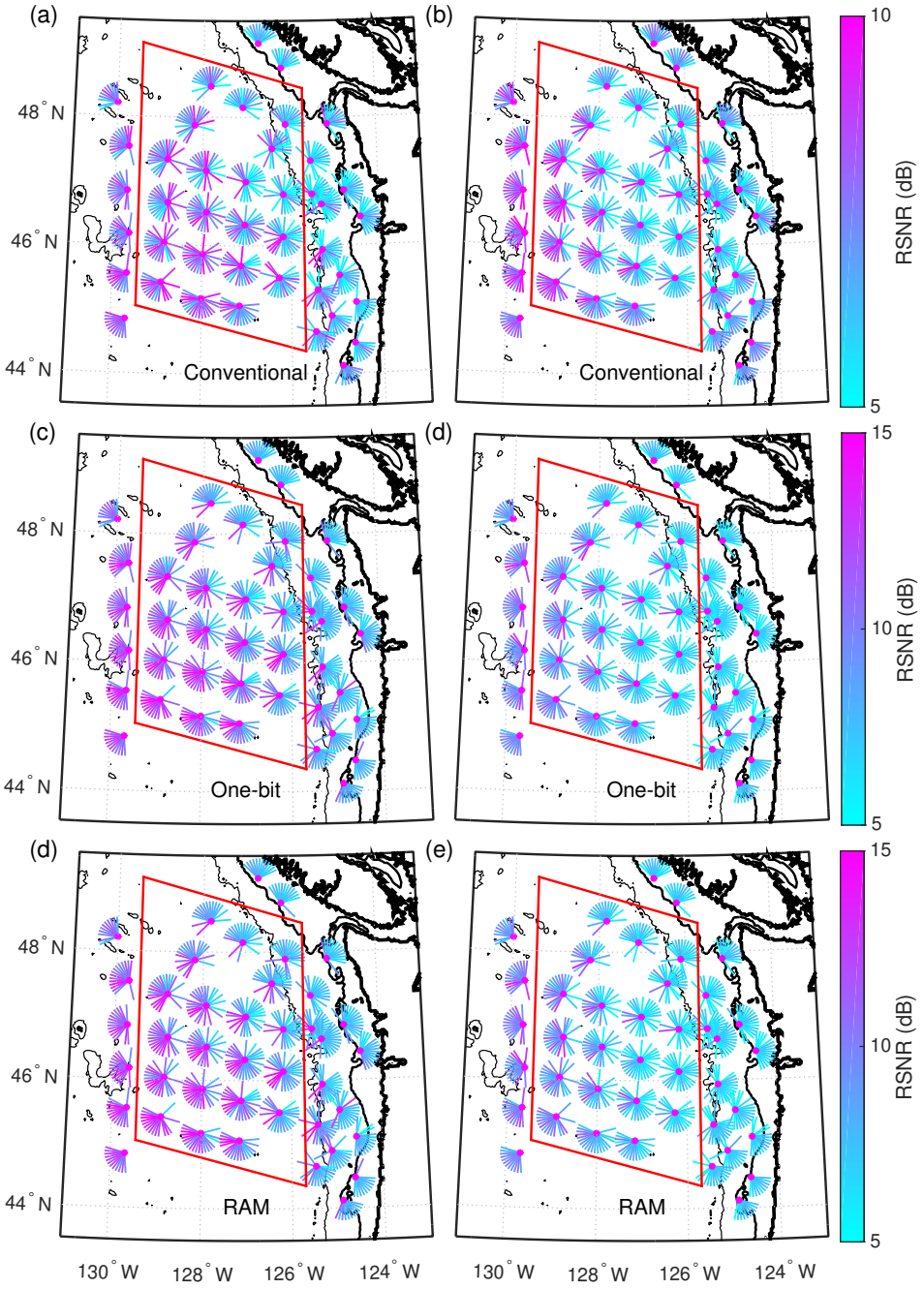

Figure 2.9: Averaged 10° azimuth slices for RSNR of cross-correlation functions from conventional (first row), one-bit (second row), and RAM (third row) preprocessing for entire CI OBS array records in March 2012. Frequency band: 0.115–0.145 Hz (first column) and 0.2–0.3 Hz (second column). Cross-correlation functions shown are restricted to those with RSNR larger than 3 dB on both sides. 821, 833, 860, 856, 860, and 856 out of 861 station-pairs are chosen in (a) to (e), respectively. The contours are the same as in Figure 2.7. The most important stations are enclosed by the red frame. Note that the first row have different color scales.

References

Aki, K. and Richards, P. G. (2002). *Quantitative Seismology*. Second Edition. University Science Books. ISBN: 0935702962.

Ardhuin, F., Stutzmann, E., Schimmel, M., and Mangeney, A. (2011). "Ocean wave sources of seismic noise". In: *Journal of Geophysical Research: Oceans* 116.C9. DOI: 10.1029/2011JC006952.

Bensen, G. D., Ritzwoller, M. H., Barmin, M. P., Levshin, A. L., Lin, F., Moschetti, M. P., Shapiro, N. M., and Yang, Y. (2007). "Processing seismic ambient noise data to obtain reliable broad-band surface wave dispersion measurements". In: *Geophysical Journal International* 169.3, pp. 1239–1260. DOI: 10.1111/j.1365-246X.2007.03374.x.

Bromirski, P. D. and Duennebier, F. K. (2002). "The near-coastal microseism spectrum: Spatial and temporal wave climate relationships". In: *Journal of Geophysical Research: Solid Earth* 107.B8, ESE 5-1–ESE 5-20. DOI: 10.1029/2001JB000265.

Bromirski, P. D., Duennebier, F. K., and Stephen, R. A. (2005). "Mid-ocean microseisms". In: *Geochemistry, Geophysics, Geosystems* 6.4. DOI: 10.1029/2004GC000768.

Bromirski, P. D., Flick, R. E., and Graham, N. (1999). "Ocean wave height determined from inland seismometer data: Implications for investigating wave climate changes in the NE Pacific". In: *Journal of Geophysical Research: Oceans* 104.C9, pp. 20753–20766. DOI: 10.1029/1999JC900156.

Bromirski, P. D., Stephen, R. A., and Gerstoft, P. (2013). "Are deep-ocean-generated surface-wave microseisms observed on land?" In: *Journal of Geophysical Research: Solid Earth* 118.7, pp. 3610–3629. DOI: 10.1002/jgrb.50268.

Campillo, M. and Paul, A. (2003). "Long-Range Correlations in the Diffuse Seismic Coda". In: *Science* 299.5606, pp. 547–549. DOI: 10.1126/science.1078551.

Cessaro, R. K. (1994). "Sources of primary and secondary microseisms". In: *Bulletin of the Seismological Society of America* 84.1, pp. 142–148.

Cupillard, P. and Capdeville, Y. (2010). "On the amplitude of surface waves obtained by noise correlation and the capability to recover the attenuation: a numerical approach". In: *Geophysical Journal International* 181.3, pp. 1687–1700. DOI: 10.1111/j.1365-246X.2010.04586.x.

Gerstoft, P. and Tanimoto, T. (2007). "A year of microseisms in southern California". In: *Geophysical Research Letters* 34.20. DOI: 10.1029/2007GL031091.

Harmon, N., Rychert, C., and Gerstoft, P. (2010). "Distribution of noise sources for seismic interferometry". In: *Geophysical Journal International* 183.3, pp. 1470–1484. DOI: 10.1111/j.1365-246X.2010.04802.x.

Hasselmann, K. (1963). "A statistical analysis of the generation of microseisms". In: *Reviews of Geophysics* 1.2, pp. 177–210. DOI: 10.1029/RG001i002p00177.

Kedar, S., Longuet-Higgins, M., Webb, F., Graham, N., Clayton, R., and Jones, C. (2008). "The origin of deep ocean microseisms in the North Atlantic Ocean". In: *Proceedings of the Royal Society A: Mathematical, Physical and Engineering Science* 464.2091, pp. 777–793. DOI: 10.1098/rspa.2007.0277.

Kinsman, B. (1965). *Wind Waves: Their Generation and Propagation on the Ocean Surface*. Prentice-Hall.

Lin, F.-C., Tsai, V. C., and Ritzwoller, M. H. (2012). "The local amplification of surface waves: A new observable to constrain elastic velocities, density, and anelastic attenuation". In: *Journal of Geophysical Research: Solid Earth* 117.B6. DOI: 10.1029/2012JB009208.

Longuet-Higgins, M. S. (1950). "A theory of the origin of microseisms". In: *Philosophical Transactions of the Royal Society of London. Series A, Mathematical and Physical Sciences* 243.857, pp. 1–35. DOI: 10.1098/rsta.1950.0012.

Prieto, G. A., Lawrence, J. F., and Beroza, G. C. (2009). "Anelastic Earth structure from the coherency of the ambient seismic field". In: *Journal of Geophysical Research: Solid Earth* 114.B7. DOI: 10.1029/2008JB006067.

Romanowicz, B. (1991). "Seismic Tomography of the Earth's Mantle". In: *Annual Review of Earth and Planetary Sciences* 19.1, pp. 77–99. DOI: 10.1146/annurev.ea.19.050191.000453.

— (2003). "GLOBAL MANTLE TOMOGRAPHY: Progress Status in the Past 10 Years". In: *Annual Review of Earth and Planetary Sciences* 31.1, pp. 303–328. DOI: 10.1146/annurev.earth.31.091602.113555.

Sato, H. and Fehler, M. C. (2009). *Seismic Wave Propagation and Scattering in the Heterogeneous Earth*. Springer. ISBN: 9783540896234.

Shapiro, N. M., Campillo, M., Stehly, L., and Ritzwoller, M. H. (2005). "High-Resolution Surface-Wave Tomography from Ambient Seismic Noise". In: *Science* 307.5715, pp. 1615–1618. DOI: 10.1126/science.1108339.

Snieder, R. (2004). "Extracting the Green's function from the correlation of coda waves: A derivation based on stationary phase". In: *Physical Review E* 69 (4), p. 046610. DOI: 10.1103/PhysRevE.69.046610.

Stehly, L., Campillo, M., Froment, B., and Weaver, R. L. (2008). "Reconstructing Green's function by correlation of the coda of the correlation (C3) of ambient seismic noise". In: *Journal of Geophysical Research: Solid Earth* 113.B11. DOI: 10.1029/2008JB005693.

Tian, Y. and Ritzwoller, M. H. (2015). "Directionality of ambient noise on the Juan de Fuca plate: implications for source locations of the primary and secondary microseisms". In: *Geophysical Journal International* 201.1, pp. 429–443. DOI: 10.1093/gji/ggv024.

Tolman, H. L. (2009). "User manual and system documentation of WAVEWATCH III TM version 3.14". In: *Technical Note, MMAB Contribution* 276.

Toomey, D. R., Allen, R. M., Barclay, A. H., Bell, S. W., Bromirski, P. D., Carlson, R. L., Chen, X., Collins, J. A., Dziak, R. P., Evers, B., Forsyth, D. W., Gerstoft, P., Hooft, E. E., Livelybrooks, D., Lodewyk, J. A., Luther, D. S., Mcguire, J. J., Schwartz, S. Y., Tolstoy, M., Tréhu, A. M., Weirathmueller, M., and Wilcock, W. S. (2014). "THE CASCADIA INITIATIVE: A Sea Change In Seismological Studies of Subduction Zones". In: *Oceanography* 27.2, pp. 138–150.

Traer, J. and Gerstoft, P. (2014). "A unified theory of microseisms and hum". In: *Journal of Geophysical Research: Solid Earth* 119.4, pp. 3317–3339. DOI: 10.1002/2013JB010504.

Tsai, V. C. (2011). "Understanding the amplitudes of noise correlation measurements". In: *Journal of Geophysical Research: Solid Earth* 116.B9. DOI: 10.1029/2011JB008483.

Welch, P. D. (1967). "The use of fast Fourier transform for the estimation of power spectra: A method based on time averaging over short, modified periodograms". In: *IEEE Transactions on Audio and Electroacoustics* 15.2, pp. 70–73. DOI: 10.1109/TAU.1967.1161901.

Yang, Y. and Ritzwoller, M. H. (2008). "Characteristics of ambient seismic noise as a source for surface wave tomography". In: *Geochemistry, Geophysics, Geosystems* 9.2. DOI: 10.1029/2007GC001814.

Yao, H. and Van Der Hilst, R. D. (2009). "Analysis of ambient noise energy distribution and phase velocity bias in ambient noise tomography, with application to SE Tibet". In: *Geophysical Journal International* 179.2, pp. 1113–1132. DOI: 10.1111/j.1365-246X.2009.04329.x.

Chapter 3

Ocean-Excited Plate Waves in the Ross and Pine Island Glacier Ice Shelves

Ice shelves play an important role in buttressing land ice from reaching the sea, thus restraining the rate of grounded ice loss. Long-period gravity-wave impacts excite vibrations in ice shelves that can expand pre-existing fractures and trigger iceberg calving. To investigate the spatial amplitude variability and propagation characteristics of these vibrations, a 34-station broadband seismic array was deployed on the Ross Ice Shelf (RIS) from November 2014 to November 2016. Two types of ice-shelf plate waves were identified with beamforming: flexural-gravity waves and extensional Lamb waves. Below 20 mHz, flexural-gravity waves dominate coherent signals across the array and propagate landward from the ice front at close to shallow-water gravity-wave speeds ($\sim$70 $\mathrm{m\,s^{-1}}$). In the 20–100 mHz band, extensional Lamb waves dominate, and propagate at phase speeds near 3 $\mathrm{km\,s^{-1}}$. Flexural-gravity and extensional Lamb waves were also observed by a 5-station broadband seismic array deployed on the Pine Island Glacier (PIG) ice shelf from January 2012 to December 2013, with flexural wave energy also detected at the PIG in the 20–100 mHz band. Considering the ubiquitous presence of storm activity in the Southern Ocean and the similar observations at both the RIS and the PIG ice shelves,

it is likely that most, if not all, West Antarctic ice shelves are subjected to similar gravity-wave excitation.

3.1 Introduction

Ice shelves play an important role in inhibiting sea level rise as they buttress glaciers on land and restrain ice discharge to the circum-Antarctica seas that merge with the Southern Ocean [MacAyeal 1987; Rignot et al. 2004; Scambos et al. 2004]. Volume loss of Antarctic ice shelves [Paolo, Fricker, and Padman 2015] reduces buttressing, which raises concerns of consequent acceleration of glacier discharge, raising sea level. Ice shelf volume loss results from ice shelf thinning due to enhanced ocean-driven melting and iceberg calving [Pritchard et al. 2012; Paolo, Fricker, and Padman 2015]. Numerical modeling [Sergienko 2010; Lipovsky 2018] and observations [MacAyeal et al. 2006; Brunt, Okal, and MacAyeal 2011] indicate that ocean gravity wave impacts can expand existing crevasses and fractures, leading to calving events and/or contributing to a reduction of ice shelf integrity. Seasonal loss of sea ice leaves the outer ice shelf margin directly impacted by swell, which may have contributed to the collapse of the Larsen A and B and Wilkins ice shelves [Massom et al. 2018]. However, modeling suggests that swell alone may not provide sufficient forcing to induce ice-shelf disruption [Lipovsky 2018].

Considering the persistent strong Southern Ocean storm activity and the associated intense ocean wave climate that continuously impacts ice shelves [Trenberth 1991; Tolman 2009; Chapman et al. 2015], ocean wave impacts likely play a role in ice shelf evolution. Thus, it is important to quantify the spatial and temporal response of ice shelves to ocean gravity waves with in-situ measurements. This will improve modeling of ice-shelf/ice-sheet response to climate change, and consequently reduce the uncertainty in ice-sheet mass loss projections over the coming decades.

To better understand the response of ice shelves to ocean-gravity-wave impacts, we

deployed a broadband seismic array on the Ross Ice Shelf (RIS) from October 2014 to November 2016 [Bromirski et al. 2015; Diez et al. 2016]. The seismic network consisted of two linear transects in a cross-like configuration that were approximately parallel and orthogonal to the shelf front (Fig. 3.1a), and included a dense subarray at the intersection of the two transects. Station separations within the transects were typically 80–90 km, while separations in the center subarray were about 5–10 km. The large array aperture and multi-year deployment allowed the spatial, seasonal, and interannual variations of the ice shelf response to ocean forcing to be quantified, and provided baseline observations to identify the magnitude of change in future studies.

In addition to the RIS array, data from a 5-station broadband seismic array deployed on the Pine Island Glacier (PIG) ice shelf from January 2012 to December 2013 [Christianson et al. 2016] were used for comparative analyses. This seismic array was about 20 km from the PIG front, with station separation about 2 km. These data allow comparison of the response of a large "stable" ice shelf (the RIS) to the much smaller less "stable" PIG ice shelf. There are significant differences in size, ice flow speed, and thinning rate of RIS and PIG. Seismic comparisons between the two shelves will show whether they have a different response to gravity-wave forcing, which can be used to estimate and compare their properties. The smaller station separation of the PIG array presented the possibility of detecting higher-frequency shorter wavelength signals than the RIS array. However, the few stations and small aperture of the PIG array preclude a detailed comparison with the RIS array results.

In this paper, we first introduce the geometry of the RIS and the PIG ice shelf. Then we introduce plate wave theory and discuss the generation mechanism. A swell event impacting the RIS during austral summer when sea ice was absent is then analyzed from both observational and theoretical perspectives. Beamforming and cross-correlation techniques are employed to obtain the signal propagation direction and the dispersion relation, which indicate the wave types and ice shelf elastic properties. Principal component analysis quantifies particle motion characteristics, which assist in the identification of the wave types. Finally, plate waves observed on the PIG ice

shelf are discussed and compared with RIS observations.

3.2 Study Regions

3.2.1 RIS

RIS ice thicknesses are 240–340 m at the ice front, and increase up to 700–800 m near the grounding zone [Fretwell et al. 2013]. The geometry of a cross-section roughly along the north-south array transect shows the variation of the ice thickness and the bathymetry (Fig. 3.1b). Along the cross-section, the ice thickness is ∼240 m at the ice front and gradually increases to ∼330 m under DR10 (the center of the dense subarray, ∼130 km from ice-front station DR02). Under RS18 (the southern most station, ∼380 km from the ice front), the ice thickness is ∼370 m. The seafloor depth varies between 600 and 800 m near the ice front, with the sub-shelf water thickness decreasing from ∼500 m near the ice front to ∼480 m below DR10 and ∼160 m below RS18, which sits above a basement high.

3.2.2 PIG Ice Shelf

The PIG ice shelf [∼3000 km^2, Bindschadler, Vaughan, and Vornberger 2011] is much smaller than the RIS [472 960 km^2, Scambos et al. 2007]. However, it is the largest regional contributor to sea level rise [Medley et al. 2014]. The ice flow speed near the ice shelf front increased from ∼2.3 $km\,a^{-1}$ to ∼4.0 $km\,a^{-1}$ from 1974 to 2008 [Joughin et al. 2003; Joughin, Smith, and D. M. Holland 2010], while the ice flow speed at the RIS is generally less than 1.2 $km\,a^{-1}$. The increased flow rate at the PIG ice shelf suggests that it is less stable than RIS. In contrast to RIS, rapid melting occurs beneath the PIG ice shelf due to the warm Circumpolar Deep Water (CDW) intruding the Amundsen Sea coast [Jacobs, Hellmer, and Jenkins 1996; Thoma et al. 2008; Joughin, Smith, and D. M. Holland 2010; Bindschadler, Vaughan, and Vornberger

2011], with enhanced thinning potentially weakening PIG.

The PIG ice shelf is over 1 km thick at its grounding line and thins to about 300 m at the ice front [Bindschadler, Vaughan, and Vornberger 2011]. The average thicknesses of the PIG seismic array sector ($\sim$460 m) and the RIS beamformed subarray sector ($\sim$300 m) are comparable. The water layer thickness at the PIG ice front is $\sim$500 m and decreases to $\sim$200 m over a distance of 35–40 km away from the ice front [Bindschadler, Vaughan, and Vornberger 2011]. There are no bathymetry data more than 40 km inland from the shelf front.

3.3 Plate Wave Theory

Ice shelves can be viewed as floating plates of ice formed by glacier outflows. Ocean surface gravity waves impact ice shelves, couple wave energy with the ice, and excite seismic plate waves. Propagation characteristics of gravity-wave-excited plate waves provide information on the elastic properties of the ice, which can be related to ice shelf integrity, i.e. weaker, more fractured ice (PIG) will behave differently than more competent (RIS) ice.

There are three types of ocean surface gravity waves below 100 mHz that excite plate waves in ice shelves: (1) very-long-period (VLP) gravity waves ($<$ 3 mHz): tsunami and meteorologically-forced waves, (2) infragravity (IG) waves (3–20 mHz), generated by nonlinear wave interactions along coastlines [Herbers, Elgar, and Guza 1995; Bromirski, Sergienko, and MacAyeal 2010] and under mid-ocean storms [Uchiyama and McWilliams 2008], and (3) swell (30–100 mHz), generated by cyclonic storm systems where wind energy couples into ocean swell. At lower frequencies ($<$ 20 mHz for the RIS), gravity provides a restoring force that is significant in ocean/ice-shelf coupling, generating flexural-gravity waves [Fox and Squire 1990]. At higher frequencies ($>$ 20 mHz for the RIS), where the gravity restoring force is negligible, Lamb waves, with both symmetric (extensional) and anti-symmetric (flexural) modes, are excited [Lamb 1917].

3.3.1 Lamb Waves

Dispersion relation

Lamb waves have multiple modes, described by the dispersion relations first developed by [Rayleigh 1888] and [Lamb 1889], with a more systematic analysis by [Lamb 1917]. To implement the system of equations, we construct a 3-dimensional *x*-*y*-*z* coordinate system, with the horizontal *x*-*y* plane coinciding with an infinite-extent ice plate of $2h$-thickness. This coordinate system assumes that plane waves propagate in the x direction with plane strain in the y direction. Let k_P, k_S, and k_L be the wavenumbers of the P wave, S wave, and Lamb waves, respectively. For stress-free boundaries, the frequency equations are obtained as modified from [Graff 1991],

$$\frac{\tanh k_2 h}{\tanh k_1 h} = \left[\frac{4 k_1 k_2 k_L^2}{(k_L^2 + k_2^2)^2} \right]^{\pm 1}, \tag{3.1}$$

where k_1 and k_2 are defined as

$$\begin{aligned} k_1^2 &= k_L^2 - k_P^2, \\ k_2^2 &= k_L^2 - k_S^2. \end{aligned} \tag{3.2}$$

The superscript on the right hand side of Eqn (3.1) corresponds to symmetric (extensional) mode $(+1)$ or anti-symmetric (flexural) mode (-1), identified by the particle motion symmetry with respect to the mid-plane of the plate.

The dispersion relation, i.e. Eqn (3.1), is numerically solved. Dispersion curves for both symmetric and anti-symmetric modes (Fig. 3.2a) have multiple higher-frequency sub-modes that depend on the vertical wavelength, represented by S_n and A_n for nth-order symmetric and anti-symmetric mode respectively. These modes approach the Rayleigh wave speed ($\sim 0.92 c_S$, where c_S is S-wave speed) asymptotically at the high-frequency end. Only the very low-frequency end of the curves ($k_S h < 0.12$) applies to the response of the RIS (Fig. 3.2b). Specifically, Lamb waves are observed below 100 mHz with array methods, above which the coherence between

stations drops to an unobservable level due to a combination of higher attenuation, and/or lower source power, and/or seismic station spacing. In addition, the ice shelf thickness $2h$ is less than 620 m over the seismic array (except land stations) (Fig. 3.1b). Assuming the S-wave speed of glacial ice $c_S = 1.58\ \mathrm{km\,s^{-1}}$ (Table 3.1), at frequencies $f < 100$ mHz, we have

$$k_S h = \frac{2\pi f}{c_S} h < \frac{2\pi \times 100\ \mathrm{mHz}}{1.58\ \mathrm{km\,s^{-1}}} \times \frac{620\ \mathrm{m}}{2} \approx 0.12, \tag{3.3}$$

which indicates that only fundamental symmetric and anti-symmetric modes (S_0 and A_0) are observable on the RIS (Fig. 3.2a). Theoretical free-space Lamb wave dispersion curves (Fig. 3.2b) of a vacuum-ice-vacuum (VIV) model (Fig. 3.3) are given as a rough approximation for the RIS.

Particle motion

For Lamb waves under stress-free boundary conditions, or free-space Lamb waves, the horizontal (U) and vertical (W) particle motions of S_0 and A_0 modes are determined from the modified solutions of [Viktorov 1967, Eqn (II.21) and (II.22)] as

$$\begin{aligned} U_{S_0} &= A k_S \frac{k_{LS_0}^2 - k_2^2}{k_{LS_0}^2 + k_2^2} \frac{1}{k_S h} \sin(k_{LS_0} x - \omega t), \\ W_{S_0} &= A k_S \frac{k_{LS_0}^2 - k_2^2}{k_{LS_0}^2 + k_2^2} \frac{k_1 z}{k_S h} \cos(k_{LS_0} x - \omega t), \end{aligned} \tag{3.4}$$

and

$$\begin{aligned} U_{A_0} &= B k_S \frac{k_S z}{2} \sin(k_{LA_0} x - \omega t), \\ W_{A_0} &= B k_S \frac{k_S}{2 k_{LA_0}} \cos(k_{LA_0} x - \omega t), \end{aligned} \tag{3.5}$$

where k_{LS_0} and k_{LA_0} are the wavenumbers of the fundamental S_0 and A_0 modes of the Lamb waves. The parameters A and B are constants that are determined by the particle motion amplitude, while ω is the angular frequency.

According to Eqn (3.4) and (3.5), for a thin plate ($k_S h \ll 1$), horizontal displacements (extensional motions) are dominant for the S_0 mode, while vertical displacements (flexural motions) are dominant for the A_0 mode. In addition, the particle motions of S_0 and A_0 modes are both retrograde. But these retrograde motions are difficult to observe since the ellipticity is very high, and thus background noise may overwhelm displacements along the minor axis.

For ice shelves, where flexural motions of the ice are coupled to motions of the water layer, the dispersion curves are different from the free-space Lamb wave dispersion curves. The extensional motions of the RIS have small vertical displacements and are minimally affected by the ice-water coupling, thus should be close to the free-space S_0 mode, represented by S_0^*. In contrast, the flexural motions in the RIS might be appreciably different than the free-space A_0 mode, represented by A_0^*. Synthetic modeling is necessary to assess the coupling effects on the flexural motions.

Synthetic modeling

To explore the effects of the components of the air-ice-water (AIW) system representative of seismic wave propagation on the RIS, synthetic seismograms were computed for VIV and AIW models (Fig. 3.3). The modeling was implemented using OASES, a seismo-acoustic package [Schmidt 2004], with ice properties given in Table 3.1. The source function is a Ricker wavelet centered at 50 mHz, representing 20 s period ocean swell impacting the RIS. Since we are dealing with long-wavelength seismic waves ($>$ 3 km), small-scale structure should not have a significant effect on seismic wave propagation in the frequency bands studied. For example, the surface firn layer thickness is on the order of 50 m [Diez et al. 2016], which will have minimal effect in the frequency bands investigated. However, as has been shown by variable ice shelf responses in observations [Bromirski et al. 2017] and modeling [Sergienko 2017], ice shelf and sub-shelf water layer thicknesses can have a significant effect.

For the VIV model, non-dispersive fundamental extensional Lamb waves S_0 traveling at

2.67 $\mathrm{km\,s^{-1}}$ can be identified (Fig. 3.4a), consistent with the theoretical dispersion curve of the S_0 mode (Fig. 3.2b). The wave amplitude decreases with the range due to geometrical spreading. Fundamental flexural Lamb waves A_0 are highly dispersive near the 50 mHz source frequency selected (Fig. 3.4c), with phase speed of 0.27 $\mathrm{km\,s^{-1}}$ that is roughly consistent with the theoretical value for the A_0 mode (Fig. 3.2a).

For the AIW model, The extensional Lamb waves, S_0^*, are observed for the AIW model with the same phase and group speeds and similar attenuation as S_0 for VIV (Fig. 3.4a,b; green dashed lines), showing that the water layer has little effect on extensional motions. The flexural Lamb waves, A_0^*, are observed for AIW, but have lower amplitude than A_0 for VIV due to energy coupled into the water layer (Fig. 3.4c,d). The phase speed of A_0^* cannot be identified due to dispersion and low amplitude.

3.3.2 Flexural-Gravity Waves and Flexural Waves

At lower frequencies (< 20 mHz), the gravity restoring-force effect is non-negligible, making it an inappropriate problem for OASES, as the effect of gravity is not included in OASES. However, an analytical solution for low-frequency flexural motions can be obtained by assuming a rigid bed below the water layer, i.e. the air-ice-water-bed (AIWB) model (Fig. 3.3), and a thin-plate model (plate thickness $\ll$ flexural-gravity-wave wavelength). Equations of the velocity potential field in water are constructed with ice-water boundary conditions on top and no vertical displacement at the bottom, yielding flexural-gravity waves excited at the ice-water interface. There are two traveling modes, four damped traveling modes, and an infinite number of evanescent modes [Fox and Squire 1991]. Traveling modes can be extracted by array coherence analysis. Because of the rapid attenuation of damped and evanescent modes with distance from the ice front, these modes contribute to relatively stronger vibrations only at the ice front. Although evanescent modes do not propagate efficiently, they are important in gravity-wave energy reflection and

transmission. At higher frequencies ($>$ 20 mHz), the gravity restoring-force effect vanishes and the flexural-gravity-wave phase speeds approach flexural Lamb wave (A_0^*) speeds, making them indistinguishable in this band. To differentiate these higher-frequency flexural motions from those where the effect of gravity is important, we term them flexural waves.

3.3.3 Dispersion Comparison

To understand propagation characteristics of plate waves generated by ocean wave impacts at the RIS, we compared theoretical dispersion curves of A_0 for the VIV model, flexural waves, flexural-gravity waves, and ocean surface gravity waves for the AIWB model (Fig. 3.5a) prior to determining the wave types from dispersion curves obtained with array processing of the observations. Note that the bed is assumed rigid for flexural-gravity waves and ocean surface gravity waves to simplify analytical solution, but is non-rigid when modeling flexural waves using crustal properties of the uppermost solid layer in PREM [Dziewonski and Anderson 1981]. For flexural-gravity waves, the ice thickness of the RIS (mostly 200 to 400 m) is much smaller than plate-wave wavelengths ($>$ 3000 m) for frequencies below 100 mHz. Thus the thin-plate assumption is valid.

The dispersion curve of A_0 in VIV calculated by OASES coincides with the analytical solution [Viktorov 1967] above 5 mHz, indicating good numerical stability except at very low frequencies. The A_0^* mode travels much slower in AIWB than A_0 does in VIV in the 10–100 mHz band, but closer to flexural-gravity wave speeds in AIWB, demonstrating the importance of water-layer coupling on plate-wave propagation. Below 10 mHz, the flexural-gravity-wave phase speed approaches the shallow-water gravity-wave phase speed ($\sim$70 m s^{-1}), while the A_0^* phase speed drops below the gravity-wave phase speed. This confirms that the gravity restoring-force effect is more significant at low frequencies. Hence, the flexural-gravity-wave formulation gives a better approximation of the flexural motions below 10 mHz than the A_0^* dispersion.

3.3.4 Wave Forcing Mechanism

Excitation of flexural-gravity waves requires coupling of gravity-wave energy at the base of the ice shelf. Consequently, because pressure perturbations from surface gravity waves decrease exponentially with depth, ice shelf thickness is an important parameter in the coupling mechanism. The ratio between gravity-wave pressure perturbation amplitude at depth z and at surface is given by

$$\alpha = \frac{\cosh[k_G(z+H)]}{\cosh(k_G H)}, \tag{3.6}$$

where H is total water depth [Kundu, Cohen, and Dowling 2011]. The wavenumber k_G at frequency f is determined by the gravity-wave dispersion relation

$$c_G = \frac{2\pi f}{k_G} = \sqrt{\frac{g}{k_G}\tanh(k_G H)}, \tag{3.7}$$

where c_G is gravity-wave phase speed. The gravitational acceleration $g = 9.8\ \mathrm{m\,s^{-2}}$. Combining Eqn (3.6) and (3.7), the relation between α and z is determined given H and f. Therefore, the geometry of the RIS is an important factor in determining the response of gravity-wave forcing of the ice shelf.

The pressure perturbation decay curve at the RIS front ($H \approx 700$ m) is determined at 20, 50, and 100 mHz (Fig. 3.5b). Lower-frequency gravity-wave pressure perturbations reach greater depths, illustrated by frequency-dependent α values at 206 m depth (base of the ice shelf front). At 50 mHz (corresponding to 20 s period swell), $\alpha = 0.13$, only about 13 % of pressure perturbation at 50 mHz signal reaching the base of the ice shelf front at 200 m depth. Furthermore, at 100 mHz, $\alpha = 2.5 \times 10^{-4}$, resulting in little energy from wave-induced pressure perturbations above 100 mHz reaching the base of the ice shelf. In contrast, at 20 mHz, $\alpha = 0.73$, indicating most of the low-frequency wave energy penetrates into the sub-shelf cavity. Pressure perturbations beneath the ice shelf couple with the ice and excite flexural-gravity waves.

Gravity-wave-induced pressure perturbations at the ice front can also excite extensional deformation. Since most of the wave energy below 20 mHz penetrates into the sub-shelf cavity, coupling with the ice shelf will occur at the ice-water interface. In contrast, because little higher-frequency (swell band) wave energy reaches the shelf base, energy exchange between swell and the ice shelf will occur primarily at the shelf front. Therefore, flexural-gravity waves and flexural waves are expected to be low-frequency dominant, while extensional Lamb waves are expected to be high-frequency dominant.

In summary, there are three wave types that are predicted to be observed at frequencies below 100 mHz:

1. Extensional Lamb waves, S_0^*, are observed at higher frequencies ($>$ 20 mHz) and are generated by swell impacts at the ice shelf front.

2. Flexural waves, also observed at higher frequencies ($>$ 20 mHz) where the gravity restoring force is weak, are generated by coupling of gravity-wave energy in the sub-shelf cavity with the ice shelf. Because the pressure from gravity waves decreases exponentially with depth, the wave energy penetrating the sub-shelf cavity is low at higher frequencies, and the flexural-wave amplitudes are expected to be weak, if observable.

3. Flexural-gravity waves, in the frequency band where the gravity restoring force has a significant effect, are generated by coupling of long-period gravity-wave energy in the ice-water system at the ice-shelf base. These are expected to have greater amplitudes at lower frequencies ($<$ 20 mHz).

The 20 mHz cutoff is based on the RIS observations at the extended center subarray (Fig. 3.1a).

3.4 Methods

3.4.1 Frequency-Domain Beamforming

Beamforming is an array processing method that combines elements of an array to reduce incoherent signals, utilizing constructive interference at particular azimuths and phase slownesses so that the azimuths and phase slownesses of coherent signals can be determined [Johnson and Dudgeon 1993; Van Trees 2002]. The ice-shelf beamforming response depends on array geometry and signal wavelength. With the same station separation, a larger array aperture improves the slowness resolution if the signals at all stations are coherent.

The data matrix $\boldsymbol{d}$, for either vertical (Z), north (N), or east (E) component, is an $m \times n$ matrix, where m is the number of stations, while n is the number of data samples. For each azimuth θ to be checked, the horizontal components are transformed to radial (R) and transverse (T) directions with

$$\begin{aligned} \boldsymbol{d}_R &= \boldsymbol{d}_N \cos\theta + \boldsymbol{d}_E \sin\theta \\ \boldsymbol{d}_T &= \boldsymbol{d}_N \sin\theta - \boldsymbol{d}_E \cos\theta, \end{aligned} \tag{3.8}$$

where $\boldsymbol{e}_i$ $(i = N, E, R, T)$ represents the corresponding direction vector.

Let $\boldsymbol{D}$ be the element-wise phase of the Fourier transform of $\boldsymbol{d}$. For each frequency bin centered at f, $\boldsymbol{D}(f)$ is an $m \times 1$ vector. The steering vector $\boldsymbol{q}$ for a plane wave coming from the azimuth θ with wavenumber $\boldsymbol{k}$, representing the phase delay at each station, is given by

$$\boldsymbol{q} = \begin{bmatrix} \exp(-j\boldsymbol{k}\cdot\boldsymbol{r}_1) \\ \exp(-j\boldsymbol{k}\cdot\boldsymbol{r}_2) \\ \vdots \\ \exp(-j\boldsymbol{k}\cdot\boldsymbol{r}_m) \end{bmatrix}, \tag{3.9}$$

where $j = \sqrt{-1}$, while $\boldsymbol{r}_i$ is the position of the ith station. Then, the phase-only frequency-domain beamforming response is obtained by

$$b = (\boldsymbol{D}^H \boldsymbol{q})^H \boldsymbol{D}^H \boldsymbol{q} = \boldsymbol{q}^H \boldsymbol{M} \boldsymbol{q}, \tag{3.10}$$

where $\boldsymbol{M} = \boldsymbol{D}\boldsymbol{D}^H$; the superscript "H" denotes the Hermitian.

For the RIS geometry, the ice-front source location is so close to the array that a large aperture makes the plane-wave assumption questionable. In addition, aliasing, the artifact in beamforming output, is another array-geometry-related problem that affects beamforming quality. The main signal can be difficult to identify with beamforming at a particular frequency because of aliasing in the azimuth-slowness domain. Tests showed that the least aliased results were obtained by restricting the stations used in beamforming to the center subarray (DR06, DR07, DR08, DR09, DR10, DR11, DR12, DR13, DR14, and RS04) with five neighboring stations (DR04, DR05, DR15, RS03, and RS05), together called the extended center subarray (Fig. 3.1a, 15 stations in total, with ∼150-km aperture). This array has an aperture about 3 and 30 times of the S_0 and A_0 wavelengths at 50 mHz, respectively.

3.4.2 Time-Domain Cross-Correlation

Cross-correlation is used to characterize signal similarity and time delay between two stations with applications in many scientific fields, including glaciology [e.g. Scambos et al. 1992], seismology [e.g. Chen, Gerstoft, and Bromirski 2016], and acoustics [e.g. Sabra, Roux, and Kuperman 2005]. The time-domain cross-correlation function (CCF) $f_{cc}(t)$ of two real-valued functions $s_1(t)$ and $s_2(t)$ is defined as

$$f_{cc}(t) = \int_{-\infty}^{\infty} s_1(\tau - t) s_2(\tau) \mathrm{d}\tau. \tag{3.11}$$

If $s_1(t)$ and $s_2(t)$ represent the records of a propagating signal at different receivers, the t value at the $f_{cc}(t)$ envelope peak, or $\underset{t}{\text{argmax}}\,\text{envelope}[f_{cc}(t)]$, indicates the time delay between $s_1(t)$ and $s_2(t)$. Assuming a signal propagating along a linear array, the time delay between two receivers depends on the receiver separation, with a plot of the separation between each receiver pair versus their respective time delay forming a straight line whose slope gives the group speed of the signal.

3.4.3 Frequency-Domain Particle Motion Analysis

Particle motion analysis follows [Vidale 1986], [Jurkevics 1988], and [Diez et al. 2016] in this paper. For each time segment, the data matrix $\boldsymbol{p}$ is a $3 \times n_p$ matrix, where the three rows denote the three components (vertical, north, and east), while n_p is the number of data samples for each component. Let $\boldsymbol{P}$ be the frequency-domain transformation of $\boldsymbol{p}$. For each frequency bin centered at f, $\boldsymbol{P}(f)$ is an 3×1 vector. The cross spectral density matrix $\boldsymbol{C}(f)$ for each data segment is obtained by

$$\boldsymbol{C}(f) = \boldsymbol{P}(f)\boldsymbol{P}^H(f). \tag{3.12}$$

Then $\boldsymbol{C}(f)$ is averaged over three neighboring time segments to get a more reliable value. The frequency-dependent maximum polarization is determined by the eigenvector $\boldsymbol{e}_0(f)$ associated with the largest eigenvalue of $\boldsymbol{C}(f)$. For each frequency bin, the direction of maximum polarization $\boldsymbol{e}_0'$ is obtained by

$$\boldsymbol{e}_0' = \boldsymbol{e}_0 \mathrm{e}^{i\psi'}, \quad \text{with} \quad \psi' = \underset{\psi}{\text{argmax}} \,\| \,\text{Re}(\boldsymbol{e}_0 \mathrm{e}^{i\psi})\|, \tag{3.13}$$

where $\text{Re}(\cdot)$ denotes real part and $\|\cdot\|$ the L2 norm. The azimuth and incident angle of $\boldsymbol{e}_0'$ are defined as for $\text{Re}(\boldsymbol{e}_0')$, giving the maximum polarization direction. Specifically, azimuth θ is the clockwise angle between the horizontal component of the maximum polarization and true north

(strike), or

$$\theta = \tan^{-1} \frac{\mathrm{Re}(e'_{0E})}{\mathrm{Re}(e'_{0N})}, \tag{3.14}$$

where e'_{0E} and e'_{0N} are the east and north components of $\boldsymbol{e}'_0$, respectively. Incident angle ϕ is the angle between the maximum polarization and the vertical downward direction, or

$$\phi = \left| \tan^{-1} \frac{\sqrt{[\mathrm{Re}(e'_{0E})]^2 + [\mathrm{Re}(e'_{0N})]^2}}{\mathrm{Re}(e'_{0Z})} \right|. \tag{3.15}$$

where e'_{0Z} is the vertical component of $\boldsymbol{e}'_0$. With $\mathrm{Im}(\cdot)$ denoting the imaginary part, ellipticity ε is defined as

$$\varepsilon = \frac{\| \mathrm{Im}(\boldsymbol{e}_0 e^{i\psi'}) \|}{\| \mathrm{Re}(\boldsymbol{e}_0 e^{i\psi'}) \|}, \tag{3.16}$$

indicating linear polarization ($\varepsilon = 0$), elliptical polarization ($0 < \varepsilon < 1$), or circular polarization ($\varepsilon = 1$).

In addition, particle motion polarization is also reflected in the phase delay between vertical and horizontal components. Assuming a signal is propagating southward, the phase difference between the vertical component and the north component is an indicator of whether the particle motion is prograde (negative), linear (0), or retrograde (positive) (Fig. S3.1).

3.5 Results

3.5.1 Observed Plate Waves Excited by Swell

Background

The responses of the RIS to ocean swell were recorded by the RIS stations with significant seasonal variation. Ten to twenty swell events per month were recorded in austral summer. A

typical strong swell event was recorded during the 2015 austral summer from 19 February 02:00 to 21 February 10:00, which had high amplitude and a clear dispersion trend, and did not overlap other swell events (Fig. 3.6). Assuming deep water ($k_G H \gg 1$), a stationary source region, and simultaneous generation of the waves over the entire swell band, the source distance d can be estimated from

$$\mathrm{d}f/\mathrm{d}t = g/4\pi d, \tag{3.17}$$

where f is center frequency of swell, t is time [Munk et al. 1963]. Since $\mathrm{d}f/\mathrm{d}t \approx 31$ mHz/22 h, as shown by Fig. 3.6c, we have $d \approx 2000$ km, which is about the distance to a modeled regional significant wave height storm event in the Southern Ocean between the RIS and New Zealand (Fig. S3.2), the likely source location of the waves for this swell event.

Ice shelf vibrations excited by swell impacts show significant attenuation away from the ice front [Figure 6, Bromirski et al. 2017]. Swell-band amplitudes were much higher at ice-front station (DR02) than at non-ice-front stations (DR10, DR16) (Fig. 3.6d). The rapid power decrease away from the ice front was in part due to the decay of evanescent modes and/or damped traveling flexural-gravity wave modes. Vertical displacements (LHZ) decayed faster than horizontal components (LHN for north-south, LHE for east-west), revealed by the greater attenuation from DR02 to DR10 on the LHZ channel than on the LHN channel. There are two possible reasons: (1) ice-shelf vertical vibration energy can leak into water layer, or (2) the vertical component may contain more evanescent and/or damped traveling energy. The spectrum of the vertical component at DR16 was augmented by the local transient events that masked the attenuation from DR10.

Source direction and dispersion

Beamforming shows that the dominant source directions were between NNE and NNW, pointing to the shelf front (Fig. 3.7a,b). Although swell energy is predominantly in the 30–

100 mHz band, coherent plate waves were also observed below this band. In particular, flexural-gravity waves were observed well below 20 mHz. This is confirmed by close agreement between the beamformed dispersion curve and the theoretical flexural-gravity wave dispersion relation (Fig. 3.8). Both the radial and vertical components show coherent energy. Below 20 mHz, the frequency of the peak power in Fig. 3.8b was 2.9 mHz at slowness of 15 $\mathrm{s\,km^{-1}}$, giving a phase speed of 66.7 $\mathrm{m\,s^{-1}}$. The flexural-gravity wave horizontal motions were much larger than the vertical motions, resulting in part from the horizontal motions of the forcing gravity waves being much larger than the vertical motions at low frequencies (Fig. S3). The rough base of the ice shelf facilitates coupling of gravity-wave horizontal forcing into flexural-gravity waves, resulting in relatively large horizontal motions.

In the 20–100 mHz band, the dominant slowness was between 0.3 and 0.4 $\mathrm{s\,km^{-1}}$ without observable dispersion, consistent with S_0^* propagation (Fig. 3.8). The dominant source direction was from the NNE at lower frequencies and NNW at higher frequencies (same for the 28 strongest swell events from January to October 2015), possibly due to variability of the dominant swell impact region along the ice front (Fig. 3.7c,d). The frequency of the peak power was 53 mHz, and the corresponding slowness was 0.34 $\mathrm{s\,km^{-1}}$, giving a phase speed of 2.94 $\mathrm{km\,s^{-1}}$ (Fig. 3.8). The radial component was more coherent than the vertical component, consistent with the theoretical expectation that S_0^* has horizontal motions much larger than vertical motions.

A spectral peak in the swell band was observed between 60 and 70 mHz on both vertical and horizontal components (Fig. 3.6d). Although extensional Lamb waves were observed on the radial component in the beamforming analysis, coherent flexural waves were not observed on any component in this band, suggesting that the spectral peak of the vertical component was due to loss of flexural wave coherence. Based on the dispersion curves in Fig. 3.5a, the wavelengths of the flexural waves (purple) in the 20–100 mHz band are 2.8–5.3 km (280 $\mathrm{m\,s^{-1}}$/100 mHz=2.8 km, 106 $\mathrm{m\,s^{-1}}$/20 mHz=5.3 km), while the wavelengths of the flexural-gravity waves (green) at 3 mHz (not shown) are about 22.2 km (66.6 $\mathrm{m\,s^{-1}}$/3 mHz=22.2 km). The shorter wavelengths in the

20–100 mHz band resulted in the flexural waves being less coherent in that frequency band, likely in part a consequence of the larger station spacing (5–20 km) compared with the signal wavelengths.

Beamforming analysis for the 28 strongest swell events from January to October 2015 indicates that flexural-gravity waves were always observed below 20 mHz, with extensional Lamb waves occurring above 20 mHz. OASES modeling (Fig. S4) shows that both flexural waves above 20 mHz and extensional Lamb waves below 20 mHz can propagate in a 300 m ice layer coupled with a 400 m water layer above the seafloor, the AIWB model (Fig. 3.3). Therefore, the dominance of a particular wave type was likely due to the ice-water coupling described in the plate wave generation mechanism rather than due to the model structure constraints on wave propagation.

As an additional verification, north-south (NS) and west-east (WE) subarrays are chosen to study the wave propagation direction and group speed with cross-correlation. Below 5 mHz, the dominant coherent signal, flexural-gravity waves, were non-dispersive. In other words, group speed was equal to phase speed and was constant in this band. A coherent signal propagating southward at $\sim$66 $\mathrm{m\,s^{-1}}$ group speed was indicated by the 2–4 mHz filtered CCFs of the LHZ and LHN components (Fig. 3.9a,b), consistent with the beamforming analysis. In the 20–100 mHz band, the dominant coherent signal, extensional Lamb waves, were non-dispersive. A coherent signal propagating southward at $\sim$3.2 $\mathrm{km\,s^{-1}}$ was indicated by the 20–100 mHz filtered CCFs of the LHN component (Fig. 3.9c), consistent with the beamforming analysis. No coherent signal was observed in the west-east direction (Fig. 3.9d). The high peaks of CCFs with small station separations are due to waveform similarity at nearby stations.

Particle motion

The azimuth, incident angle, and ellipticity of the maximum particle motion polarization during the swell event were obtained for DR02, DR10, and DR16 (Fig. 3.10), which were

$\sim$2 km, $\sim$100 km, $\sim$300 km south of the ice front, respectively. Particle motions at non-ice-front stations (e.g. DR10, DR16) had the following patterns: (1) The source azimuth was northerly, changing from NNE to NNW with increasing frequency in the 20–100 mHz band, consistent with the beamforming analysis and with the expectation that swell impacting the shelf front excites these signals. (2) Below 10 mHz, incident angle variability indicates that the maximum polarization was horizontal, due to coupling with the shallow-water gravity waves that have mostly horizontal particle motions. In the 20–100 mHz band, the maximum polarization was horizontal, characteristic of extensional Lamb waves. Estimates of the incident angle (Fig. 3.10b) in the 10–20 mHz band at DR10 have a wide range, possibly indicating a transition band between flexural-gravity wave domination and extensional Lamb wave domination. (3) Ellipticity analysis (Fig. 3.10c) indicates that the maximum polarization was an oblate ellipse both below 10 mHz and in the 20–100 mHz band. Combining the ellipticity and incident angle distributions, the major axis of the oblate ellipse was horizontal in both frequency bands. In the 10–20 mHz band, the polarization was close to circular as a result of low signal-to-noise-ratio that affects horizontal/vertical ratios in the transition band.

Particle motions at ice-front stations (e.g. DR02) differed from those at non-ice-front locations in the following respects: (1) The source azimuth cannot be constrained well at the ice front, and (2) the maximum polarization was vertical in the 20–100 mHz band at the ice front. Both observations could be the effect of the evanescent modes and/or the damped traveling modes of flexural-gravity waves that were not observed at non-front stations.

These observations indicate that the dominant signal propagated roughly north to south, away from the shelf front. Therefore, linear, prograde, and retrograde particle motions correspond to 0, negative, and positive phase difference between the vertical component and the north component, respectively. This vertical-north phase difference was frequency dependent, shown in Fig. 3.11. The positive phase difference in the 1–10 mHz band indicates retrograde particle motion, consistent with flexural-gravity-wave propagation [Robinson 1983]. The phase lag

changed significantly in the transition band, i.e. 10–20 mHz, and dropped to near 0 above 20 mHz at stations south of DR06, probably due to the vertical component decaying below the detection level. The phase lag at stations north of DR06 was positive and greater than 40° above 20 mHz, indicating retrograde particle motion, which is consistent with extensional Lamb wave propagation.

3.5.2 Plate Waves Excited by Tsunami and IG Waves

Plate waves were also observed during tsunami impacts between 17 and 19 September 2015 and during a strong IG arrival between 5 and 8 May 2015 [Bromirski et al. 2017]. Coherent extensional Lamb waves were not observed during tsunami excitation, but were observed in the 20–30 mHz band during the IG event. Low energy levels above 20 mHz during the tsunami explain this difference. However, flexural-gravity waves were observed below 20 mHz, similar to that observed during the swell event. Importantly, flexural-gravity waves were observable even during most "quiet" days both in spectra and in beamforming analysis, indicating that flexural-gravity waves were generated continuously by the persistent IG waves throughout the year. These year-round vibrations can potentially weaken the ice by expanding existing fractures [Holdsworth and Glynn 1978; Bromirski et al. 2017].

3.6 Discussion

Gravity-wave amplitudes are expected to vary considerably along the Antarctic coast, with associated forcing on ice shelves dependent on the source amplitude, location, spectral content, and continental shelf bathymetry. Continuous gravity-wave impacts promote crack expansion and iceberg calving, facilitating the progressive reduction of ice shelf buttressing over time. VLP, IG, and swell synoptic variability associated with individual storms will differentially impact

different regions along the Antarctic coast at different times. Year-round ice shelf seismic records at the RIS and PIG ice shelves allow inferences about the general characteristics of gravity-wave spatial variability and their impact (Fig. 3.12).

Noticeably lower spectral amplitudes were observed at PIG during January to March 2013 in the swell band (30–100 mHz) (Fig. 3.12), which we hypothesize is due to PIG being partly shielded from Amundsen Sea wave activity mainly by the Thurston Island, the King Peninsula, and the Canisteo Peninsula. Also, the PIG ice shelf front is oriented roughly north-south (orthogonal to the West Antarctica coast). Typical eastward storm tracks would tend to result in oblique gravity-wave approach angles to PIG shelf front, which could reduce the response. The higher spectral levels at PIG compared with RIS in the austral winter at frequencies > 60 mHz can be explained in part by PIG being farther north where sea ice cover is typically less and not as persistent, so the overall winter damping of swell is less. These location-related differences result in the comparatively high amplitude spectral levels at RIS during February, represented by the 95th percentile peak at DR04 near 60 mHz (Fig. 3.12c). These factors combine to produce more low-level background energy at PIG, while sea ice north of the RIS front damps the shorter period gravity-wave energy at DR04 at frequencies > 60 mHz during the austral winter. Importantly, Thwaites, Dotson, Getz, and other West Antarctic ice shelves are more exposed than PIG to gravity waves coming from the open waters of the Amundsen Sea, which should result in higher-amplitude gravity waves at certain coastal locations compared to PIG.

The apparent year-round persistence of VLP band energy at both RIS and PIG suggests that this forcing is common at all ice shelves. Spectral levels are higher at the RIS at < 20 mHz, but VLP band energy is also present at PIG. Presumably flexural-gravity waves are the source of the energy at PIG in this band, although the PIG array aperture precludes identification of VLP signals with beamforming. Note the much higher IG band peak levels at RIS (about 20 dB higher) compared with PIG near 6 mHz, likely resulting from less flexural-gravity wave energy at PIG.

As the PIG ice shelf is shielded by the northern promontories and the PIG front is oriented

roughly north-to-south, swell events likely rarely excite strong vibrations of the PIG ice shelf. Only one clear swell event was recorded during the 2013 austral summer from 12 March 12:00 to 14 March 00:00. The same analysis methods used for the RIS observations were applied to the PIG seismic data. Coherent signals from the west were identified above 20 mHz on the vertical component (Fig. 3.13), consistent with generation at the PIG shelf front. The slowness resolution is low due to the small array aperture. Thus, it cannot be determined whether coherent signals exist below 10 mHz. However, in contrast to the RIS, dispersion curve analysis of the vertical component at the PIG ice shelf shows that flexural waves exist above 20 mHz (Fig. 3.14a) in addition to flexural-gravity waves below 20 mHz (Fig. 3.14a) and extensional Lamb waves (Fig. 3.14b). Flexural waves are detected at the PIG ice shelf in part because the PIG seismic array is close to the ice front ($\sim$25 km) so that the flexural waves are less attenuated, and also because the relatively small station separation of the PIG array ($\sim$1–2 km, less than the flexural wave wavelengths) allows identification of coherent signals from the shorter-wavelength higher-frequency swell-induced flexural waves.

Flexural-gravity wave energy attenuates with distance from an ice shelf front, but observations indicate that there is still substantial wave-induced energy 100 km from the RIS front [Bromirski et al. 2017]. Significantly less flexural-gravity wave energy is observed at larger ranges from the front such that much of the RIS is little affected by this forcing. In contrast, smaller ice shelves, such as the PIG ice shelf, Thwaites ice tongue, and Dotson and Getz ice shelves, have grounding zones that are on the order of 100 km or less from their fronts. Thus, for smaller shelves, the entire shelf is subjected to flexural-gravity wave forcing and associated fracture expansion, as well as potentially affecting grounding zone stability.

3.7 Conclusions

We deployed a 34-station seismic array on the RIS from November 2014 to November 2016 to study its response to long-period gravity-wave impacts. Between January and October 2015, we observed 28 non-overlapping strong swell events. For one of the strongest events (February 2015), we observed two types of plate waves: dispersive flexural-gravity waves below 20 mHz and non-dispersive extensional Lamb waves in the 20–100 mHz band, both propagating landward from the RIS front. Seismic array beamforming revealed that flexural-gravity waves, propagating at close to shallow-water gravity-wave speeds, dominated the coherent signal below 20 mHz. However, coherent flexural waves were not observed at RIS in the 20–100 mHz band even though vertical motions were strong, probably because the station spacing of the RIS beamformed subarray (5–20 km) is significantly longer than the wavelengths of flexural waves (2.8–5.3 km) in the 20–100 mHz band, resulting in lower coherence between stations.

We compared the response of the large stable RIS with the Pine Island Glacier (PIG) ice shelf using seismic data collected by a 5-station array deployed on the PIG ice shelf from January 2012 to December 2013, with the PIG array located closer to the ice front than the RIS beamforming array and with smaller station spacing. In contrast to RIS, beamforming of the PIG seismic data showed evidence of flexural waves above 20 mHz, likely detectable because of the smaller station spacing. Lower flexural-gravity wave spectral levels in the infragravity (IG) band at the PIG ice shelf compared with the RIS indicates that less gravity wave energy impacts PIG, partly due the orientation of the PIG ice front relative to IG wave propagation direction and shielding by northern promontories.

Our results improve the understanding of the response of Antarctic ice shelves to long-period gravity wave forcing. We conclude that because of the ubiquitous storm activity in the Southern Ocean, most, if not all, West Antarctic ice shelves are likely subjected to gravity-wave impacts that excite plate waves. However, significant differences in gravity wave forcing are

expected as a result of storm track and storm intensity, as well as the orientation of the ice front relative to gravity wave arrivals and the shielding of ice shelves by promontories. In this respect, it seems likely that the Thwaites Glacier tongue, Dotson, Getz, and other Amundsen coast ice shelves are more exposed than PIG to gravity waves arriving from the north. Persistent excitation of relatively high-amplitude flexural-gravity waves induce dynamic strains that can expand existing fractures and thus affect ice shelf integrity and their evolution.

Acknowledgements

We thank the two reviewers for their valuable suggestions. This study was funded by the U.S. National Science Foundation (EAR-1147435 [Sandwell] and EAR-1147436 [Dolan]) and the Southern California Earthquake Center (SCEC). SCEC is funded by the NSF Cooperative Agreement EAR-1033462 and USGS Cooperative Agreement G12AC20038. Optical data and fault trace maps were provided by the USGS and CICESE. ERS and ENVISAT data were provided by ESA and were obtained from the WInSAR archive. ALOS data were provided by JAXA and were acquired from ASF archive. GPS data were provided by UNAVCO and CICESE. We thank all of these facilities for their help on this study. The SCEC contribution number for this paper is 2076.

Remark

Chapter 3, in full, is a reprint of the material as it appears in Journal of Glaciology: Chen, Z., Bromirski, P.D., Gerstoft, P., Stephen, R.A., Wiens, D.A., Aster, R.C., Nyblade, A.A., 2018, "Ocean-excited plate waves in the Ross and Pine Island Glacier ice shelves", *Journal of Glaciology*, 64(247), pp.730-744. The dissertation author is the primary investigator and author of this paper.

Tables and Figures

Table 3.1: Model parameters. The parameters c_P, c_S, and ρ denote the P-wave speed, S-wave speed, and density of each layer. Parameters for air are for dry air at 15 °C at sea level. The c_P and c_S values of (intact) ice are calculated from Young's modulus $E = 6$ GPa and Poisson's ratio $\nu = 0.3$. Parameters for water are the approximate values for sea water. The bed properties for modeling S_0^* and A_0^* with OASES are those of the uppermost solid layer of PREM [Dziewonski and Anderson 1981]. The bed is assumed rigid to obtain a simpler analytical solution of flexural-gravity waves [Fox and Squire 1990].

	c_P ($\mathrm{m\,s^{-1}}$)	c_S ($\mathrm{m\,s^{-1}}$)	ρ ($\mathrm{kg\,m^{-3}}$)
air	340	0	1.225
ice	2959.0	1581.6	922.5
water	1500	0	1025
bed (S_0^*, flexural wave)	5800	3200	2600
bed (flexural-gravity wave)	∞	∞	∞

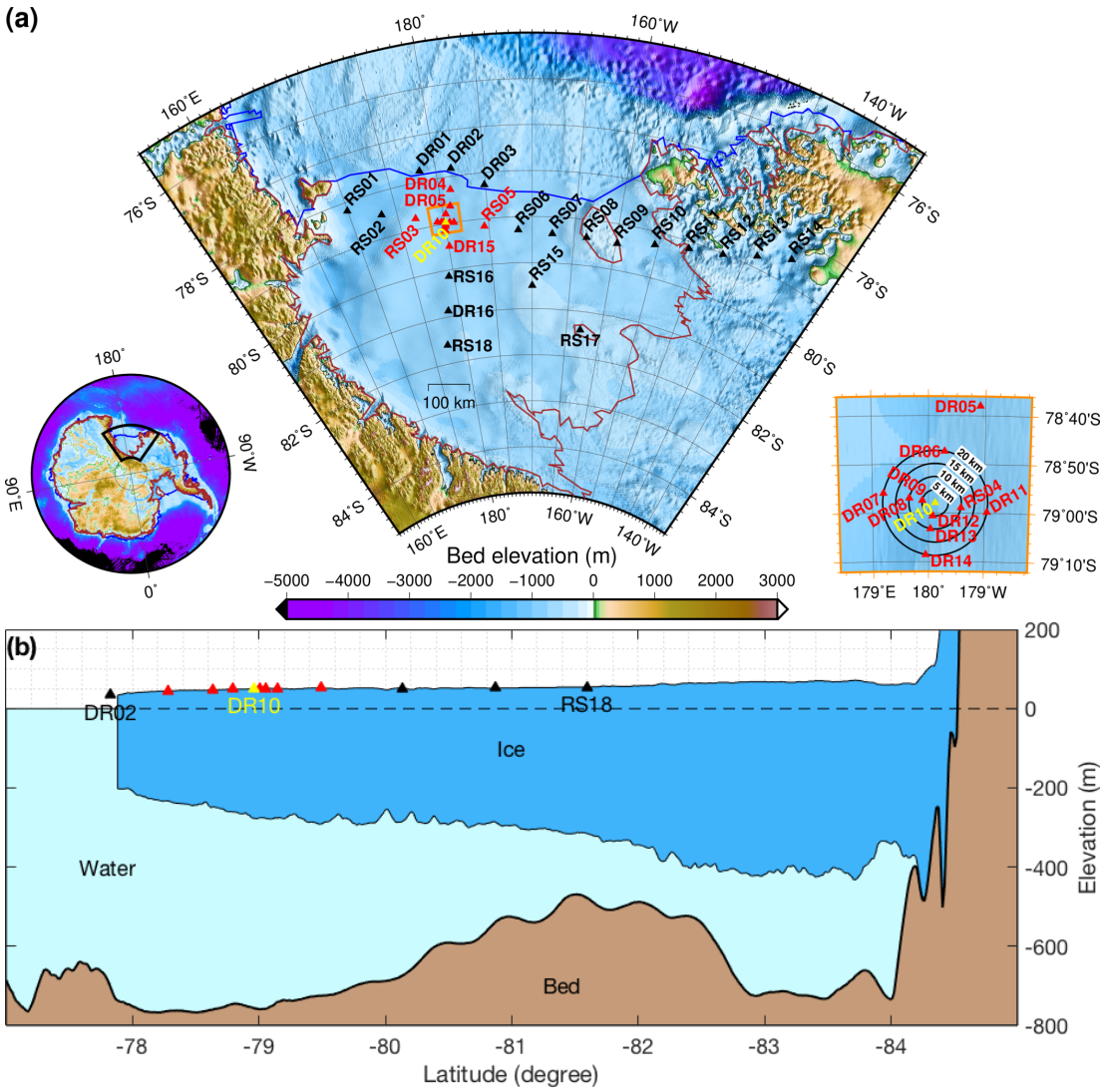

Figure 3.1: (a) The RIS seismic stations (triangles) superimposed on the bed elevation map [Fretwell et al. 2013], with the center station DR10 (yellow), extended center subarray (red) and other stations (black) indicated. The RIS is bounded by the grounding line (brown line) and the ice front (blue line). Expanded view of the dense center subarray (orange box) is shown in the right inset, where the contours of distance to DR10 are shown (black circles). (b) Cross-section along the 180° meridian [Fretwell et al. 2013]. DR02 is off the ice front because the ice front has moved northward, but the ice thickness model has not been updated.

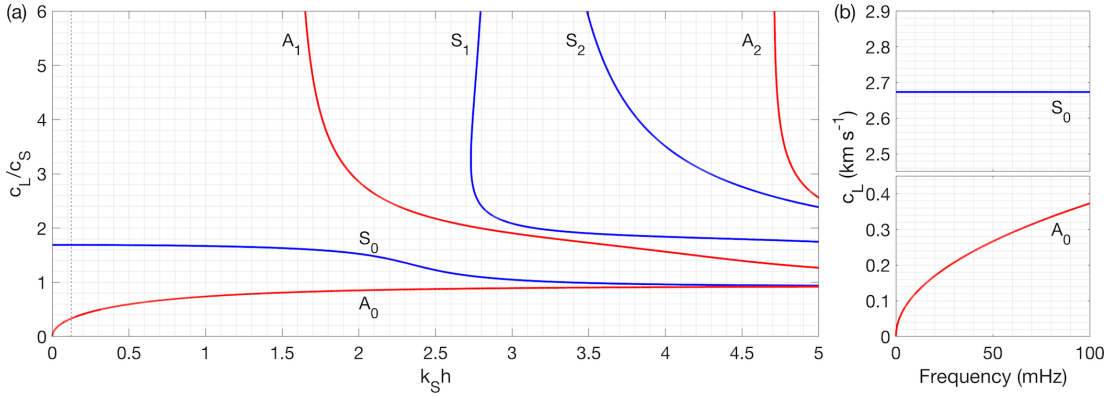

Figure 3.2: (a) Dispersions curves of free-space Lamb waves for Poisson's ratio $\nu = 0.3$. The horizontal axis is the product of the S-wave wavenumber k_S and the half plate thickness h, with the vertical axis the Lamb-wave phase speed c_L normalized by S-wave speed c_S. The low-frequency part of the curves ($k_S h < 0.12$, left of the black dashed line) resulting from low-frequency gravity-wave forcing applies to the RIS observations. (b) Dispersion curves of free-space Lamb waves in the vacuum-ice-vacuum (VIV) model (see Fig. 3.3).

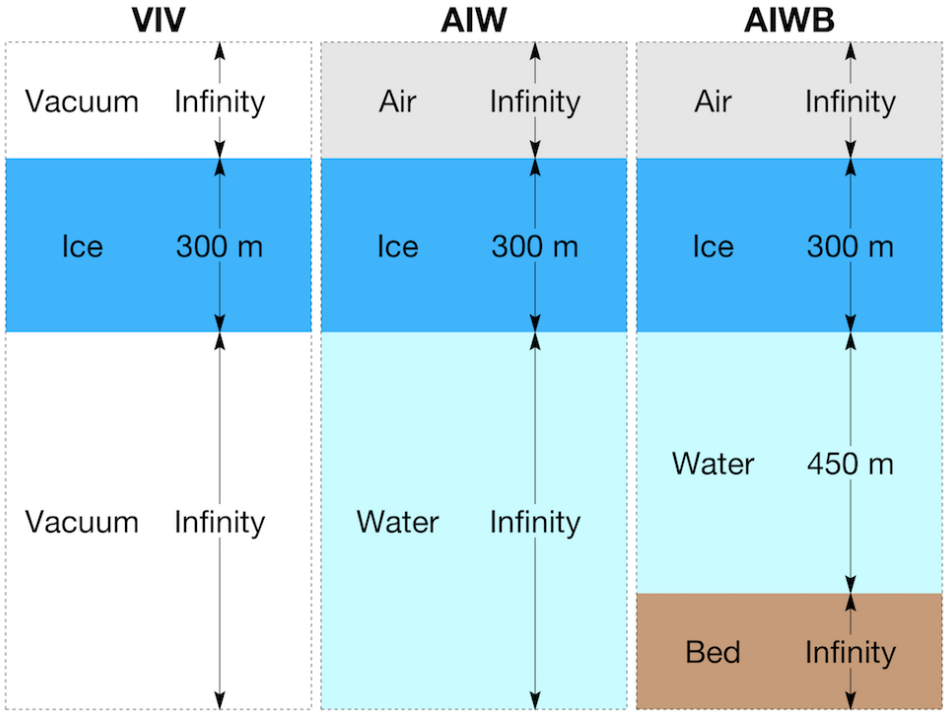

Figure 3.3: Model geometry for vacuum-ice-vacuum (VIV), air-ice-water (AIW), and air-ice-water-bed (AIWB) cases. The layer properties are given in Table 3.1.

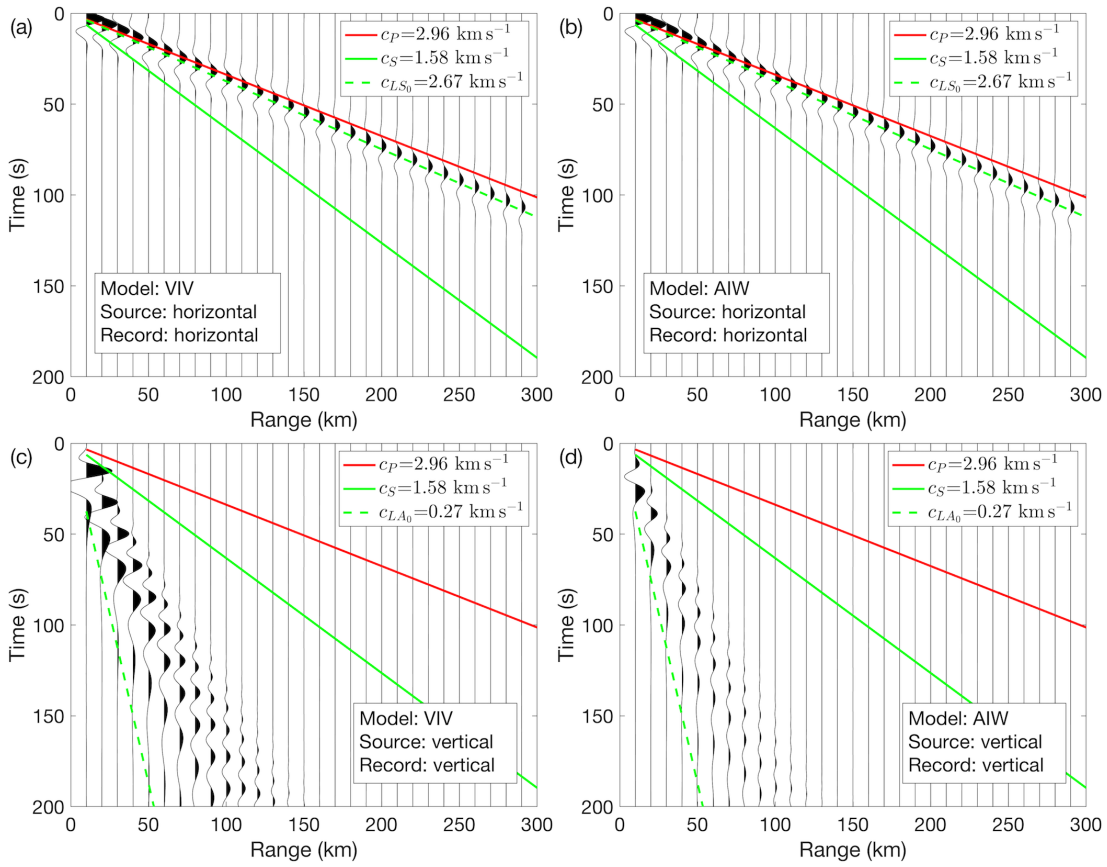

Figure 3.4: Synthetic seismograms of the (a,b) horizontal (radial) component and (c,d) vertical component on the ice layer surface in model VIV (a,c) and AIW (b,d). The source function is a Ricker wavelet centered at 50 mHz, with a horizontal point force in (a,b) and vertical point force in (c,d). The normalizations for horizontal motions in (c) and (d) are 10 times those of (a) and (b). P-wave speed (c_P, red solid), S-wave speed (c_S, green solid), and fundamental free-space Lamb-wave phase speeds (c_{LS_0} and c_{LA_0}, green dashed) at 50 mHz are indicated.

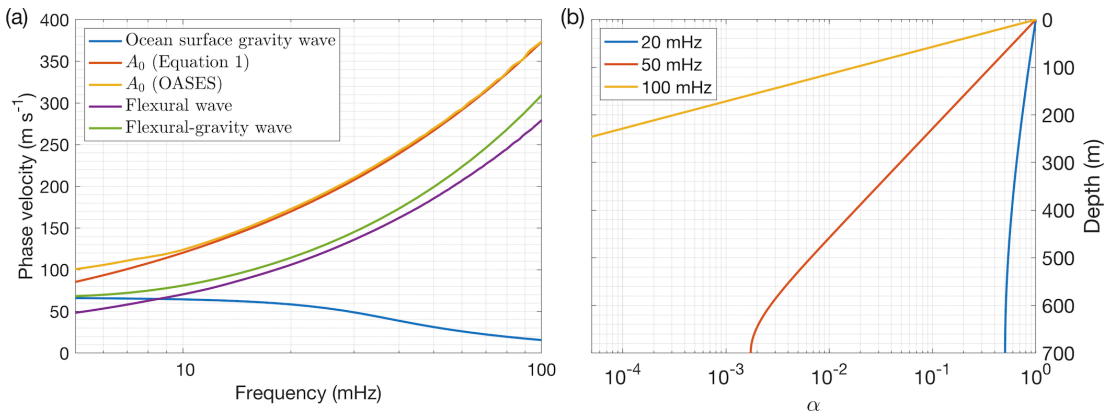

Figure 3.5: (a) Dispersion curve comparison. The A_0 dispersion curve for the free-space ice plate in the VIV model is calculated by solving Eqn (3.1) (red), and by numerical modeling using OASES (yellow). The flexural wave dispersion curve of the floating ice plate in the AIWB model (purple) is calculated from numerical modeling with OASES. The dispersion curves from OASES modeling are smoothed using a moving average 15 mHz window. The thin-plate flexural-gravity-wave dispersion curve of the floating ice plate in the AIWB model (green) is based on [Fox and Squire 1990]. The ocean-surface-gravity-wave dispersion curve (blue) of a water layer of 450 m depth is given for reference. (b) The ratio between gravity-wave pressure perturbation amplitude at depth z and at surface, or $\alpha(z)$, in a water layer of depth $H = 700$ m, according to Eqn (3.6).

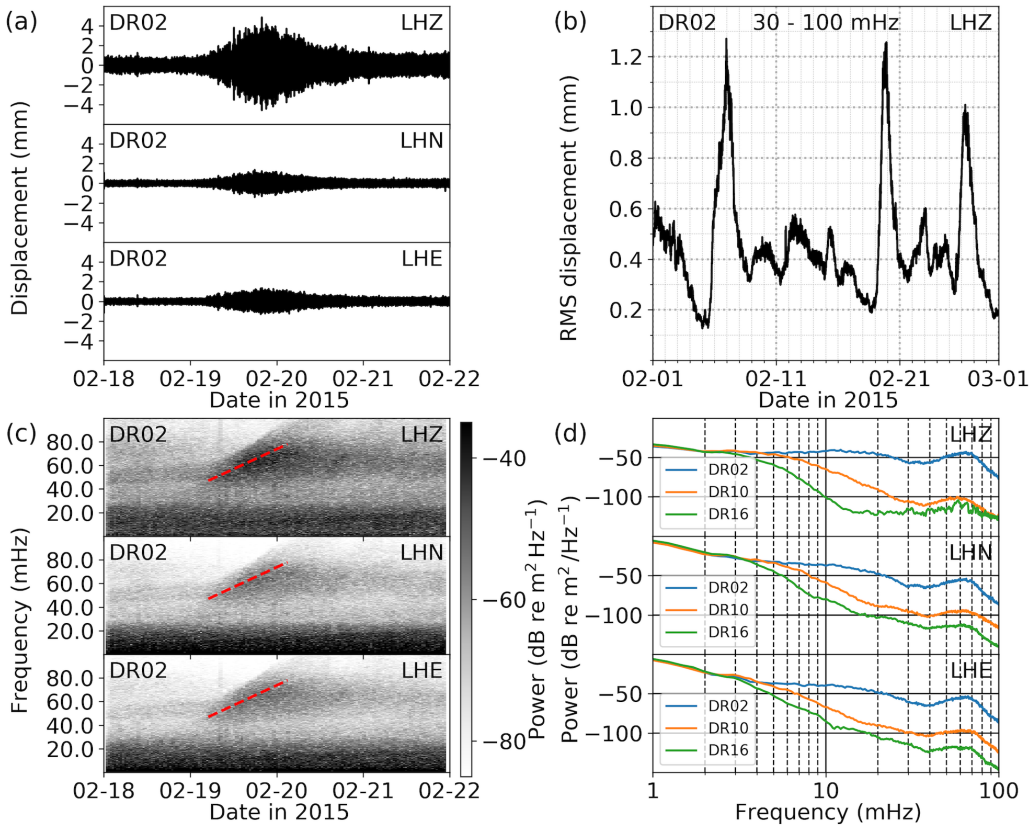

Figure 3.6: RIS response to a swell event from 02:00 on 19 February to 10:00 on 21 February, 2015: (a) 4-day seismograms at DR02 (bandpassed 30–100 mHz). (b) Root-mean-square (RMS) of the vertical displacements at DR02 (bandpassed 30–100 mHz) in February 2015. RMS window length is 4096 s. (c) Displacement spectrogram at DR02. The dispersion trend slope (red dashed) indicates a source distance of about 2000 km. (d) Displacement spectrum at DR02 (blue), DR10 (orange), and DR16 (green) from 19 February 02:00 to 21 February 10:00. The vertical LHZ, and horizontal LHN and LHE components are indicated in each subplot.

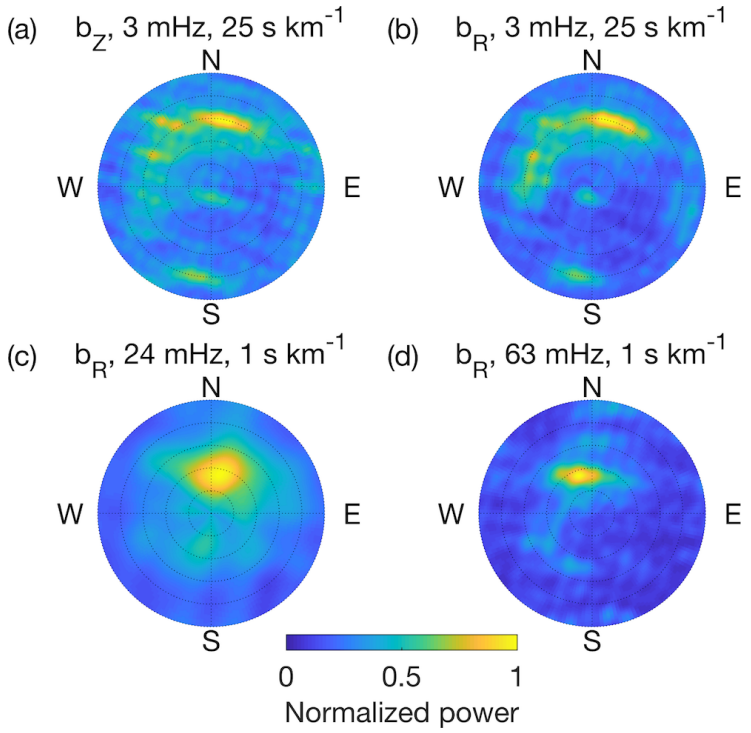

Figure 3.7: RIS response to a swell event from 02:00 on 19 February to 10:00 on 21 February, 2015: Phase-only beamforming of (a) the vertical component at 3 mHz, and the radial component at (b) 3, (c) 24, and (d) 63 mHz. For each subplot, the azimuth corresponds to the signal incoming direction, while the radial axis represents slownesses that vary from 0 at the center to the maximum slowness given in each subplot title. The peak-power regions give dominant signal incoming directions and slownesses. The signal incoming directions are clear and characteristic at these selected frequencies. Processing FFT window length is 4096 s, with step size of 2048 s. Beamforming power levels are normalized to the maximum value at each frequency in each subplot.

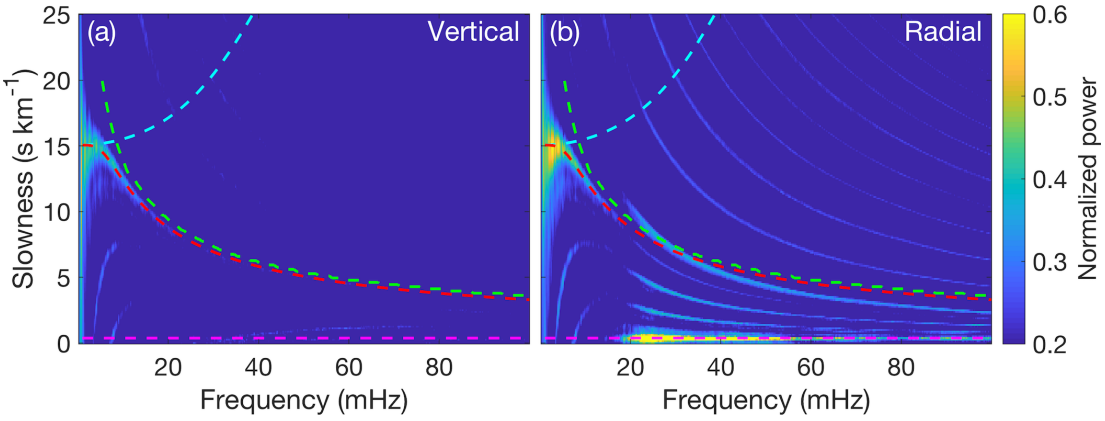

Figure 3.8: RIS response to a swell event from 02:00 on 19 February to 10:00 on 21 February, 2015: Dispersion curves of (a) vertical and (b) radial components, obtained by averaging the beamforming output over 0° to 20° azimuth (the north-south line subarray is roughly along 10°). Phase speed dispersion curves of ocean surface gravity waves (cyan), flexural waves (green), flexural-gravity waves (red), and S_0^* (magenta) in the AIWB model (see Fig. 3.3) are overlaid for comparison. The subplots are normalized to the maximum value over the two subplots.

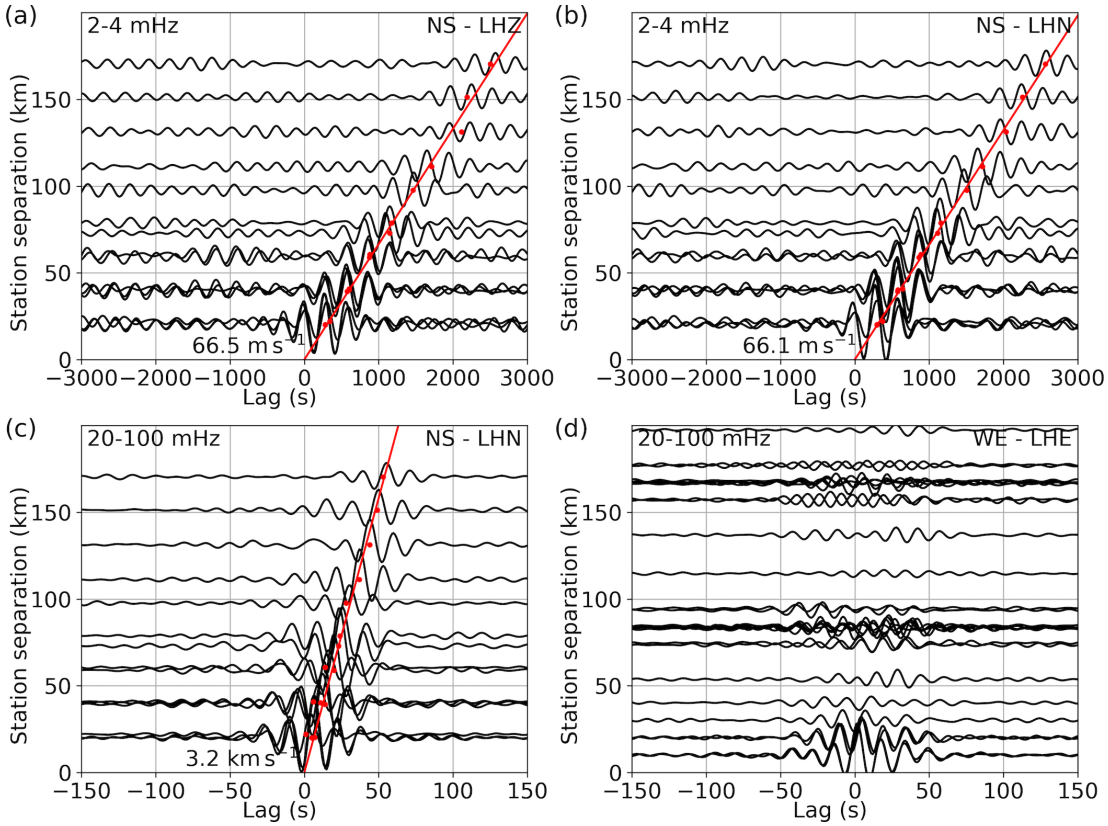

Figure 3.9: RIS response to a swell event from 02:00 on 19 February to 10:00 on 21 February, 2015: (a) Cross-correlation functions of the LHZ channel between north-south (NS) subarray stations (DR05, DR06, DR10, DR14, DR15, RS16) (bandpassed 2–4 mHz). (b) Cross-correlation functions of the LHN channel within NS subarray (bandpass filtered, 2–4 mHz). (c) Cross-correlation functions of the LHN channel within NS subarray (bandpassed 20–100 mHz). (d) Cross-correlation functions of the LHE channel between the west-east (WE) subarray stations (RS01, RS02, RS03, DR07, DR10, RS04, DR11, RS05, RS06, RS07) (bandpass filtered, 20–100 mHz). The raw data were demeaned, filtered, and cross-correlated between each station pair in time domain. The peak positions of the cross-correlation function envelopes are indicated by red dots, which are fitted by the red line constrained to go through (0, 0).

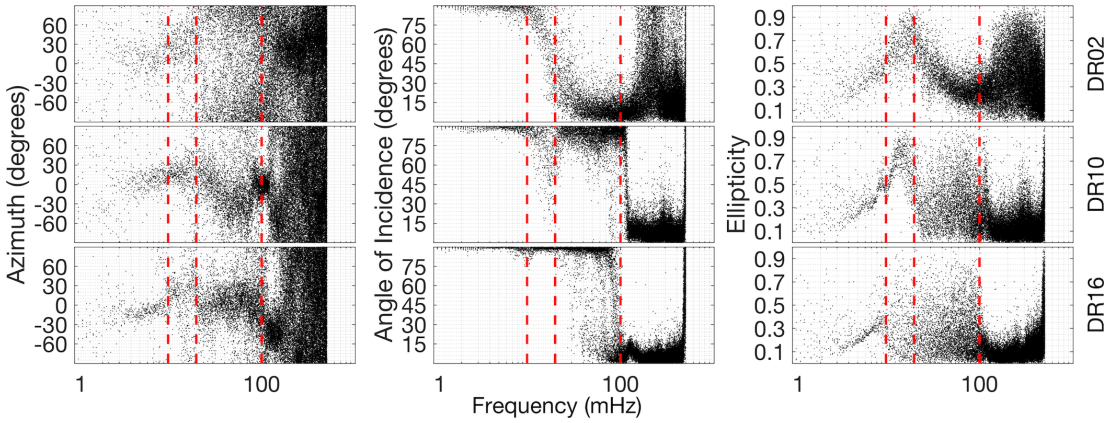

Figure 3.10: RIS response to a swell event from 02:00 on 19 February to 10:00 on 21 February, 2015: Frequency-dependent azimuth (left column), angle of incidence (middle column), and ellipticity (right column) at DR02 (top row), DR10 (middle row), and DR16 (bottom row). The time series were partitioned into 16384 s (4 h 33 min 4 s) windows overlapped by half window length, resulting in a frequency-bin width of 60 μHz. Each dot represents the estimated parameter in that time window at the corresponding frequency bin. The three vertical red dashed lines indicate 10, 20, and 100 mHz, respectively.

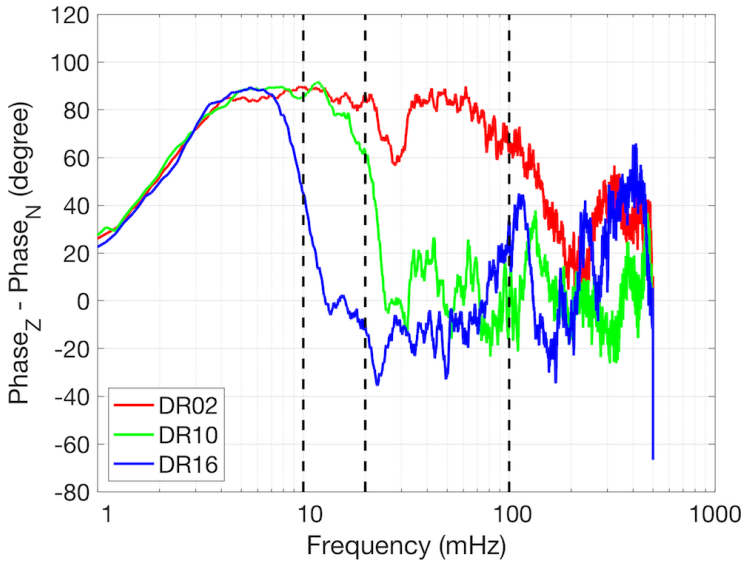

Figure 3.11: RIS response to a swell event from 02:00 on 19 February to 10:00 on 21 February, 2015: Frequency-dependent phase lag between vertical component and north component at selected stations. Positive lags indicate retrograde motions. Negative lags indicate prograde motions. Zero lag indicates linear polarization or a noisy time period. The time series were partitioned into 2.28 h windows, with a half window-length overlap. The phase lag is calculated by averaging the phase difference between FFTs between the vertical and north components over all windows. To identify dominant features, the phase lag curve was then smoothed by 20-point moving average. The three vertical black dashed lines indicate 10, 20, and 100 mHz respectively.

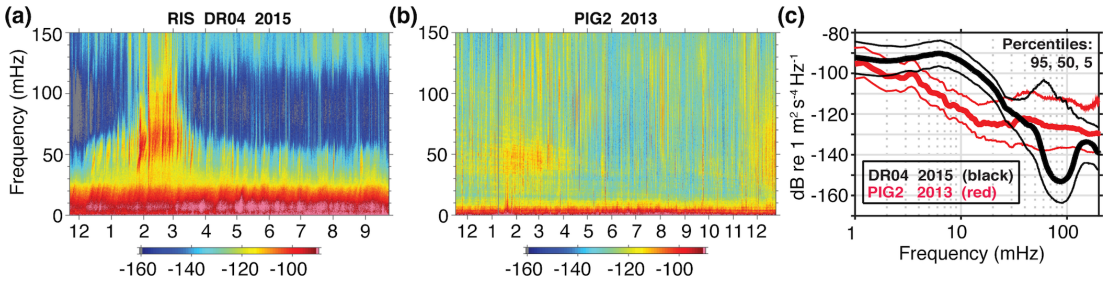

Figure 3.12: Acceleration response power spectral density spectrograms (in dB re 1 $m^2 s^{-4} Hz^{-1}$) at (a) RIS seismic station DR04, located about 50 km south of the RIS ice front, and at (b) the PIG2 seismic station about 24 km east of the PIG ice shelf front, collected as part of the Observing Pine Island Glacier project [D. Holland and Bindschadler 2012]. Months are indicated by the x-axis tick labels. (c) Spectra with percentile spectral levels obtained at DR04 and PIG2 for the time periods of the spectrograms shown.

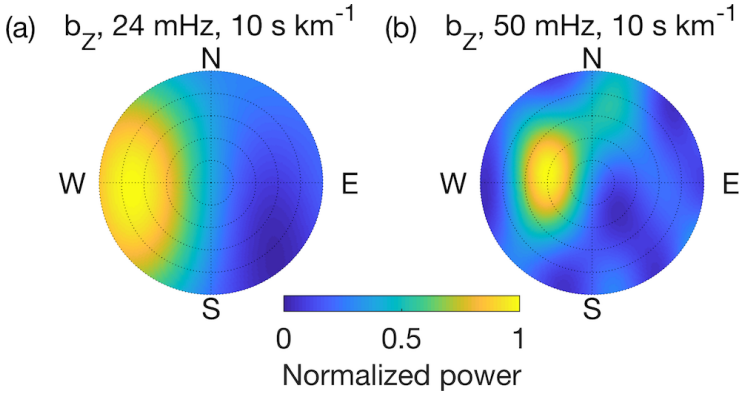

Figure 3.13: PIG ice shelf response to a swell event from 12:00 on 12 March to 00:00 on 14 March, 2013: Phase-only beamforming of the vertical component at (a) 24 mHz and (b) 50 mHz. For each subplot, the azimuth corresponds to the signal incoming direction, while the radial axis represents slownesses that vary from 0 at the center to the maximum slowness given in each subplot title. The peak-power regions give dominant signal incoming directions and slownesses. The signal incoming directions are clear and characteristic at these selected frequencies. Processing FFT window length is 4096 s, with step size 2048 s. Windows with missing data are discarded. Beamforming power levels are normalized to the maximum value at each frequency in each subplot.

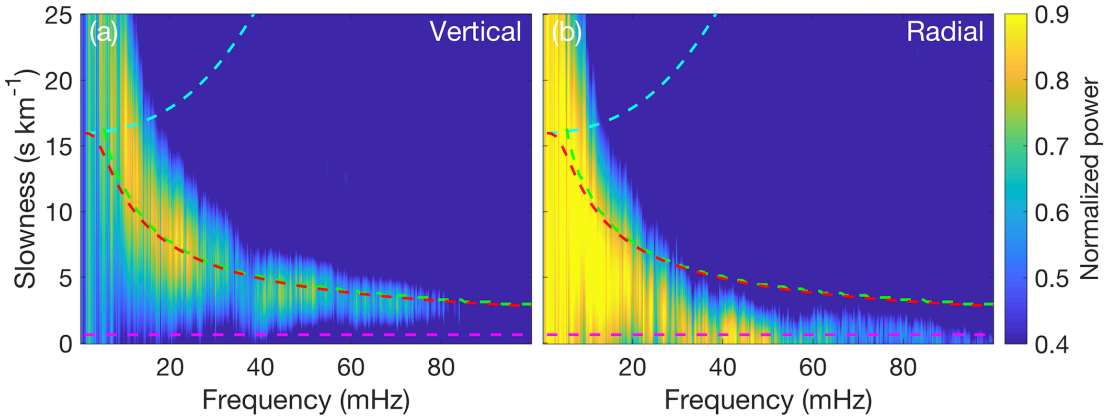

Figure 3.14: PIG ice shelf response to a swell event from 12:00 on 12 March to 00:00 on 14 March, 2013: Dispersion curves of (a) vertical and (b) radial components, obtained by averaging the beamforming output over 260° to 280° azimuth (20° azimuth range centered due west). Phase speed dispersion curves of ocean surface gravity waves (cyan), flexural waves (green), flexural-gravity waves (red), and S_0^* (magenta) in the AIWB model (see Fig. 3.3) are overlaid for comparison. An ice thickness of 460 m and a water depth of 400 m were used to compute the dispersion curves, representing the PIG ice shelf geometry at the array area [Fretwell et al. 2013]. The subplots are normalized to the maximum value over the two subplots.

Appendix

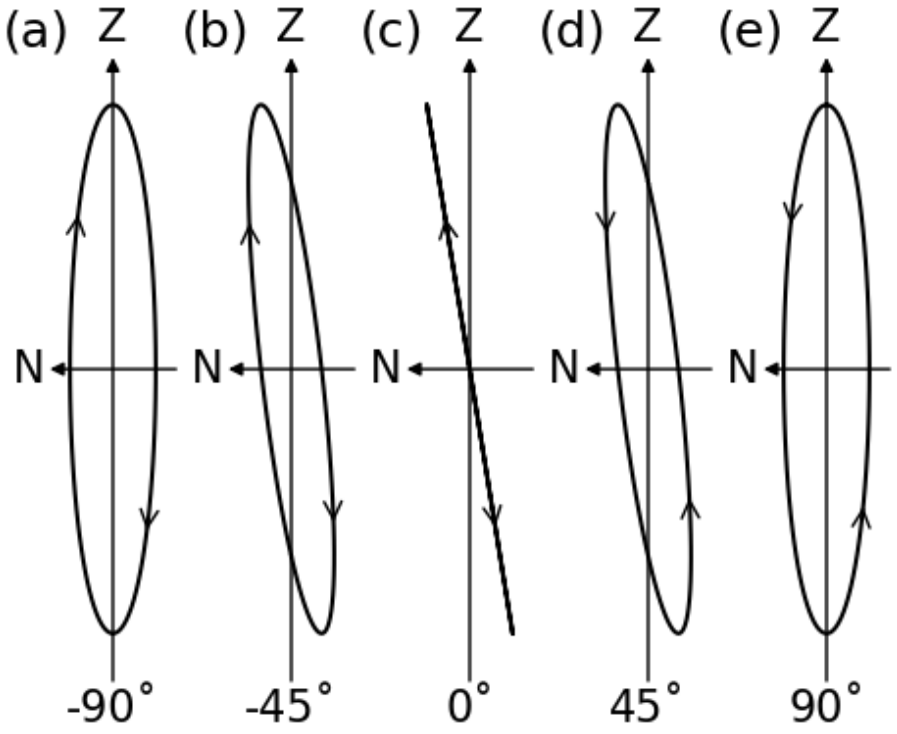

Figure S3.1: A sketch of retrograde (a, b), linear (c), and prograde (d, e) particle motions with the corresponding phase difference between vertical and north components indicated, assuming the signal is propagating from north to south.

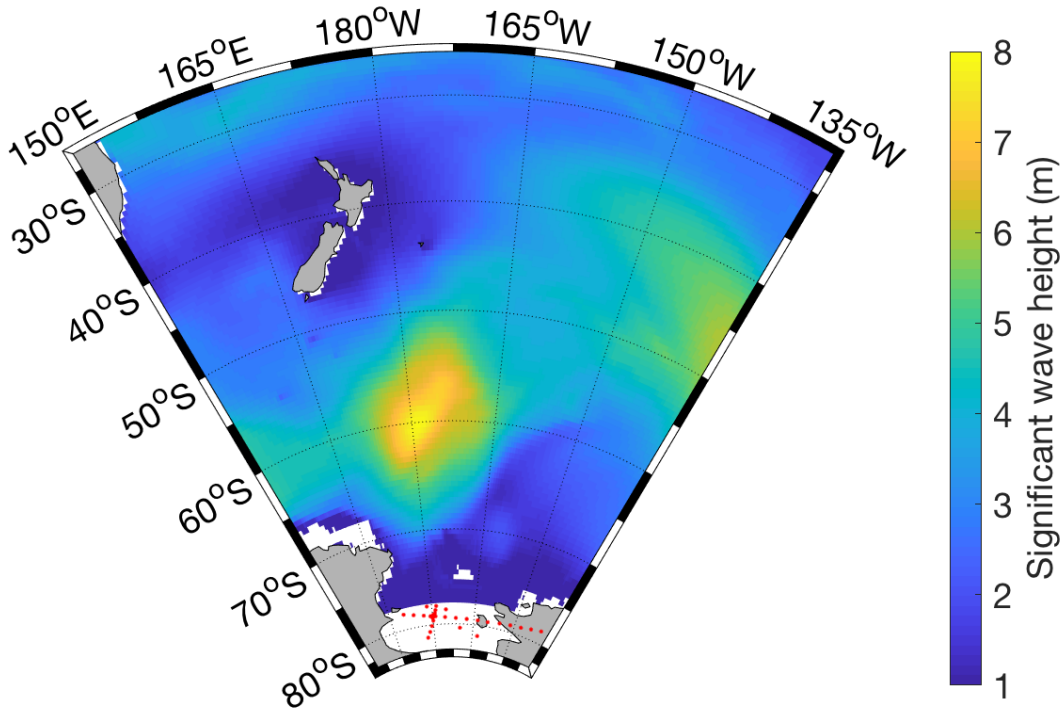

Figure S3.2: WAVEWATCH III significant wave height hindcast model [Tolman 2009] at 00:00 on 19 February 2015. The seismic stations are indicated by the red dots.

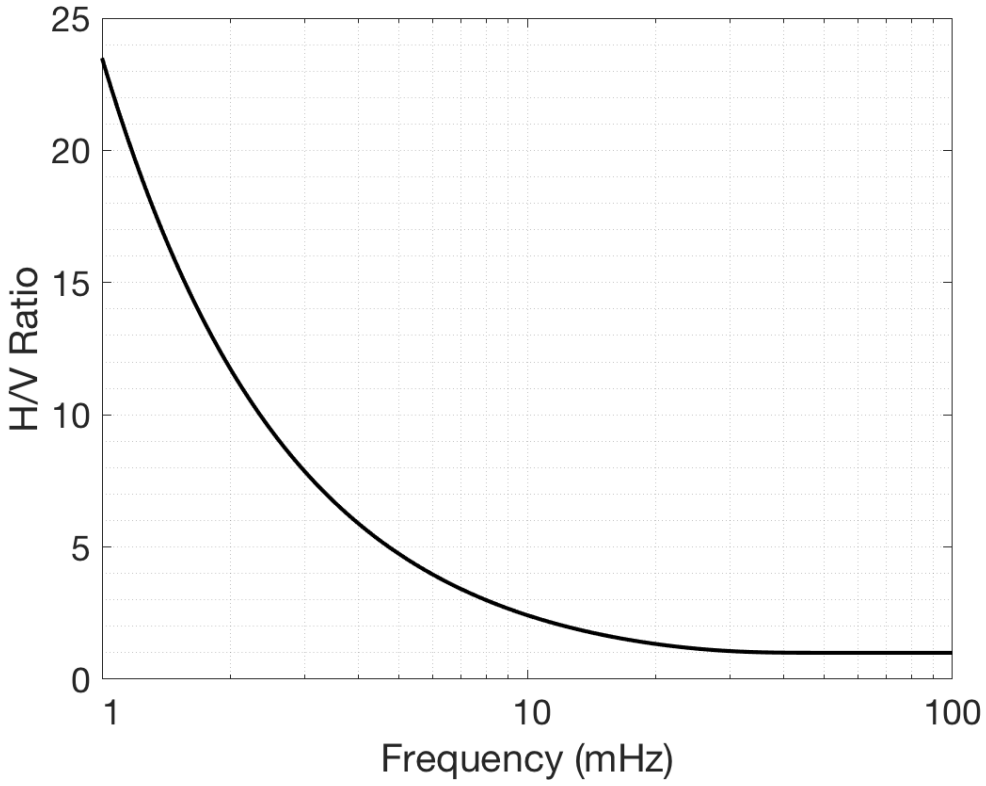

Figure S3.3: Horizontal-to-vertical (H/V) ratio of gravity-wave particle motions at the ocean surface, for a water depth of 450 m.

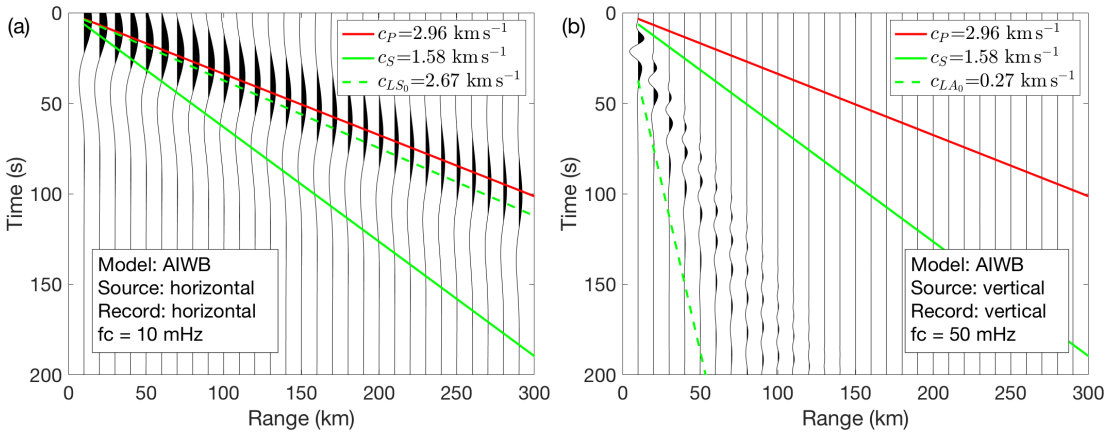

Figure S3.4: (a) Synthetic seismograms of the horizontal (radial) component on the ice-layer surface in the AIWB model (Fig. 3). The source function is a Ricker wavelet centered at 10 mHz, with a horizontal point force. (b) Synthetic seismograms of the vertical component on the ice-layer surface in the AIWB model. The source function is a Ricker wavelet centered at 50 mHz, with a vertical point force. The normalization factor of (b) is 100 times that of (a). P-wave speed (c_P, red solid), S-wave speed (c_S, green solid), and fundamental free-space Lamb-wave phase speeds (c_{LS_0}) and c_{LA_0}, green dashed) at the corresponding Ricker wavelet center frequency are indicated.

References

Bindschadler, R., Vaughan, D. G., and Vornberger, P. (2011). "Variability of basal melt beneath the Pine Island Glacier ice shelf, West Antarctica". In: *Journal of Glaciology* 57.204, pp. 581–595. DOI: 10.3189/002214311797409802.

Bromirski, P. D., Chen, Z., Stephen, R. A., Gerstoft, P., Arcas, D., Diez, A., Aster, R. C., Wiens, D. A., and Nyblade, A. (2017). "Tsunami and infragravity waves impacting Antarctic ice shelves". In: *Journal of Geophysical Research: Oceans* 122.7, pp. 5786–5801. DOI: 10.1002/2017JC012913.

Bromirski, P. D., Diez, A., Gerstoft, P., Stephen, R. A., Bolmer, T., Wiens, D. A., Aster, R. C., and Nyblade, A. (2015). "Ross ice shelf vibrations". In: *Geophysical Research Letters* 42.18, pp. 7589–7597. DOI: 10.1002/2015GL065284.

Bromirski, P. D., Sergienko, O. V., and MacAyeal, D. R. (2010). "Transoceanic infragravity waves impacting Antarctic ice shelves". In: *Geophysical Research Letters* 37.2. DOI: 10.1029/2009GL041488.

Brunt, K. M., Okal, E. A., and MacAyeal, D. R. (2011). "Antarctic ice-shelf calving triggered by the Honshu (Japan) earthquake and tsunami, March 2011". In: *Journal of Glaciology* 57.205, pp. 785–788. DOI: 10.3189/002214311798043681.

Chapman, C. C., Hogg, A. M., Kiss, A. E., and Rintoul, S. R. (2015). "The dynamics of Southern Ocean storm tracks". In: *Journal of Physical Oceanography* 45.3, pp. 884–903. DOI: 10.1175/JPO-D-14-0075.1.

Chen, Z., Gerstoft, P., and Bromirski, P. D. (2016). "Microseism source direction from noise cross-correlation". In: *Geophysical Journal International* 205.2, pp. 810–818. DOI: 10.1093/gji/ggw055.

Christianson, K., Bushuk, M., Dutrieux, P., Parizek, B. R., Joughin, I. R., Alley, R. B., Shean, D. E., Abrahamsen, E. P., Anandakrishnan, S., Heywood, K. J., Kim, T.-W., Lee, S. H., Nicholls, K., Stanton, T., Truffer, M., Webber, B. G. M., Jenkins, A., Jacobs, S. S., Bindschadler, R., and Holland, D. M. (2016). "Sensitivity of Pine Island Glacier to observed ocean forcing". In: *Geophysical Research Letters* 43.20, pp. 10817–10825. DOI: 10.1002/2016GL070500.

Diez, A., Bromirski, P., Gerstoft, P., Stephen, R., Anthony, R., Aster, R., Cai, C., Nyblade, A., and Wiens, D. (2016). "Ice shelf structure derived from dispersion curve analysis of ambient seismic noise, Ross Ice Shelf, Antarctica". In: *Geophysical Journal International* 205.2, p. 785. DOI: 10.1093/gji/ggw036.

Dziewonski, A. M. and Anderson, D. L. (1981). "Preliminary reference Earth model". In: *Physics of the Earth and Planetary Interiors* 25.4, pp. 297–356. DOI: 10.1016/0031-9201(81)90046-7.

Fox, C. and Squire, V. A. (1990). "Reflection and transmission characteristics at the edge of shore fast sea ice". In: *Journal of Geophysical Research: Oceans* 95.C7, pp. 11629–11639. DOI: 10.1029/JC095iC07p11629.

— (1991). "Coupling between the ocean and an ice shelf". In: *Annals of Glaciology* 15, pp. 101–108. DOI: 10.3189/1991AoG15-1-101-108.

Fretwell, P., Pritchard, H. D., Vaughan, D. G., Bamber, J. L., Barrand, N. E., Bell, R., Bianchi, C., Bingham, R. G., Blankenship, D. D., Casassa, G., Catania, G., Callens, D., Conway, H., Cook, A. J., Corr, H. F. J., Damaske, D., Damm, V., Ferraccioli, F., Forsberg, R., Fujita, S., Gim, Y., Gogineni, P., Griggs, J. A., Hindmarsh, R. C. A., Holmlund, P., Holt, J. W., Jacobel, R. W., Jenkins, A., Jokat, W., Jordan, T., King, E. C., Kohler, J., Krabill, W., Riger-Kusk, M., Langley, K. A., Leitchenkov, G., Leuschen, C., Luyendyk, B. P., Matsuoka, K., Mouginot, J., Nitsche, F. O., Nogi, Y., Nost, O. A., Popov, S. V., Rignot, E., Rippin, D. M., Rivera, A., Roberts, J., Ross, N., Siegert, M. J., Smith, A. M., Steinhage, D., Studinger, M., Sun, B., Tinto, B. K., Welch, B. C., Wilson, D., Young, D. A., Xiangbin, C., and Zirizzotti, A. (2013). "Bedmap2: improved ice bed, surface and thickness datasets for Antarctica". In: *Cryosphere* 7.1, pp. 375–393. DOI: 10.5194/tc-7-375-2013.

Graff, K. F. (1991). *Wave Motion in Elastic Solids*. Revised Edition. Dover Publications. ISBN: 9780486667454.

Herbers, T. H. C., Elgar, S., and Guza, R. T. (1995). "Generation and propagation of infragravity waves". In: *Journal of Geophysical Research: Oceans* 100.C12, pp. 24863–24872. DOI: 10.1029/95JC02680.

Holdsworth, G. and Glynn, J. (1978). "Iceberg calving from floating glaciers by a vibrating mechanism". In: *Nature* 274.5670, pp. 464–466. DOI: 10.1038/274464a0.

Holland, D. and Bindschadler, R. (2012). *Observing Pine Island Glacier (PIG) ice shelf deformation and fracture using a GPS and Seismic Network*. International Federation of Digital Seismograph Networks. Other/Seismic Network. DOI: 10.7914/SN/XC_2012.

Jacobs, S. S., Hellmer, H. H., and Jenkins, A. (1996). "Antarctic Ice Sheet melting in the southeast Pacific". In: *Geophysical Research Letters* 23.9, pp. 957–960. DOI: 10.1029/96GL00723.

Johnson, D. H. and Dudgeon, D. E. (1993). *Array Signal Processing: Concepts and Techniques*. Prentice Hall. ISBN: 9780130485137.

Joughin, I., Rignot, E., Rosanova, C. E., Lucchitta, B. K., and Bohlander, J. (2003). "Timing of Recent Accelerations of Pine Island Glacier, Antarctica". In: *Geophysical Research Letters* 30.13. DOI: 10.1029/2003GL017609.

Joughin, I., Smith, B. E., and Holland, D. M. (2010). "Sensitivity of 21st century sea level to ocean-induced thinning of Pine Island Glacier, Antarctica". In: *Geophysical Research Letters* 37.20. DOI: 10.1029/2010GL044819.

Jurkevics, A. (1988). “Polarization analysis of three-component array data”. In: *Bulletin of the Seismological Society of America* 78.5, pp. 1725–1743.

Kundu, P. K., Cohen, I. M., and Dowling, D. R. (2011). *Fluid Mechanics*. Fifth Edition. Academic Press. ISBN: 9780123821003.

Lamb, H. (1889). “On the flexure of an elastic plate”. In: *Proceedings of the London Mathematical Society* s1-21.1, pp. 70–91. DOI: 10.1112/plms/s1-21.1.70.

— (1917). “On waves in an elastic plate”. In: *Proceedings of the Royal Society of London A: Mathematical, Physical and Engineering Sciences* 93.648, pp. 114–128. DOI: 10.1098/rspa.1917.0008.

Lipovsky, B. P. (2018). “Ice Shelf Rift Propagation and the Mechanics of Wave-Induced Fracture”. In: *Journal of Geophysical Research: Oceans* 123. DOI: 10.1029/2017JC013664.

MacAyeal, D. R. (1987). “Ice-Shelf Backpressure: Form Drag Versus Dynamic Drag”. In: *Dynamics of the West Antarctic Ice Sheet*. Ed. by C. J. Van der Veen and J. Oerlemans. Dordrecht: Springer Netherlands, pp. 141–160. ISBN: 9789400937451.

MacAyeal, D. R., Okal, E. A., Aster, R. C., Bassis, J. N., Brunt, K. M., Cathles, L. M., Drucker, R., Fricker, H. A., Kim, Y.-J., Martin, S., Okal, M. H., Sergienko, O. V., Sponsler, M. P., and Thom, J. E. (2006). “Transoceanic wave propagation links iceberg calving margins of Antarctica with storms in tropics and Northern Hemisphere”. In: *Geophysical Research Letters* 33.17. DOI: 10.1029/2006GL027235.

Massom, R. A., Scambos, T. A., Bennetts, L. G., Reid, P., Squire, V. A., and Stammerjohn, S. E. (2018). “Antarctic ice shelf disintegration triggered by sea ice loss and ocean swell”. In: *Nature* 558.7710, pp. 383–389. DOI: 10.1038/s41586-018-0212-1.

Medley, B., Joughin, I., Smith, B. E., Das, S. B., Steig, E. J., Conway, H., Gogineni, S., Lewis, C., Criscitiello, A. S., McConnell, J. R., Broeke, M. R. van den, Lenaerts, J. T. M., Bromwich, D. H., Nicolas, J. P., and Leuschen, C. (2014). “Constraining the recent mass balance of Pine Island and Thwaites glaciers, West Antarctica, with airborne observations of snow accumulation”. In: *Cryosphere* 8.4, pp. 1375–1392. DOI: 10.5194/tc-8-1375-2014.

Munk, W. H., Miller, G. R., Snodgrass, F. E., and Barber, N. F. (1963). “Directional Recording of Swell from Distant Storms”. In: *Philosophical Transactions of the Royal Society of London A: Mathematical, Physical and Engineering Sciences* 255.1062, pp. 505–584. DOI: 10.1098/rsta.1963.0011.

Paolo, F. S., Fricker, H. A., and Padman, L. (2015). “Volume loss from Antarctic ice shelves is accelerating”. In: *Science* 348.6232, pp. 327–331. DOI: 10.1126/science.aaa0940.

Pritchard, H. D., Ligtenberg, S. R. M., Fricker, H. A., Vaughan, D. G., Broeke, M. R. van den, and Padman, L. (2012). "Antarctic ice-sheet loss driven by basal melting of ice shelves". In: *Nature* 484, pp. 502–505. DOI: 10.1038/nature10968.

Rayleigh, L. (1888). "On the free vibrations of an infinite plate of homogeneous isotropic elastic matter". In: *Proceedings of the London Mathematical Society* s1-20.1, pp. 225–237. DOI: 10.1112/plms/s1-20.1.225.

Rignot, E., Casassa, G., Gogineni, P., Krabill, W., Rivera, A., and Thomas, R. (2004). "Accelerated ice discharge from the Antarctic Peninsula following the collapse of Larsen B ice shelf". In: *Geophysical Research Letters* 31.18. DOI: 10.1029/2004GL020697.

Robinson, E. S. (1983). "Flexural-gravity waves on floating stratified ice". In: *Journal of Glaciology* 29.101, pp. 133–141. DOI: 10.3189/S0022143000005207.

Sabra, K. G., Roux, P., and Kuperman, W. A. (2005). "Emergence rate of the time-domain Green's function from the ambient noise cross-correlation function". In: *Journal of the Acoustical Society of America* 118.6, pp. 3524–3531. DOI: 10.1121/1.2109059.

Scambos, T. A., Bohlander, J. A., Shuman, C. A., and Skvarca, P. (2004). "Glacier acceleration and thinning after ice shelf collapse in the Larsen B embayment, Antarctica". In: *Geophysical Research Letters* 31.18. DOI: 10.1029/2004GL020670.

Scambos, T. A., Dutkiewicz, M. J., Wilson, J. C., and Bindschadler, R. A. (1992). "Application of image cross-correlation to the measurement of glacier velocity using satellite image data". In: *Remote Sensing of Environment* 42.3, pp. 177–186. DOI: 10.1016/0034-4257(92)90101-O.

Scambos, T. A., Haran, T. M., Fahnestock, M. A., Painter, T. H., and Bohlander, J. (2007). "MODIS-based Mosaic of Antarctica (MOA) data sets: Continent-wide surface morphology and snow grain size". In: *Remote Sensing of Environment* 111.2, pp. 242–257. DOI: 10.1016/j.rse.2006.12.020.

Schmidt, H. (2004). *OASES version 3.1 user guide and reference manual*.

Sergienko, O. V. (2010). "Elastic response of floating glacier ice to impact of long-period ocean waves". In: *Journal of Geophysical Research: Earth Surface* 115.F4. DOI: 10.1029/2010JF001721.

— (2017). "Behavior of flexural gravity waves on ice shelves: Application to the Ross Ice Shelf". In: *Journal of Geophysical Research: Oceans* 122.8, pp. 6147–6164. DOI: 10.1002/2017JC012947.

Thoma, M., Jenkins, A., Holland, D., and Jacobs, S. S. (2008). "Modelling Circumpolar Deep Water intrusions on the Amundsen Sea continental shelf, Antarctica". In: *Geophysical Research Letters* 35.18. DOI: 10.1029/2008GL034939.

Tolman, H. L. (2009). “User manual and system documentation of WAVEWATCH III TM version 3.14”. In: *Technical Note, MMAB Contribution* 276.

Trenberth, K. E. (1991). “Storm tracks in the Southern Hemisphere”. In: *Journal of the Atmospheric Sciences* 48.19, pp. 2159–2178. DOI: 10.1175/1520-0469(1991)048<2159:STITSH>2.0.CO;2.

Uchiyama, Y. and McWilliams, J. C. (2008). “Infragravity waves in the deep ocean: Generation, propagation, and seismic hum excitation”. In: *Journal of Geophysical Research: Oceans* 113.C7. DOI: 10.1029/2007JC004562.

Van Trees, H. L. (2002). *Optimum Array Processing: Part IV of Detection, Estimation, and Modulation Theory*. Wiley-Interscience. ISBN: 9780471093909.

Vidale, J. E. (1986). “Complex polarization analysis of particle motion”. In: *Bulletin of the Seismological Society of America* 76.5, pp. 1393–1405.

Viktorov, I. A. (1967). *Rayleigh and Lamb waves: Physical Theory and Applications*. Plenum. ISBN: 9780306302862.

Chapter 4

Ross Ice Shelf Icequakes Associated with Ocean Gravity Wave Activity

Gravity waves impacting ice shelves illicit a suite of responses that can affect ice shelf integrity. Broadband seismometers deployed on the Ross Ice Shelf (RIS), complemented by a near-icefront seafloor hydrophone, establish the association of strong icequake activity with gravity wave amplitudes (A_G) below 0.04 Hz. The RIS-front seismic vertical displacement amplitudes (A_{SV}) are well-correlated with A_G, allowing determination of an empirical transfer function from A_G to A_{SV}. The A_{SV}/A_G ratio is 0.6–0.7 below 0.01 Hz, but decreases rapidly above 0.01 Hz. Strong icequake activity exhibits spatial and seasonal associations with different gravity wave frequency bands, dominated by austral summer activity for icefront icequakes when sea ice is minimal and swell impacts are strongest. Strong rift icequakes have weak seasonal variation, but tend to occur primarily in the austral winter when the strongest very-long-period gravity waves impact the RIS.

4.1 Introduction

Ice shelves play an important role in restraining the grounded ice discharge to the sea. Their integrity is thus crucial in moderating sea level rise. Ocean forcing can impact ice shelf integrity both thermally and dynamically. Although the internal glaciological stresses may be the dominant driving force of crevasse formation and expansion [Bassis et al. 2008], surface melt water can facilitate this process by providing additional pressure in fissures [Benn and Evans 2010], with basal melting thinning [Rignot et al. 2013] and thus weakening ice shelves. Stress perturbations from ocean gravity wave impacts [Lipovsky 2018] and tides [Wiens et al. 2008; Olinger et al. 2018] may also contribute to ice fracture and rift propagation, further reducing ice shelf integrity. At the ice front, persistent gravity wave forcing with intermittent strong impacts, including swell, infragravity (IG) waves, and tsunami, trigger iceberg calving, fatigue ice shelves, and even collapse weakened ice shelves [Bromirski, Sergienko, and MacAyeal 2010; Bromirski et al. 2017; Brunt, Okal, and MacAyeal 2011; Massom et al. 2018]. Seismological studies of the response of ice shelves to gravity wave forcing can provide valuable information on the forcing function and the ice shelf mechanical properties [e.g. Diez et al. 2016; Chen et al. 2018], which are important parameters in ice shelf modeling.

To better understand ice shelf dynamics associated with the response to gravity wave forcing, a 34-station broadband seismic array was deployed on the RIS between October 2014 and November 2016, with three stations positioned 2 km from the ice edge [Bromirski et al. 2015]. Each seismic station includes a three-component Nanometrics T120 PHQ seismometer, which was buried in the ice at depth of 1 m. Additionally, a three-component Nanometrics Trillium Compact broadband ocean bottom seismometer (OBS) system with a HighTech HTI-04-PCA/ULF hydrophone pressure sensor was deployed on the seafloor 8 km north of on-ice seismic station DR01 (6 km north of the ice shelf front, KPDR in Figure 4.1a) by the Korea Polar Research Institute (KOPRI) between Jan 17 and Dec 11, 2015. Few in-situ measurements of the

ocean waves near ice shelf fronts are available due to the harsh environment. The hydrophone observations allow estimation of gravity wave amplitudes (A_G) near the RIS front (Section 4.7.1). The concurrent deployment of an ocean bottom hydrophone and an on-ice broadband seismic station near the ice shelf front enables estimation of A_G and ice shelf vertical seismic displacements (A_{SV}) at the same time, allowing determination of an empirical ocean-wave-to-seismic transfer function for the first time.

Gravity wave forcing covers a wide frequency/period range, from less than 10 s (wind waves) to over 300 s (tsunamis). Here, we estimate an empirical transfer function from A_G to A_{SV} for the RIS. The RIS response is characterized in the swell (0.03–0.1 Hz, or 10–30 s), IG (0.003–0.02 Hz, or 50–300 s), and very-long-period (VLP, 0.003–0.001, or 300–1000 s) bands. Because ice fracturing is associated with rift propagation and iceberg calving, icequake activity is an indicator of changes in ice shelf integrity. The importance of gravity wave forcing on RIS integrity is thus inferred from the association of the spatial and temporal distribution of strong icequakes with the seasonal variation of the gravity wave impacts.

4.2 Transfer Function: from A_G to A_{SV}

Dynamic pressure from low-frequency (<0.04 Hz) surface gravity waves decays relatively slowly with depth, with significant signal reaching the seafloor at KPDR (741 m) near the RIS front. Long-period gravity waves also excite high-amplitude A_{SV} at nearby on-ice station DR01 (Figure 4.1b). Episodic strong IG arrivals are observed at both KPDR and DR01, spanning the 0.003–0.02 Hz band. They result primarily from the non-linear transformation of long-period swell in shallow water [Herbers, Elgar, and Guza 1995] along the Pacific coasts of North, Central, and South America. IG events are associated with heightened levels in the VLP band, particularly during the austral winter from late March to early October. IG and VLP waves are minimally attenuated by sea ice in winter [Bromirski, Sergienko, and MacAyeal 2010; Bromirski et al. 2017].

In contrast, swell is significantly attenuated by sea ice. When sea ice is minimal (mid-January to mid-March), the DR01 response shows that swell excites high-amplitude A_{SV} (Figure 4.1b). The response to swell is much smaller during the winter, when sea ice damps swell energy above 0.04 Hz. Due to the frequency-dependent dynamic pressure decay with depth, gravity wave signals are only detected at KPDR below 0.04 Hz, above which the dynamic pressure is not above the background noise, making the A_G estimation unreliable. Therefore, the transfer function estimation is focused on VLP, IG, and low-frequency swell (0.03–0.04 Hz) bands.

As mentioned above, VLP and IG arrivals observed at KPDR and DR01 coincide, yielding good correlation between incident gravity waves and icefront vibrations. Specifically, the yearly correlation coefficient between A_G and A_{SV}, or R_{GSV}, is 0.938 in the combined VLP and IG band (Figure 4.1c). Similarly, the correlation is also good for low-frequency swell (R_{GSV}=0.916, 0.03–0.04 Hz), implying that it is not strongly attenuated by sea ice. The high correlations between A_G and A_{SV} suggests that a reliable estimate of the empirical A_G to A_{SV} transfer function can be determined, providing an important observation-based estimate of the gravity-wave/ice-shelf interaction.

The frequency-dependent empirical transfer function $T_{GSV}(f)$ of A_G to A_{SV} was determined for yearly, summer, and winter periods following the methodology in Section 4.7.1. The yearly average transfer function (Figure 1d, black curve) is approximately constant (0.6–0.7) in the 0.001–0.01 Hz band, covering the VLP band and part of the IG band. The transfer function decreases dramatically above 0.01 Hz, likely due to (1) the bottom pressure noise from non-gravity-wave sources results in over-estimation of A_G at higher frequencies, which reduces the transfer function, (2) less energy reaches the ice shelf cavity to force higher-amplitude ice shelf flexural vibrations, indicated by the plate wave observations on the RIS [Chen et al. 2018], and/or (3) a significant portion of higher-frequency incident swell is reflected during summer. T_{GSV} during summer (Jan 17–Mar 15, 2015), winter (Jul 1–Sep 1, 2015), and the whole year (Jan 17–Dec 8, 2015) shows little seasonal variation below 0.04 Hz, indicating that sea ice sea

ice doesn't significantly damp swell at these frequencies. In addition to providing a physical relation between gravity wave impacts and ice shelf response that supports our discussion on the association of icequakes and the gravity waves, the transfer function can potentially be used to estimate the ice shelf response with marine measurements in the future, which is valuable for ice shelf stability analysis.

4.3 A_G and A_{SV} in the VLP, IG, and Swell Band

With $T_{GSV}(f)$ determined, we further scrutinize and compare A_G (Figure 4.2a) and A_{SV} (Figure 4.2b) in the VLP, IG, and swell bands, with major earthquakes and other strong transient signals removed. Characteristic tsunami and strong IG are observed, as well as seasonal variation of wave activity. Their potential association with ice fracturing is discussed.

The VLP-band A_G and A_{SV} are higher in winter than in summer. Average VLP-band A_G is twice as large in winter ($\sim$2 mm) compared with summer ($<$1 mm), reflecting strong storm activity over the Southern Ocean in winter. Similarly, as $T_{GSV}(f)$ indicates, average VLP-band A_{SV} in winter ($\sim$1 mm) is about twice that during summer ($\sim$0.5 mm). The highest VLP-band A_G (7 mm) and A_{SV} (4 mm) in 2015 are observed on September 17–18, resulting from tsunami arrivals generated by the Mw 8.3 Chilean earthquake on September 16. The tsunami excited flexural-gravity waves propagating southward across the RIS, recorded by the on-ice seismic array [Bromirski et al. 2017].

Though the background IG-band A_G ($\sim$2 mm) and A_{SV} ($\sim$1 mm) do not vary significantly with season, there are more strong IG arrivals in winter. The highest IG-band A_G in 2015 (7 mm) is observed in early May, during which high A_{SV} (2.7 mm) and cross-ice-shelf flexural-gravity waves were also observed [Bromirski et al. 2017], compared with the highest IG-band A_{SV} (3.3 mm) observed during the mid-September tsunami.

A_G was estimated for the low-frequency swell band, while A_{SV} is estimated for both the

low-frequency swell band and full swell band (Figure 4.2). Unlike VLP, IG, and low-frequency swell, high-frequency swell (0.04–0.1 Hz) is readily attenuated by sea ice. Consequently, A_{SV} is significantly higher in summer (2–8 mm) than in winter (1–4 mm, except for an 8-mm event). As swell attenuation by sea ice is very effective above 0.04 Hz, this causes a strong seasonal variation of A_{SV} for the full swell band, with amplitudes sporadically above 0.5 mm, and up to 2.1 mm in summer versus 0.02–0.2 mm in winter. A_{SV} plummets in mid-March, when sea ice begins to form near the shelf front (Figure S4.1).

The VLP, IG, and low-frequency swell bands are combined (0.001–0.04 Hz) to investigate the full RIS response. A_G is slightly higher in summer than in winter, primarily due to less sea ice attenuation of swell near 0.04 Hz. In contrast, A_{SV} is higher in winter when more VLP and IG energy is produced by heightened storm activity.

4.4 Icequakes

The impact of gravity wave excitation on the RIS integrity can be assessed in part by the temporal and spatial distribution of wave-induced icequake activity. Icequakes can be classified by seismic source processes. Rift icequakes are associated with crevasse extension and formation, which occupy the 5–50 Hz band for the Amery Ice Shelf [Bassis et al. 2007]. Basal shear icequakes are associated with basal sliding over bedrock, causing stick-slip events. They are observed at longer periods, e.g. 20–150 s at the Whillans Ice Plain [Wiens et al. 2008]. Basal non-shear seismicity have been rarely observed and are primarily hydrofracture-related [Podolskiy and Walter 2016]. Iceberg calving generates high-frequency seismicity (primarily 1–5 Hz), which may be observed tens or hundreds of kilometers away [O'Neel et al. 2010].

Here we focus on the seismicity in the 1–8 Hz band, which is the dominant band of icequakes observed at the ice shelf front and at non-icefront stations. Icequakes are detected using STA/LTA methodology [Withers et al. 1998], removing spurious transients and teleseismic

signals (Section 4.7.2). For spectral and statistical analysis, the 250 highest (waveform envelope) amplitude icequakes over the two-year deployment were identified at each station. Their distributions are shown in Figure 4.4e, which show two classes of icequakes based on amplitude, those near the shelf front and those interior RIS. Although icequake signals at DR14 are the strongest among non-icefront icequakes, they are typically one to two orders of magnitude lower than icefront events.

The top 20 icequake signals at DR14 were located to be near the rift tip (Figure 4.1a, Section 4.7.3 gives the location methodology). Though most icequakes near DR14 are observed at multiple stations, only a few icefront icequakes with clear arrivals were detected at multiple stations to allow location (Figure 4.1a). This is primarily due to station proximity. The locatable icequakes at DR01 (four), DR02 (one), and DR03 (eight) occur near the icefront, potentially due to a different source mechanism than the rift icequakes near DR14. The rift icequakes cannot be observed more than 60 km away (from near DR14 to DR05), while some icefront icequakes are detectable 160 km away (from near DR01 to DR14) as a consequence of their higher amplitudes.

To further investigate the rift and icefront icequakes, we analyzed icequakes near DR14 and DR01 each in a subsection. Since most locatable rift icequakes occurred closest to DR14, icequake signals at DR14 are used for rift icequake analysis. Though all icefront stations have locatable icequake observations, an OBS station (KPDR) near DR01 (Figure 4.1a) provided seafloor observations for comparison with icequake signals at DR01. Rift and icefront icequakes were characterized based on their 0.1–20 Hz spectral content and their corresponding background noise spectra (Figure 4.3). Moreover, their propagation and particle motion characteristics are discussed for two representative icequakes, which have clear arrivals and propagate at about the average speed of all located icequakes of their type. To identify seismic phases, we compared the observed travel speeds with those indicated by the synthetic seismograms on the ice shelf surface (Figure S4.2). By setting P and S wave speeds as 3.772 km/s and 1.875 km/s [Diez et al. 2016] in the model, the extensional and flexural Lamb wave speeds are 3.0 and 1.5 km/s respectively.

These two types of plate waves are also observed at lower frequencies [Chen et al. 2018].

4.4.1 Rift Icequakes

At DR14, the summer (Jan 15–Mar 15, 2015) and the winter (Jul 1–Sep 1, 2015) background vertical displacement spectral levels are similar, with summer $<$10 dB higher in the 0.4–2 Hz band (Figure 4.3a), suggesting that the seasonal variation of the ocean wave impacts and local environment (e.g. temperature, wind, ice flow) do not strongly affect the background noise levels. The 1–10 Hz median icequake spectrum is about 20–30 dB above the background.

The representative rift icequake is located on the rift north of DR14, located with high confidence (Figure 4.3c). Two major phases are observed on projections on the vertical-radial plane. The first phase travels at 3.0 km/s (Figure 4.3e,g) and is strongest on the radial component, suggesting extensional Lamb wave generated by a source with a considerable horizontal forcing (Figure S4.2). The second phase travels at 1.5 km/s and is observed on both vertical and horizontal components with elliptical polarization, suggesting flexural Lamb wave (Figure S4.2).

4.4.2 Icefront Icequakes

At DR01, the median winter background spectrum is similar to DR14, while the summer background spectrum is 20–30 dB higher than winter (Figure 4.3b), suggesting that icefront background noise results primarily from seasonal variations in sea ice attenuation of ocean wave energy and/or temperature. The median icequake spectrum is 10–20 dB higher than the summer background spectrum over most of the 0.1–20 Hz band.

The representative icefront icequake is located near DR01 at the icefront, with the 95% confidence interval covering part of the icefront (Figure 4.3d). Two major phases are observed on projections on the vertical-radial plane, traveling at 6.1 km/s and 3.5 km/s (Figure 4.3f,h). Since the first phase travels much faster than ice P-waves, a portion of its propagation path must be

through the crust. The second phase travels close to ice P-wave speed, but has comparable vertical and radial components, different from the radial-dominant extensional Lamb waves observed for the rift icequake. It is likely the extensional Lamb waves generated by a source with primarily vertical forcing. Alternatively, it might travel through the lithified sediments on the seafloor [P-wave speed 3.75 km/s Peters et al. 2008]. The icequake is also observed at KPDR, traveling at 1.6 km/s (near 1.5 km/s water wave speed) over the estimated 9 km epicentral distance. Similar icefront icequakes likely results from either iceberg calving, intra-shelf fracturing, or possibly basal crevasse expansion near the icefront. Icequake observations at DR01 and KPDR show such evens are quite common. Among the 50 strongest icequake signals during the time period when both DR01 and KPDR are deployed, 23 icequakes were clearly detected at both stations, including the two locatable events in 2015. On-ice and seafloor hydrophone arrays near the ice edge would be needed to understand these potentially important icefront icequakes.

4.5 Discussion

Rift and icefront icequakes have different temporal distributions, resulting from being associated with different portions of the gravity wave spectrum. Most icefront icequakes occur in summer and early fall. Among the 250 strongest icequake signals at DR01, DR02, and DR03, 236, 243, and 205 occurred from January to March respectively, the same period when sea ice is minimal and the swell-band icefront vibrations are strongest (Figure 4.4a,b,c and Figure S4.3). The rapid increase (January) and decrease (March) of the swell-band vibrations are accompanied by a rapid change in cryoseismicity (Figure S4.3), indicating the association of swell and ice fracturing at the shelf front. Sea ice efficiently attenuates swell and protects the ice shelf. The winter collapses of the Larsen and Wilkins ice shelves were preceded by increased seasonal sea ice loss, suggesting that swell may have contributed to triggering their disintegration [Massom et al. 2018]. However, the very rapid drop-off of swell excitation at the onset of the austral winter

(Figure 4.2) demonstrate the high sensitivity of swell >0.04 Hz to sea ice damping. Consequently, unless sea ice was nearly completely absent during the collapse events, it's questionable whether swell impacts initiated their collapse, suggesting that undamped heightened winter VLP excitation could have contributed.

Although there appears to be a clear association between swell forcing and icefront cryoseismicity, more icequakes do not occur during strong swell arrivals. Three icequake swarms occurred at DR01 in summer 2015 at DR01 and one at DR02 in 2016. There is no evidence that they are associated with strong swell arrivals. Additionally, fewer icequakes were observed in 2016 than in 2015 regardless of the swarms, although a strong El Niño occurred in early 2016, causing higher swells near RIS (Figure 4.4a–d, blue curves). At DR03, 149 strong icequakes were detected between 12/01/2014 and 09/01/2015, while only 100 icequakes occurred during the El Niño. This suggests that swell does not directly force ice fracturing, but instead contributes to fracture expansion and fatigue weakening by persistently impacting the ice shelf.

In contrast to icefront icequakes, no strong seasonal variation of rift seismicity is observed. Slightly more rift icequakes occurred in winter and early spring, the same period when VLP is strongest. Among the 250 strongest icequake signals at DR14, on average, about 14 occurred per month from June to September (Figure 4.4d) versus 9 in other months. But due to such low seasonal variation, the relation between rift icequakes and VLP impacts is still questionable. As persistent waves with little sea ice attenuation, VLP may also contribute to ice shelf fatigue weakening and facilitate icequakes indirectly. Additionally, rift icequakes have been related to thermal tidally-driven stresses [Olinger et al. 2018], indicating that multiple factors are involved.

The spatial distribution of strong icequake detections across the RIS is influenced by the array configuration and station positions (Figure 4.1a). Icefront stations (all located 2 km from the ice edge) show amplitude variability (Figure 4.4e) that must be associated with gravity wave variability along the front and/or variable ice integrity. Near-rift amplitudes generally decrease with distance from the rift near DR14. At stations away from the rift or front (RS03, DR05, DR06,

DR11), strong icequake detections are far fewer and with lower amplitude, indicating that there are regions of the RIS that exhibit relatively low seismicity, even in passive ice regions [Fürst et al. 2016] where ice velocity is high [Rignot, Mouginot, and Scheuchl 2011].

4.6 Conclusions

Ice shelves restrain ice discharge to the sea. Their integrity may deteriorate due to several factors, including the ocean gravity wave impacts. Gravity wave amplitudes, A_G, were estimated from seafloor pressure data near the RIS front. Together with on-ice vertical seismic displacement amplitudes, A_{SV}, at a near-front seismic station, the transfer function, T_{GSV}, from A_G to A_{SV} was shown to be nearly constant below 0.01 Hz with a rapid decrease at higher frequencies. Analysis on the high-frequency swell band (>0.04 Hz) is limited by unreliable A_G estimation due to poor signal-to-noise. Based on the source locations, spectra, and travel speeds, two types of icequakes were observed on the RIS, rift icequakes and icefront icequakes, both exhibiting two major phases. Rift icequakes mainly occurred along a rift about 150 km from the icefront, primarily spanning the 1–10 Hz band. These icequake signals propagate in the ice, with the phases traveling at 3.0 km/s and 1.5 km/s. Their occurrences do not show a significant correlation with gravity wave events, suggesting that fracture expansion and associated weakening from persistent wave excitation may be important factors that precondition the ice for fracturing under moderate ocean-driven stresses. Icefront icequakes span a wider frequency band, down to 0.1 Hz or lower, with phases traveling at higher speeds, indicating travel paths through the crust (6.1 km/s) and though the ice or lithified sediments (3.5 km/s). These may result from iceberg calving, intra-shelf fracturing, or basal crevasse expansion. The seismicity has a strong seasonal concentration, with most occurring during the austral summer when sea ice is absent. Closely-spaced on-ice and seafloor hydrophone arrays near the ice edge are needed to understand these potentially important fracture events.

Acknowledgements

Bromirski, Gerstoft, and Chen were supported by NSF grant PLR 1246151. Bromirski also received support from NSF OPP 1744856 and CAL DPR C1670002. Stephen was supported by NSF grant PLR-1246416. Wiens, Aster, and Nyblade were supported under NSF grants PLR-1142518, 1141916, and 1142126, respectively. Seismic instruments and on-ice installation support were provided by the Incorporated Research Institutions for Seismology (IRIS) through the PASSCAL Instrument Center at New Mexico Tech. The RIS and KPDR seismic data are archived at the IRIS Data Management Center, http://ds.iris.edu/ds/nodes/dmc/, with network code XH and KP, respectively. The facilities of the IRIS Consortium are supported by the National Science Foundation under Cooperative Agreement EAR-1261681 and the DOE National Nuclear Security Administration. We thank Patrick Shore, Michael Baker, Cai Chen, Robert Anthony, Reinhard Flick, Jerry Wanetick, Weisen Shen, Tsitsi Madziwa Nussinov and Laura Stevens for their help with field operations. Logistical support from the U.S. Antarctica Program in McMurdo was critical, and is much appreciated.

Remark

Chapter 4, in full, has been submitted for publication as Chen, Z., Bromirski, P.D., Gerstoft, P., Stephen, R.A., Lee, W.S., Yun, S., Olinger, S.D., Aster, R.C., Wiens, D.A., and Nyblade, A.A., 2019, “Ross Ice Shelf Icequakes Associated with Ocean Gravity Wave Activity", *Geophysical Research Letters.* The dissertation author was the primary investigator and author of the paper.

Figures

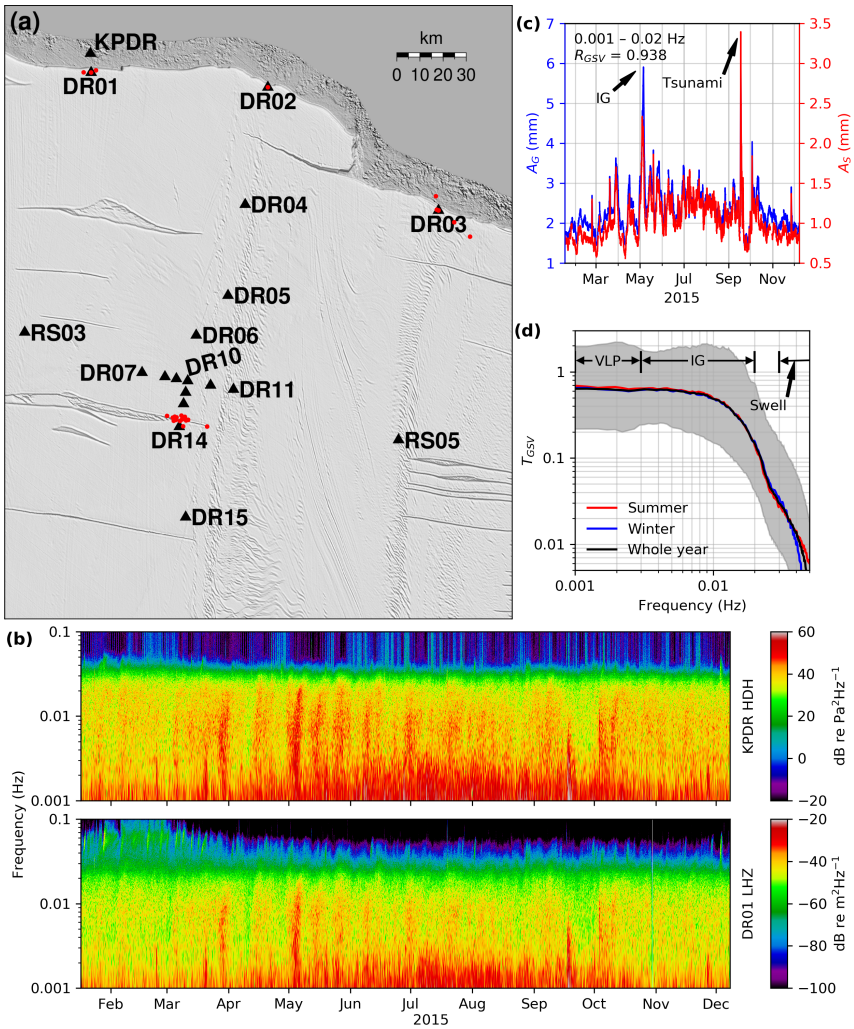

Figure 4.1: (a) The on-ice broadband seismic array and the OBS off the ice shelf front (triangles), with morphology as background [Haran et al. 2014; Scambos et al. 2007] and located icequakes (red dots). (b) Spectrograms of the ocean bottom pressure at KPDR (top) and vertical displacement at DR01 (bottom). The sampling rate of the seismic data is 1 Hz. (c) Combined VLP and IG band (0.001–0.02 Hz) A_G (blue) near the RIS front, estimated from the OBS (b, top), in comparison with A_{SV} (red) at the RIS front, estimated from the vertical seismic displacement spectrogram at DR01 (b bottom). Both were smoothed with a 12-h median filter. Major earthquakes and other strong transients were removed. The strong IG event in May and the tsunami in September are annotated. (d) Frequency-dependent transfer function for the ocean-wave height to the vertical displacement of the ice shelf front in summer (Jan 17–Mar 15, 2015, red), winter (Jul 1–Sep 1, 2015, blue), and whole year (Jan 17–Dec 8, 2015, black). The gray area indicates the range of the A_SV/A_G ratio of the time segments that were used for transfer function estimation.

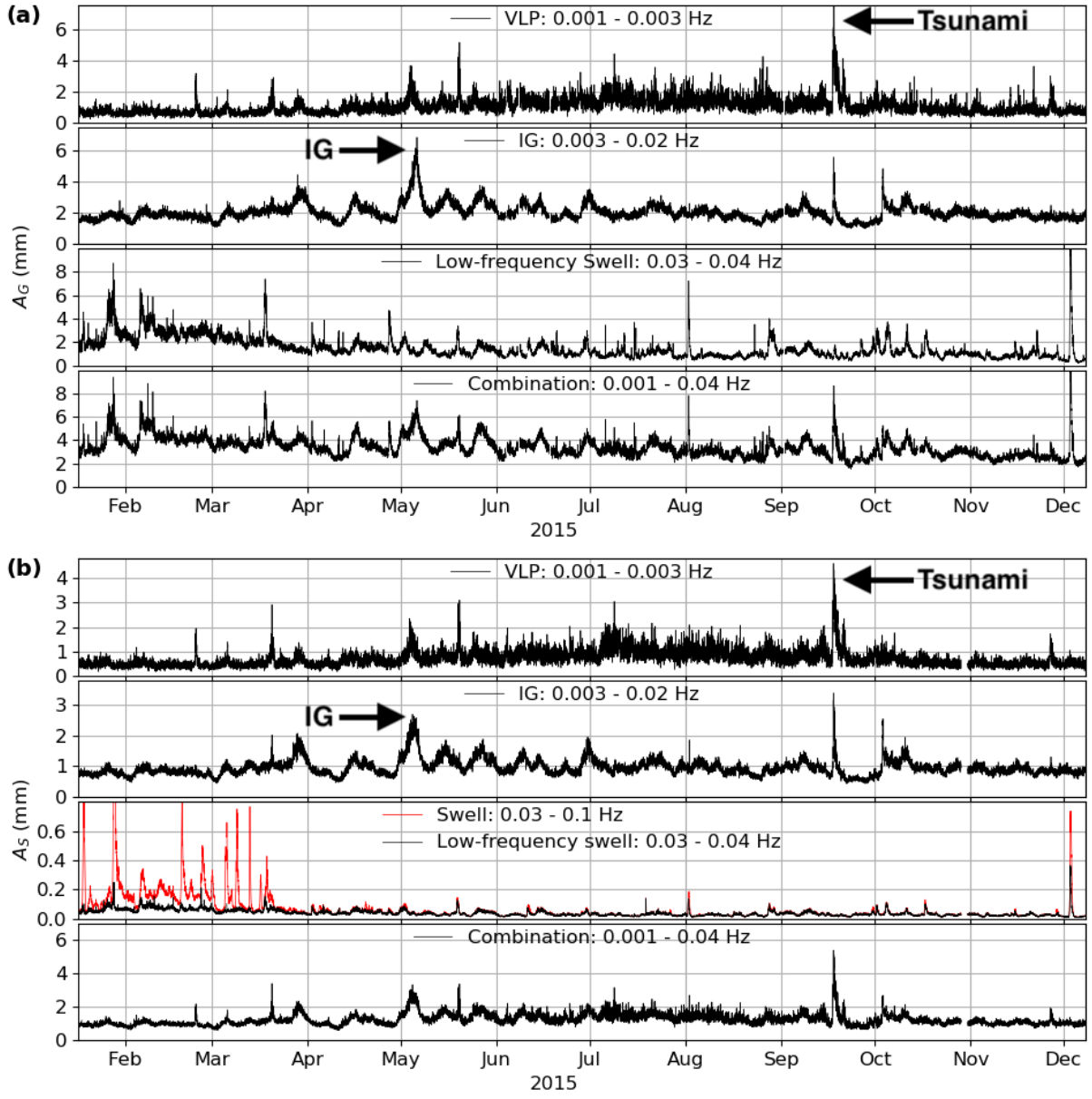

Figure 4.2: (a) A_G at KPDR estimated from the bottom pressure spectrogram, Figure 4.1b. The clipped amplitudes in early December are 13.2 and 13.5 mm for the 0.03–0.04 and 0.001–0.04-Hz bands. (b) A_{SV} at DR01. The amplitude of the two clipped 0.03–0.1-Hz peaks in January are 0.9 and 2.1 mm.

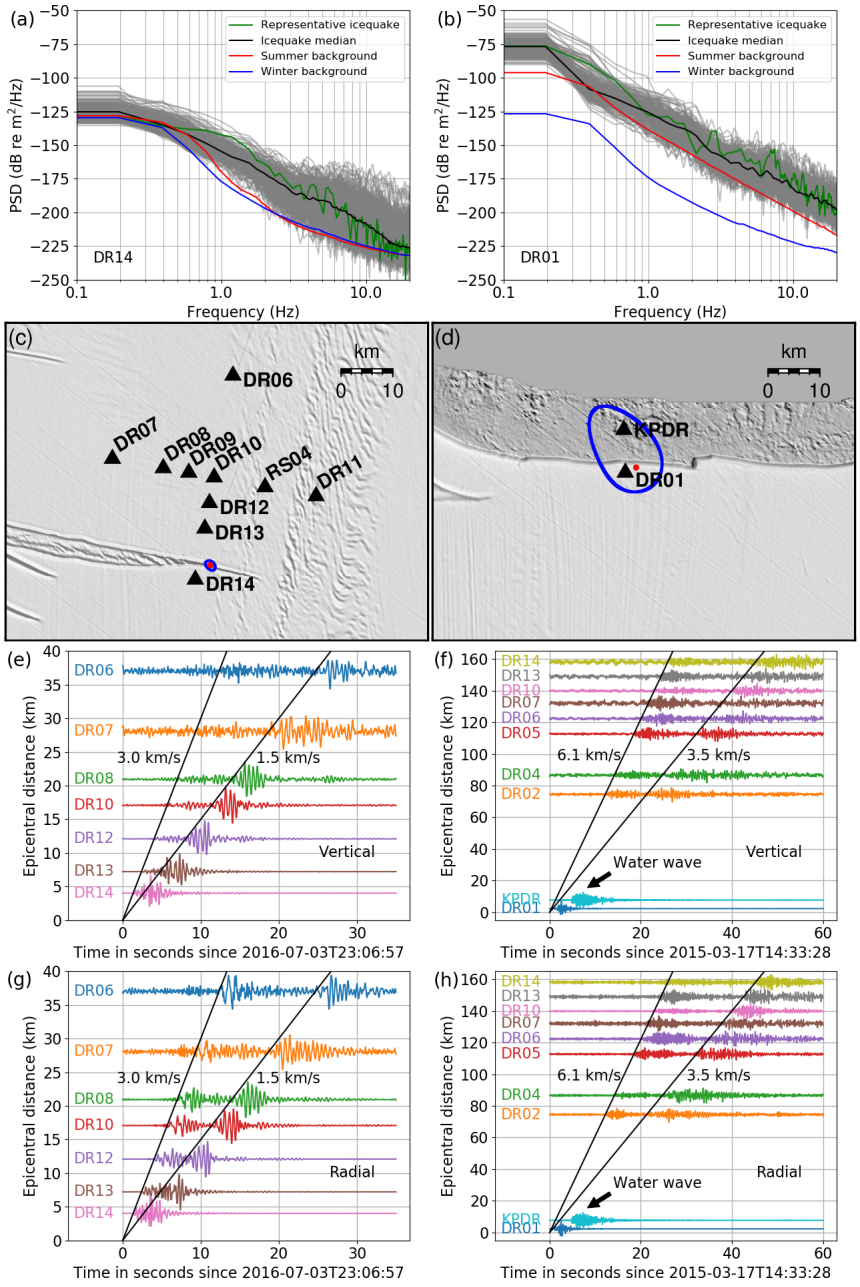

Figure 4.3: DR14 (a) and DR01 (b) spectra of the vertical displacements of the 250 strongest icequake signals (gray) with median (black) and representative icequake (green) spectrum, as well as summer (Jan 15–Mar 15, 2015, red) and winter (Jul 1–Sep 1, 2015, blue) background noise spectra. Near-DR14 (c) and near-DR01 (d) map of the stations (black triangle) and representative icequake (red dot) with 95% confidence intervel (blue), morphology as background [Haran et al. 2014; Scambos et al. 2007]. The icequakes were located with the phase traveling at 3.0 km/s (c, DR14) and 6.1 km/s (d, DR01). Vertical (e) and radial (g) displacement moveout of representative icequake near DR14, 2–8 Hz bandpassed and normalized to its maximum amplitude. (f, h) Same as (e, g) but for DR01. KPDR pressure response is included.

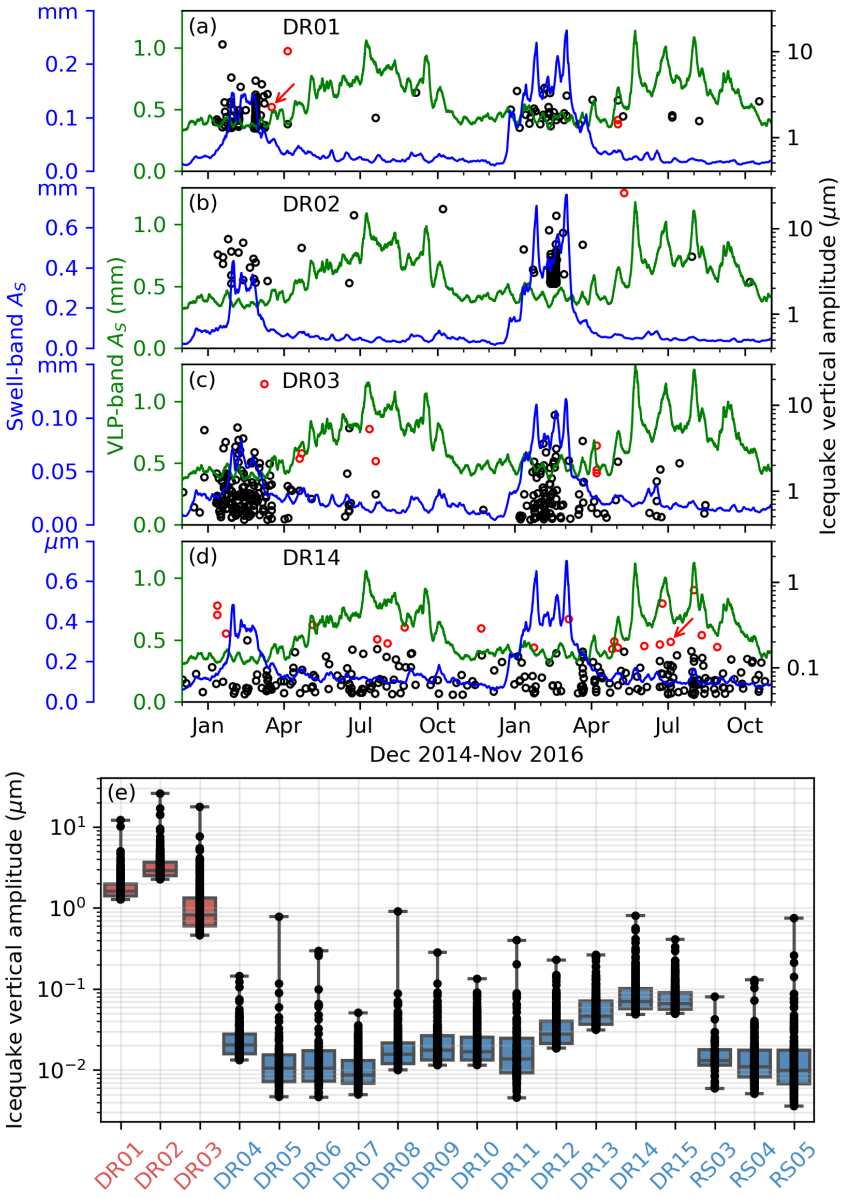

Figure 4.4: DR01 (a), DR02 (b), DR03 (c), and DR14 (d) weekly medians of A_{SV} in the VLP band (0.001–0.003 Hz, green curve) and swell band (0.03–0.1 Hz, blue curve), with the temporal distribution of the 250 strongest icequake signals (red circles: located in Figure 4.1a; black circles: unlocated) from Dec 1, 2014 to Nov 1, 2016. The representative icequakes near DR01 and DR14 in Figure 4.3 are indicated by arrows in (a) and (d). The swell-band A_{SV} units are mm for DR01, DR02, and DR03, but is μm for DR14. (e) Vertical amplitude distribution of the strongest 250 (or fewer) icequake signals (dots) at each station in Figure 4.1a (zoom-in map in Figure 4.3c). The box and the band inside indicate the three quartiles. Fewer than 250 icequakes were detected at DR05 (80), DR06 (83), DR11 (106), RS03 (41), RS04 (214), RS05 (203).

4.7 Appendix

4.7.1 Gravity Wave Amplitude, Seismic Wave Amplitude, and Transfer Function Estimation

For a gravity wave train propagating on a free surface along the horizontal x axis with amplitude a, wavenumber k, and angular frequency ω, the time-dependent dynamic pressure at depth z is

$$p(z) = \rho g a \frac{\cosh(k(z+H))}{\cosh(kH)} \cos(kx - \omega t), \tag{4.1}$$

where ρ is water density (1025 kg/m^3), g is gravitational acceleration (9.8 m/s^2), H is total water depth (741 m for KPDR) [Kundu, Cohen, and Dowling 2011, Equation 7.31]. Hence, the bottom dynamic pressure $p_{BDP} = p(z = -H)$ can be represented by the product of the surface dynamic pressure $p_{SDP} = p(z = 0)$ and the frequency-dependent surface-to-bottom dynamic pressure decay factor $\alpha(f)$

$$p_{BDP} = \alpha(f) p_{SDP}, \tag{4.2}$$

where

$$\alpha(f) = \cosh^{-1}(kH). \tag{4.3}$$

By solving the gravity wave dispersion relation [Kundu, Cohen, and Dowling 2011, Equation 7.29]

$$c = \frac{\omega}{k} = \sqrt{\frac{g}{k} \tanh(kH)}, \tag{4.4}$$

the wavenumber k, and thereafter $\alpha(f)$, can be determined for each frequency. Let $S_{SDP}(f,t)$ be the surface dynamic pressure spectrogram, i.e. the spectrogram of p_{SDP}, and $S_{BDP}(f,t)$ be the bottom dynamic pressure spectrogram, i.e. the spectrogram of p_{BDP}. $S_{BDP}(f,t)$ is calculated with 4096-s long Hanning-windowed pressure data segments, overlapped 1024 s. The 100-Hz

sampled pressure data are lowpass filtered at 0.4 Hz and downsampled to 1 Hz for spectrogram calculation. According to Equation 4.2, $S_{SDP}(f,t)$ is estimated by

$$S_{SDP}(f,t) = \alpha^{-2}(f) S_{BDP}(f,t). \tag{4.5}$$

The gravity wave amplitude spectrogram $S_G(f,t)$ is then obtained by

$$S_G(f,t) = \frac{S_{SDP}(f,t)}{(\rho g)^2}. \tag{4.6}$$

Let $S_{SV}(f,t)$ be the vertical seismic displacement spectrogram. $S_{SV}(f,t)$ is calculated with the same parameters as for $S_{BDP}(f,t)$ except that 1-Hz sampled seismic data are directly available. The frequency-dependent transfer function, $T_{GSV}(f)$, is defined by

$$S_{SV}(f,t) = T_{GSV}(f) S_G(f,t) \tag{4.7}$$

and is estimated by minimizing

$$\| S_{SV}(f,t) - T_{GSV}(f) S_G(f,t) \|_2^2 \tag{4.8}$$

at each frequency f.

The time-dependent gravity wave amplitude $A_G(t)$ in frequency band $[f_1, f_2]$ is estimated by

$$A_G(t) = \sqrt{\int_{f_1}^{f_2} S_G(f,t) \mathrm{d}f} \tag{4.9}$$

Similarly, the time-dependent vertical seismic displacement amplitude $A_S(t)$ in frequency

band $[f_1, f_2]$ is estimated by

$$A_{SV}(t) = \sqrt{\int_{f_1}^{f_2} S_{SV}(f,t)\mathrm{d}f} \tag{4.10}$$

In real data processing, temporal segments with missing data, earthquakes, or significant instrument noise are discarded. Transfer function values are first calculated for each segment and then sorted. Segments giving transfer function values below 5 percentile level or above 95 percentile level are discarded in transfer function estimation. The summer, winter, and whole year estimation are based on 4633, 5132, and 26271 segments, respectively.

4.7.2 Icequake Detection

First, we use short-term-average/long-term-average (STA/LTA) methodology [Withers et al. 1998] to detect signals with high signal-to-noise-ratio (SNR). A STA/LTA ratio above a preselected “on-threshold" identifies a high-SNR signal. The detected signal is regarded as ended when the ratio drops below a preselected “off-threshold". This process is automated by ObsPy [Beyreuther et al. 2010], a Python package that we used in this study. The lengths of the short time window and the long time window are 3 and 60 seconds. The on and off thresholds are 10 and 1.

Second, we clean the detection results by removing the non-icequake signals. One kind of non-icequake signals has waveforms like a sequence of the same wavelet, often with much higher amplitudes than adjacent normal data. Another kind of non-icequake signal is an earthquake. We differentiate them from icequakes with an empirical method based on the following aspects. (1) Earthquake sources are mainly out of the RIS, while icequake sources are mainly within the RIS. (2) Earthquake signals propagate at a higher speed than icequakes. (3) Earthquakes are usually observed at most of the 34 RIS array stations, except that they can sometimes be overwhelmed by the strong background noise at the icefront. Icequakes (1–8 Hz) can hardly propagate more than 200 km, i.e. they can be observed at less than 20 stations, but typically 10 or less. Though

lower-frequency icequakes, like the stick-slip icequakes [Wiens et al. 2008], can propagate a longer distance, they are out of this paper's scope.

4.7.3 Icequake Location

Icequakes are located based on Chapter 5.7 of [Shearer 2009]. Icequakes are defined by their origin times t_0 and hypocenter locations, i.e. latitude θ, longitude ϕ, and depth h. For the RIS (hundreds of meters thick), the focal depth h is much less than the epicentral distance (tens of kilometers); therefore, h is neglected in the following. The seismic arrival time at the nth station is predicted by

$$t_n^p = F_n(t_0, \theta, \phi), \tag{4.11}$$

where F_n is a prediction operator that incorporates the Earth model parameters. For icequake signals traveling at uniform apparent speed c, F_n is simplified as

$$t_n^p = t_0 + \frac{d_n(\theta, \phi)}{c}, \tag{4.12}$$

where d_n denotes the epicentral distance of the nth station.

Let the model vector $\mathbf{m} = (t_0, \theta, \phi, c)^T$, where the superscript $(\cdot)^T$ denotes transpose. The cost function is defined as the sum of squared arrival time prediction errors at the N stations

$$\varepsilon(\mathbf{m}) = \sum_{n=1}^{N} [t_n - t_n^p(\mathbf{m})]^2, \tag{4.13}$$

where t_n is the observed arrival time at the nth station. Minimization of $\varepsilon(\mathbf{m})$ yields an estimate of the model vector $\mathbf{m}_{\text{best}}$. Since $d_n^p(\theta, \phi)$ is a non-linear function, the minimization is done by grid search.

For simplicity, assume the misfit $t_n - t_n^p(\mathbf{m})$ is caused by uncorrelated, random Gaussian

noise with standard deviation of σ, which can be estimated by the residuals at $\mathbf{m}_{\text{best}}$

$$\sigma^2(\mathbf{m}_{\text{best}}) = \frac{\sum_{n=1}^{N}[t_n - t_n^p(\mathbf{m}_{\text{best}})]^2}{n_{\text{df}}}, \tag{4.14}$$

where $n_{\text{df}} = N - 4$ is the degree of freedom since $\mathbf{m}$ has 4 components. Accordingly, the variable

$$\chi^2(\mathbf{m}) = \sum_{n=1}^{N} \frac{[t_n - t_n^p(\mathbf{m})]^2}{\sigma^2}, \tag{4.15}$$

follows χ^2 distribution with n_{df} degrees of freedom, from which the 95% confidence limits can be obtained.

This is a basic method to get a first estimation of the icequake locations. Waveform cross-correlation methods could be applied to improve relative locations.

Table S4.1: Elastic parameters of air, ice [Diez et al. 2016], and water that are used in generating the synthetic seismograms on the ice shelf surface (Figure S4.2).

Layer	c_P (km/s)	c_S (km/s)	Density (kg/m^3)
Air	0.340	0	1.225
Ice	3.772	1.875	916
Water	1.500	0	1024

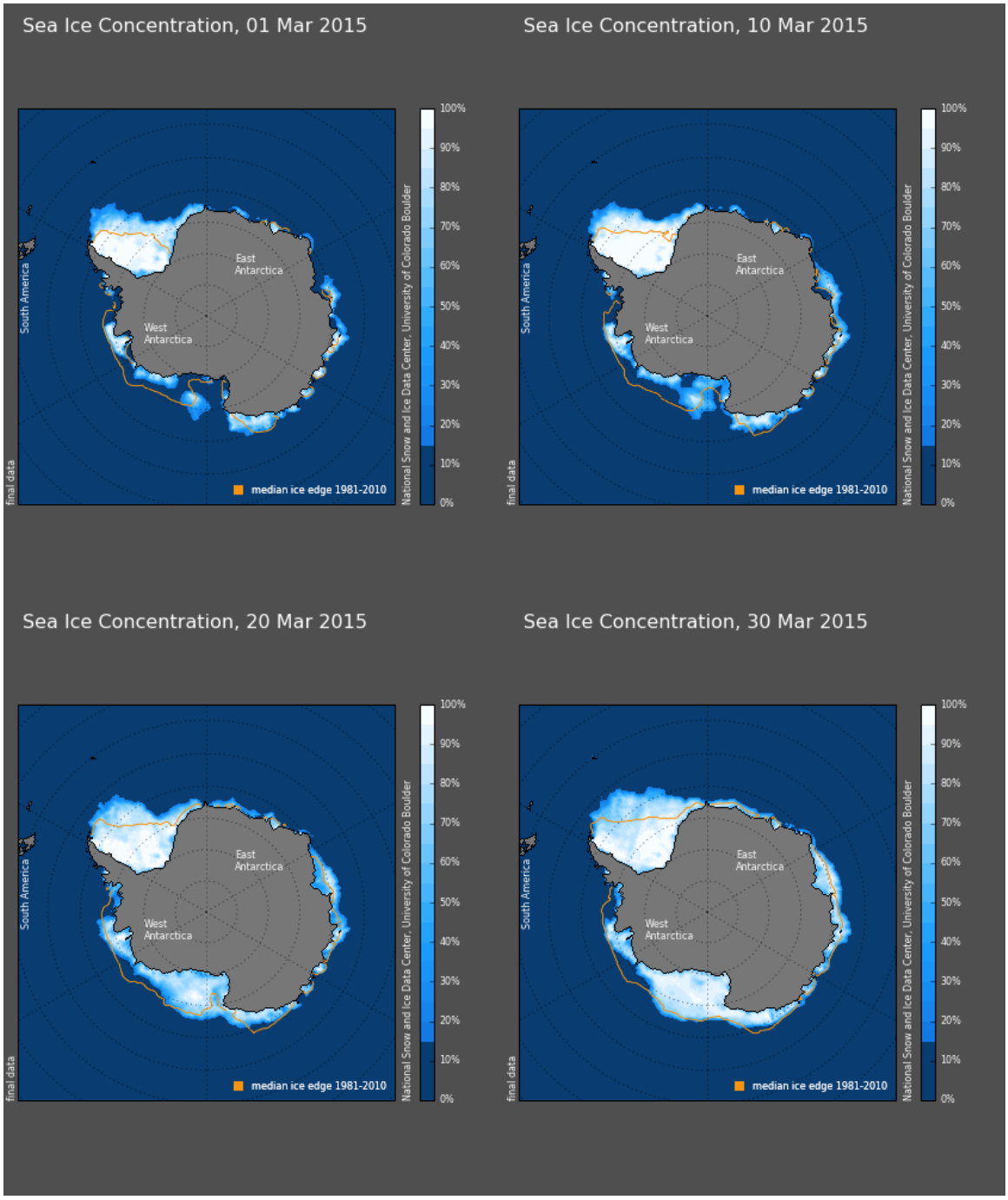

Figure S4.1: Sea ice concentration on Mar (a) 01, (b) 10, (c) 20, and (d)30 in 2015. Imagery from NASA Nimbus-7 SMMR and DMSP SSM/I-SSMIS Passive Microwave Data [Cavalieri et al. 1996 to present, updated yearly], courtesy NASA NSIDC DAAC.

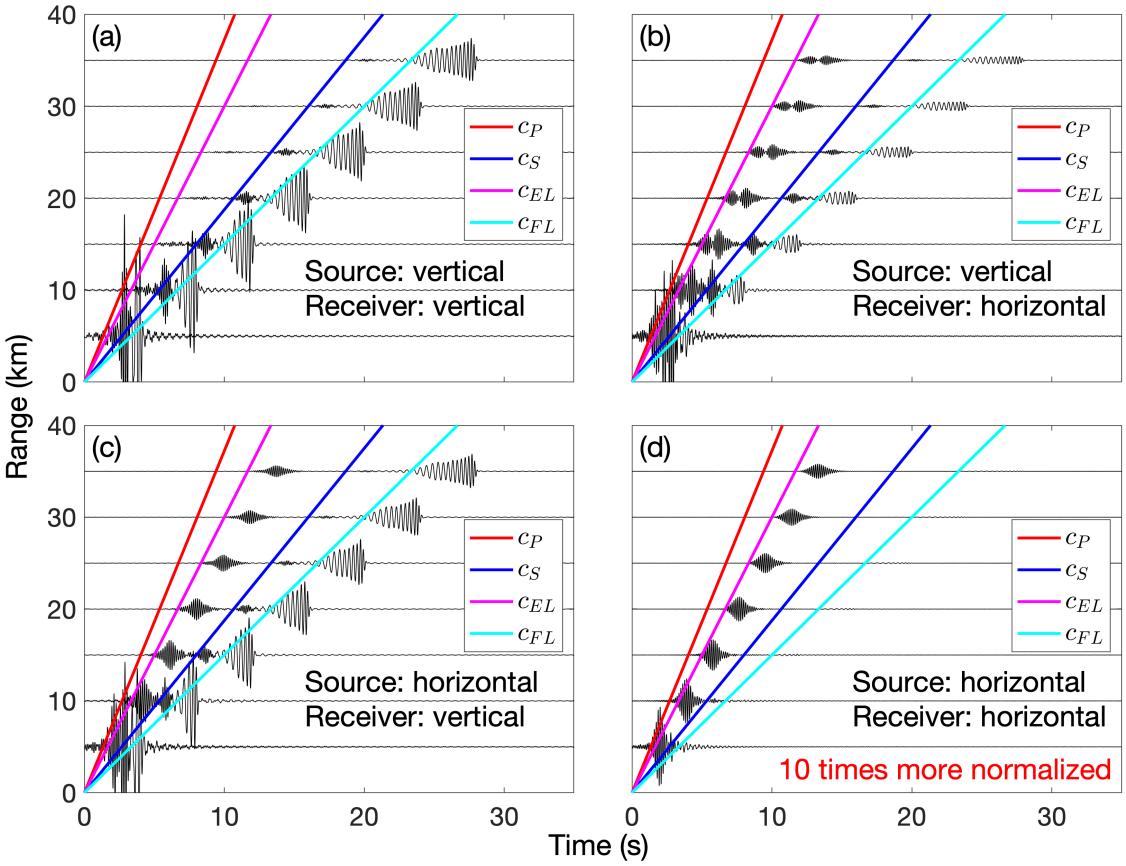

Figure S4.2: Synthetic seismograms on the ice shelf surface in a three layer model composed of air (half space), ice (300 m thick), and water (half space), with elastic parameters given in Table S4.1. They are generated with OASES, a software for modeling seismo-acoustic propagation in horizontally stratified waveguides [Schmidt and Jensen 1985]. The source is 10 m above the ice shelf bottom with a Ricker wavelet source function centered at 5 Hz. The source direction and receiver component are annotated. The speeds of P-wave (c_P=3.772 km/s, red), S-wave (c_S=1.875 km/s, blue), extensional Lamb wave (c_{EL}=3.0 km/s, magenta), and flexural Lamb wave (c_{FL}=1.5 km/s, cyan) in the ice shelf are indicated. The seismic traces are normalized with the same factor in (a), (b), and (c) and are 10 times more normalized in (d).

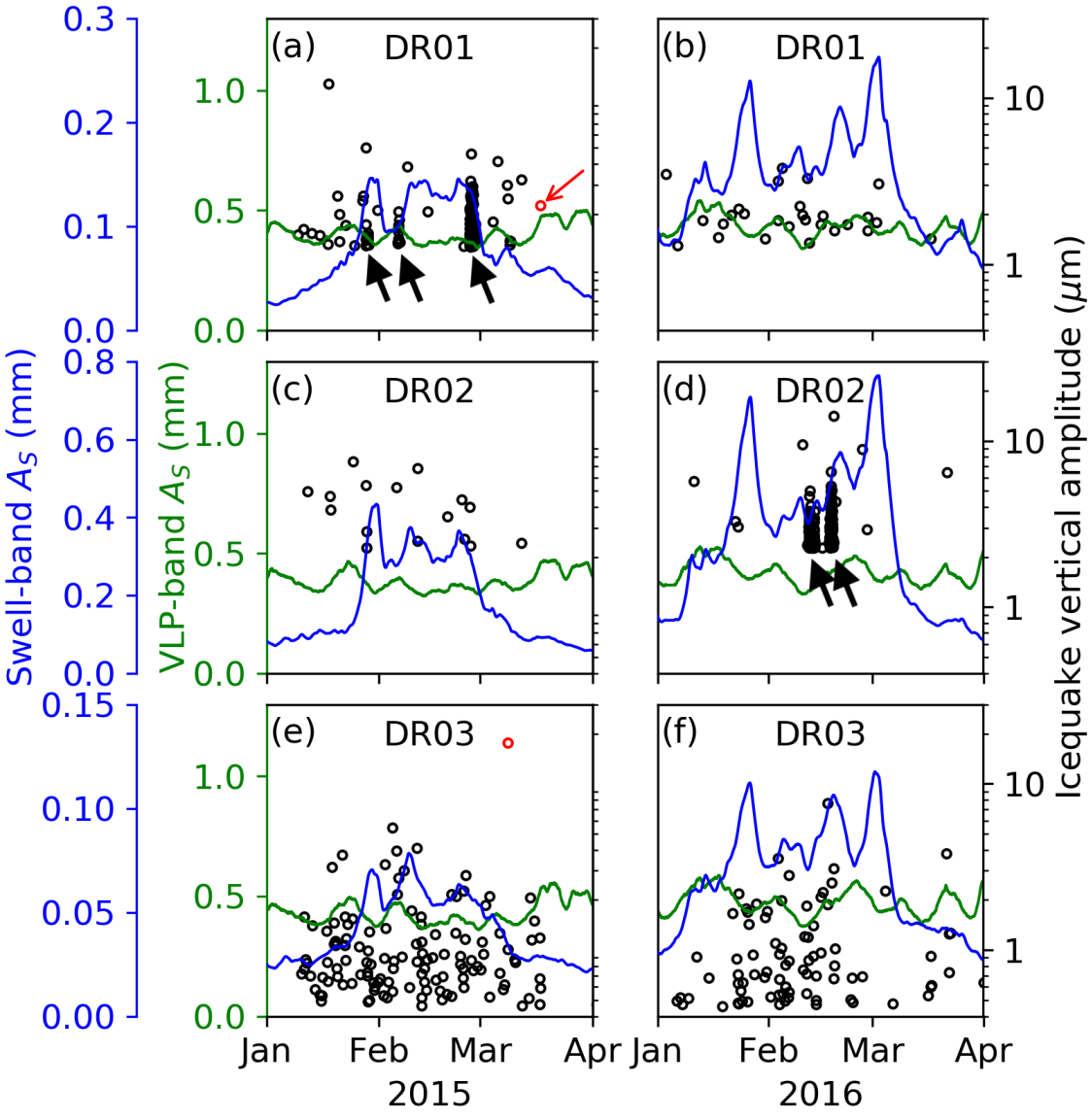

Figure S4.3: Zoom-in plot of austral summer activity from Figure 4.4. Weekly medians of A_{SV} in the VLP band (0.001–0.003 Hz, green curve) and swell band (0.03–0.1 Hz, blue curve) from Jan 1 to Apr 1, 2015. Icequakes that could be located are indicated by red circles, with positions shown in Figure 4.1a. (b, d, f) Same as (a, c, e) but for A_{SV} a year later. The three swarms at DR01 (a) and the two swarms at DR02 (d) are indicated by black arrows. The representative icequake near DR01 (shown in Figure3d) is indicated by the red arrow in (a).

References

Bassis, J. N., Fricker, H. A., Coleman, R., Bock, Y., Behrens, J., Darnell, D., Okal, M., and Minster, J.-B. (2007). "Seismicity and deformation associated with ice-shelf rift propagation". In: *Journal of Glaciology* 53.183, pp. 523–536. DOI: 10.3189/002214307784409207.

Bassis, J. N., Fricker, H. A., Coleman, R., and Minster, J.-B. (2008). "An investigation into the forces that drive ice-shelf rift propagation on the Amery Ice Shelf, East Antarctica". In: *Journal of Glaciology* 54.184, pp. 17–27. DOI: 10.3189/002214308784409116.

Benn, D. and Evans, D. (2010). *Glaciers and Glaciation*. Hodder Education, pp. 135–136. ISBN: 9780340905791.

Beyreuther, M., Barsch, R., Krischer, L., Megies, T., Behr, Y., and Wassermann, J. (2010). "ObsPy: A Python Toolbox for Seismology". In: *Seismological Research Letters* 81.3, p. 530. DOI: 10.1785/gssrl.81.3.530.

Bromirski, P. D., Chen, Z., Stephen, R. A., Gerstoft, P., Arcas, D., Diez, A., Aster, R. C., Wiens, D. A., and Nyblade, A. (2017). "Tsunami and infragravity waves impacting Antarctic ice shelves". In: *Journal of Geophysical Research: Oceans* 122.7, pp. 5786–5801. DOI: 10.1002/2017JC012913.

Bromirski, P. D., Diez, A., Gerstoft, P., Stephen, R. A., Bolmer, T., Wiens, D. A., Aster, R. C., and Nyblade, A. (2015). "Ross ice shelf vibrations". In: *Geophysical Research Letters* 42.18, pp. 7589–7597. DOI: 10.1002/2015GL065284.

Bromirski, P. D., Sergienko, O. V., and MacAyeal, D. R. (2010). "Transoceanic infragravity waves impacting Antarctic ice shelves". In: *Geophysical Research Letters* 37.2. DOI: 10.1029/2009GL041488.

Brunt, K. M., Okal, E. A., and MacAyeal, D. R. (2011). "Antarctic ice-shelf calving triggered by the Honshu (Japan) earthquake and tsunami, March 2011". In: *Journal of Glaciology* 57.205, pp. 785–788. DOI: 10.3189/002214311798043681.

Cavalieri, D. J., Parkinson, C. L., Gloersen, P., and Zwally, H. J. (1996 to present, updated yearly). *Sea Ice Concentrations from Nimbus-7 SMMR and DMSP SSM/I-SSMIS Passive Microwave Data, Version 1. (Subset: Mar 2015).* Boulder, Colorado USA. NASA National Snow and Ice Data Center Distributed Active Archive Center. Accessed: 2019-02-04. DOI: 10.5067/8GQ8LZQVL0VL.

Chen, Z., Bromirski, P. D., Gerstoft, P., Stephen, R. A., Wiens, D. A., Aster, R. C., and Nyblade, A. A. (2018). "Ocean-excited plate waves in the Ross and Pine Island Glacier ice shelves". In: *Journal of Glaciology* 64.247, pp. 730–744. DOI: 10.1017/jog.2018.66.

Diez, A., Bromirski, P., Gerstoft, P., Stephen, R., Anthony, R., Aster, R., Cai, C., Nyblade, A., and Wiens, D. (2016). "Ice shelf structure derived from dispersion curve analysis of ambient

seismic noise, Ross Ice Shelf, Antarctica". In: *Geophysical Journal International* 205.2, p. 785. DOI: 10.1093/gji/ggw036.

Fürst, J. J., Durand, G., Gillet-Chaulet, F., Tavard, L., Rankl, M., Braun, M., and Gagliardini, O. (2016). "The safety band of Antarctic ice shelves". In: *Nature Climate Change* 6, pp. 479–482. DOI: 10.1038/nclimate2912.

Haran, T., Bohlander, J., Scambos, T., Painter, T., and Fahnestock, M. (2014). "MODIS Mosaic of Antarctica 2008–2009 (MOA2009) image map". In: *Boulder, Colorado USA, National Snow and Ice Data Center* 10, N5KP8037.

Herbers, T. H. C., Elgar, S., and Guza, R. T. (1995). "Generation and propagation of infragravity waves". In: *Journal of Geophysical Research: Oceans* 100.C12, pp. 24863–24872. DOI: 10.1029/95JC02680.

Kundu, P. K., Cohen, I. M., and Dowling, D. R. (2011). *Fluid Mechanics*. Fifth Edition. Academic Press. ISBN: 9780123821003.

Lipovsky, B. P. (2018). "Ice Shelf Rift Propagation and the Mechanics of Wave-Induced Fracture". In: *Journal of Geophysical Research: Oceans* 123. DOI: 10.1029/2017JC013664.

Massom, R. A., Scambos, T. A., Bennetts, L. G., Reid, P., Squire, V. A., and Stammerjohn, S. E. (2018). "Antarctic ice shelf disintegration triggered by sea ice loss and ocean swell". In: *Nature* 558.7710, pp. 383–389. DOI: 10.1038/s41586-018-0212-1.

Olinger, S., Wiens, D. A., Aster, R. C., Bromirski, P. D., Gerstoft, P., Nyblade, A. A., and Stephen, R. A. (2018). *Microseismicity along Major Ross Ice Shelf Rift Resulting from Tidal Stresses and Thermal Contraction of the Near-Surface Firn Layer*. Abstract S41B-09 presented at 2018 Fall Meeting, AGU, Washington D.C., 10-14 Dec.

O'Neel, S., Larsen, C. F., Rupert, N., and Hansen, R. (2010). "Iceberg calving as a primary source of regional-scale glacier-generated seismicity in the St. Elias Mountains, Alaska". In: *Journal of Geophysical Research: Earth Surface* 115.F4. DOI: 10.1029/2009JF001598.

Peters, L. E., Anandakrishnan, S., Holland, C. W., Horgan, H. J., Blankenship, D. D., and Voigt, D. E. (2008). "Seismic detection of a subglacial lake near the South Pole, Antarctica". In: *Geophysical Research Letters* 35.23. DOI: 10.1029/2008GL035704.

Podolskiy, E. A. and Walter, F. (2016). "Cryoseismology". In: *Reviews of Geophysics* 54.4, pp. 708–758. DOI: 10.1002/2016RG000526.

Rignot, E., Jacobs, S., Mouginot, J., and Scheuchl, B. (2013). "Ice-Shelf Melting Around Antarctica". In: *Science* 341.6143, pp. 266–270. DOI: 10.1126/science.1235798.

Rignot, E., Mouginot, J., and Scheuchl, B. (2011). "Ice Flow of the Antarctic Ice Sheet". In: *Science* 333.6048, pp. 1427–1430. DOI: 10.1126/science.1208336.

Scambos, T. A., Haran, T. M., Fahnestock, M. A., Painter, T. H., and Bohlander, J. (2007). "MODIS-based Mosaic of Antarctica (MOA) data sets: Continent-wide surface morphology and snow grain size". In: *Remote Sensing of Environment* 111.2, pp. 242–257. DOI: 10.1016/j.rse.2006.12.020.

Schmidt, H. and Jensen, F. B. (1985). "A full wave solution for propagation in multilayered viscoelastic media with application to Gaussian beam reflection at fluid-solid interfaces". In: *The Journal of the Acoustical Society of America* 77.3, pp. 813–825. DOI: 10.1121/1.392050.

Shearer, P. M. (2009). *Introduction to Seismology*. Second Edition. Cambridge University Press.

Wiens, D. A., Anandakrishnan, S., Winberry, J. P., and King, M. A. (2008). "Simultaneous teleseismic and geodetic observations of the stick-slip motion of an Antarctic ice stream". In: *Nature* 453.7196, pp. 770–774.

Withers, M., Aster, R., Young, C., Beiriger, J., Harris, M., Moore, S., and Trujillo, J. (1998). "A comparison of select trigger algorithms for automated global seismic phase and event detection". In: *Bulletin of the Seismological Society of America* 88.1, pp. 95–106.